Universidad Pública de Navarra
Departamento de Ingeniería Eléctrica y Electrónica

LUMINESCENCE-BASED OPTICAL FIBER OXYGEN SENSORS FABRICATED BY MEANS OF LAYER-BY-LAYER NANO-ASSEMBLY

PhD dissertation by
Nerea de Acha Morrás

Advisors
Dr. César Elosúa Aguado
Prof. Francisco J. Arregui San Martín

Pamplona, January 2018

A mis padres
y mis hermanos

"Work hard,
dream big"

"Non gogoa,
han zangoa"

"¿Qué es la vida? Una ilusión,
una sombra, una ficción,
y el mayor bien es pequeño:
que toda la vida es sueño,
y los sueños, sueños son."
-Pedro Calderón de la Barca,
La vida es sueño

ACKNOWLEDGMENTS

This PhD thesis has been possible thanks to the pre-doctoral fellowship (reference BES-2014-069692) funded by the Spanish Ministry of Economy and Competitiveness through the TEC2013-43679-R project. This work has also been supported by the Spanish State Research Agency (AEI) and the European Regional Development Fund (ERDF-FEDER) through the TEC2016-79367-C2-2-R project and by the Government of Navarra Research Grants through the project Excelsen.

The author would also like to express her gratitude to the Public University of Navarra, where the main body of this thesis has been carried out, as well as the University of Nottingham, where a research internship was conducted under the supervision of Prof. Sergiy Korposh.

CEMITEC must also be acknowledged for the utilization of their facilities and Nadetech Innovations for their technical support, as well.

AGRADECIMIENTOS

Ahora que “de repente” ha llegado ese momento que durante mucho tiempo parecía que no iba a llegar, me toca escribir el apartado más importante de esta tesis: unas pocas palabras para dar las gracias a todas las personas que me habéis acompañado durante este camino. No es mi intención olvidarme de nadie, pero en caso de que sea así, pido perdón antes de empezar.

En primer lugar, quiero dar las gracias a quienes más me han ayudado para que esta tesis saliera adelante, animándome siempre y no dejándome tirar la toalla en los momentos más difíciles: Patxi Arregui y César Elosúa. Miles de gracias por vuestro apoyo y dedicación, por ver siempre el vaso medio lleno y, sobre todo, por vuestra infinita paciencia conmigo. Pero, sobre todo, gracias por ser aún mejores como personas. También muchas gracias a todos mis compañeros de Sensores, por estar dispuestos a ayudarme siempre. Además de muy buenos compañeros, creo que puedo decir que me llevo varios buenos amigos. Debo mencionar especialmente a Diego López, con quien más tiempo he pasado en el laboratorio, en prácticas y en los congresos, a Abián por sus continuos ánimos y consejos y, sobre todo, a Aitor Urrutia y Pedro Rivero, por estar dispuestos a escucharme y ayudarme siempre. También quiero dar las gracias a los técnicos de laboratorio por hacer que nuestro trabajo sea siempre más fácil (mención especial para Santiago de Miguel, por lo mucho que me he reído con él). Además de a todos ellos, he tenido la suerte de conocer a muy buenas personas de otros grupos con los que he compartido muchos momentos: entre ellos, Javi, Juanjo, Paola y, sobre todo, Amagoia, quien, además de ser una buena amiga, ha sido siempre un ejemplo de trabajo y esfuerzo para mí.

I would also like to express my gratitude to the Optics and Photonics Research Group from the University of Nottingham, for making me feel at home from the very beginning of my stay in the group. I would like to acknowledge Sergiy Korposh for his supervision, and Jiri Hromadka and

Ricardo Correia for their major support in the lab. Also, thanks to everyone in the group (Baptiste, Chalani, David, Kalei, Qimei, Shiemma, Víctor, etc.), because with them I spent my best moments at uni. Ulises and Sia (sorry, Dr. Uli and Dr. Siavash Mirahmadi) deserve a special mention for their friendship: you owe me a visit, and you know it. También muchas gracias a los expatriados que conocí en Nottingham por acogerme tan bien desde el principio, especialmente a Ana F., Elena, Esther, Luismi, Oscar, Sergio y Teresa. Ojalá tengáis un futuro tan grande como el que os merecéis. Aquí, tengo que volver a acordarme de quienes me dieron la oportunidad de vivir esta increíble experiencia, Patxi y César: gracias por animarme siempre, y sin dudas, a realizar esta estancia. Igualmente, gracias a quienes me visitaron durante aquel periodo y, sobre todo, a quienes se atrevieron a montarse en coche conmigo como conductora.

Como siempre, también quiero dar las gracias a todos los amigos con los que he compartido juevintxos, viajes, montes, fiestas, veranos (y los que nos quedan), y que me han apoyado siempre: Amaia G. Amaia O., Ángel, Borja, Iratxe, Itziar, Nerea, Raquel y Sonia. Leire se merece un capítulo aparte por todos los buenos ratos que hemos pasado juntas.

Por último, y por ello también lo más importante, tengo que agradecer el apoyo constante de toda mi familia (tíos, primos y sobre todo, abuelos). De forma especial, quiero darles las gracias a mis hermanos, Javier y Loreto por su cariño, apoyo y paciencia durante estos años, y, por encima de todos, a mis padres, Pedro y Ana, por su ejemplo impagable, su esfuerzo incansable y su apoyo y cariño incondicional. Ojalá esto esté ala altura de lo que os merecéis. Como siempre, ni quiero, ni puedo, olvidarme de mi abuelo Pedro, que seguro que me habrá echado algún cable.

Muchas gracias a todos,

Nerea.

ABSTRACT

Over the last decades, luminescence quenching has been established as a widespread technique for gaseous oxygen monitoring in a broad range of applications. Thus, considerable effort has been made to manufacture luminescent oxygen sensors. The performances of such sensors are determined by the oxygen indicator and the matrix that entraps this indicator as well. In spite of its versatility for fine-tuning the final features of nanostructures, the Layer-by-Layer nano-assembly technique has been rarely studied for fabricating these sensors. This could be explained by the fact that most of the optically stable and highly sensitive oxygen indicators are not water soluble.

The main objective of this work is to combine these detection and deposition techniques with optical fiber setups, for the fabrication and characterization of luminescent optical fiber oxygen sensors fabricated by Layer-by-Layer nano-assembly.

Table of contents

Chapter 1

Introduction: motivation and objectives

1.1. Motivation and objectives

Photoluminescence is of great interest because it has become an essential tool for a wide range of research fields, such as genetic analysis [1], biochemistry [2], life science [3] or materials science [4], just to name a few. For instance, fluorescent probes have been utilized to detect novel risk factors of thrombosis [5], to characterize genetic alterations in ductal carcinoma [6], to identify heavy metal ions [7] or to monitor oxygen concentrations [8]. This latter application is one of the most extended owing to the key role that oxygen plays in many biochemical processes [9], either as a reactant [10] or as a product [11]. Thus, luminescent oxygen sensors are well established in applications found in environmental science, food packaging industry or biotechnology, among others [12].

This kind of sensors is based on the collisional quenching of the luminescent intensity of an indicator produced by molecular oxygen [13].

Therefore, in last decades, considerable effort has been devoted to the manufacture of optically stable and chemically robust luminescent indicators for sensing purposes [14]. These indicators are usually embedded in polymeric films, which also play a key role on the performance of the sensors: the sensitivity of these sensors does not only depend on the features of the indicator, but also on the distribution of this indicator inside the matrix [15], as well as on the own characteristics of this matrix [16]. Such characteristics can be tailored in the nanometer scale [18]. Although there are different techniques to produce luminescent sensing coatings such as chemical vapor deposition, liquid phase epitaxy, sputtering or atomic layer deposition all these are usually expensive and do not adapt well to mass production. There are other alternatives such as spin coating, spray coating or sol-gel dip coating which are more affordable but, unfortunately, are not able to control the characteristics of the material on the nanometer scale and optimize the devices. An appropriate approach could be the Layer-by-Layer (LbL) nano-assembly technique, which allows the fabrication and tuning of nanostructured films. LbL is a wet technique that basically consists of the deposition of oppositely charged materials (usually polyelectrolytes) by electrostatic and other forces acting simultaneously.

Another remarkable characteristic of these luminescence-based sensors is the increasing utilization of optical fiber for their fabrication. Among the advantages that this technology presents compared to the semiconductor-based one, its electromagnetic immunity [19], the possibility of multiplexing large amounts of sensors over long distances [20], the lack of oxygen consumption [21] or its biocompatibility [22] are some of the most attractive ones. Furthermore, the use of optical fiber as substrate of luminescence-based sensors requires the use of optical instrumentation that is compatible with the spectral features of the sensitive indicator: on one side, the central wavelength of the light source must overlap with the absorption spectrum of the indicator and, on the other side, the spectrometer must be highly sensitive in the range of wavelengths of the luminescent peak and exhibit a fast response towards intensity changes. Moreover, the choice of the dimensions of the optical

fibers employed is crucial, as they determine the light coupling from the light source towards the sensor and from the sensor to the spectrometer.

Taking into account all these factors, the main goal of this thesis is to combine the above-mentioned detection and fabrication techniques, together with the optical fiber as substrate, for the development and study of luminescent optical fiber sensors for oxygen and gases monitoring fabricated by means of the Layer-by-Layer nano-assembly technique. This objective presents different challenges that have to be overcome in order to carry out the proposed study:

- The first one is related to oxygen indicators: the most sensitive and chemically stable luminophores employed for oxygen sensing are water-insoluble metallo-porphyrins. This characteristic makes them theoretically incompatible with the standard LbL nano-assembly technique: consequently, their deposition by means of this technique is one of the main challenges of this thesis.

- Once this goal is achieved, the optical set-up must be carefully selected in order to excite properly the luminescent indicator, as well as ensuring the appropriate coupling of the luminescent emission from the sensor to the spectrometer.

- When that objective is met, the following step would consist of the detailed analysis of the features of different polymeric matrices that determine the performance of these oxygen sensors, in terms of sensitivity and kinetics. This would allow the selection of the optimum polymeric matrix to entrap the luminescent indicator.

- Finally, for each polymeric matrix, the effect of increasing the spacing distance between the luminescent layers should be studied. Besides, in the case that the optimal separation between the luminophore films is found, it should be figured out which parameter determines that separation.

1.2. Organization

This thesis is organized as follows. First of all, a review of the state of the art of luminescence-based sensors fabricated by means of the LbL technique is presented in Chapter 2. This chapter goes over the main purposes of luminescent sensors: oxygen monitoring, metal ions detection and biosensing applications. Sensors based on indicators immobilized in multilayer films are analyzed and solution-based probes as well.

Chapter 3 is devoted to the LbL assembly of a water-insoluble metalloporphyrin which is sensitive to oxygen. With that aim, the oxygen indicator has been tried to be entrapped into a Zirconium Phosphate film and into a polymeric coating, as well. In order to analyze the proper incorporation of the sensing material inside the embedding matrix, the absorption spectrum as well as the Energy Dispersive X-ray spectroscopy of this matrix have been studied.

In Chapter 4, the effect of three different cationic polyelectrolytes (PDDA, PEI and PAH) on the performance of luminescent sensors is investigated. The hydrophilicity/hydrophobicity and the morphological properties of the sensing films have been studied, trying to find any kind of relationship between these parameters and the sensitivity and kinetics of the sensors. The influence of these cationic polyelectrolytes on the distribution of the luminophore inside the entrapping matrices has also been examined, and some attempts to optimize the deposition conditions (pH value of the polycationic solution) of a sensing nanostructure have been carried out.

Chapter 5 is focused on the optimization of the spacing distance between luminescent layers in order to avoid self-quenching. Using the same cationic polyelectrolytes as in the previous chapters, different separation distances between the luminophore films have been analyzed. This study has permitted to investigate the effect of that distance on the sensitivity of the sensors and on the distribution of the indicator inside the sensing nanostructures, as well.

Finally, the main conclusions obtained in this thesis are explained in Chapter 6. Additionally, three appendices are included in this dissertation: the first one is focused on the development of a luminescent and colorimetric optical fiber sensor for the detection of organic vapors. In Appendix II, Long Period Gratings (LPGs) coated with a metal-organic framework are studied as ethanol sensors: one of the devices has also been utilized to detect ethanol in human breath. To conclude, in Appendix III, the scientific publications produced during the development of this research are listed.

Bibliography

1. Bucci, M.; Wente, S. R. A novel fluorescence-based genetic strategy identifies mutants of Saccharomyces cerevisiae defective for nuclear pore complex assembly. *Molecular Biology of the Cell* **1998**, *9*, 2439–2461, doi:10.1091/mbc.9.9.2439.
2. Slaughter, B. D.; Li, R. Toward quantitative "in vivo biochemistry" with fluorescence fluctuation spectroscopy. *Molecular Biology of the Cell* **2010**, *21*, 4306–4311, doi:10.1091/mbc.E10-05-0451.
3. Boghossian, A. A.; Zhang, J.; Barone, P. W.; Reuel, N. F.; Kim, J.-H.; Heller, D. A.; Ahn, J.-H.; Hilmer, A. J.; Rwei, A.; Arkalgud, J. R.; Zhang, C. T.; Strano, M. S. Near-infrared fluorescent sensors based on single-walled carbon nanotubes for life sciences applications. *ChemSusChem* **2011**, *4*, 848–863, doi:10.1002/cssc.201100070.
4. Wang, H.; Xie, L.; Peng, Q.; Meng, L.; Wang, Y.; Yi, Y.; Wang, P. Novel thermally activated delayed fluorescence materials-thioxanthone derivatives and their applications for highly efficient OLEDs. *Advanced Materials* **2014**, *26*, 5198–5204, doi:10.1002/adma.201401393.
5. Tirado, I.; Fontcuberta, J.; Soria, J. M. Rapid Detection of the 46C → T Polymorphism in the Factor XII Gene, a Novel Genetic Risk Factor for Thrombosis, by Melting Peak Analysis Using Fluorescence Hybridization Probes. *Genetic Testing* **2003**, *7*, 295–301, doi:10.1089/109065703322783644.
6. Murphy, D. S.; Hoare, S. F.; Going, J. J.; Mallon, E. E. A.; George, W. D.; Kaye, S. B.; Brown, R.; Black, D. M.; Keith, W. N. Characterization of extensive genetic alterations in ductal carcinoma in situ by fluorescence in situ hybridization and molecular analysis. *Journal of the National Cancer Institute* **1995**, *87*, 1694–1704, doi:10.1093/jnci/87.22.1694.
7. Oehme, I.; Wolfbeis, O. S. Optical Sensors for Determination of Heavy Metal Ions. *Mikrochimica Acta* **1997**, *126*.
8. McShane, M. J.; Brown, J. Q.; Guice, K. B.; Lvov, Y. M. Polyelectrolyte Microshells as Carriers for Fluorescent Sensors: Loading and Sensing Properties of a Ruthenium-Based Oxygen Indicator. *Journal of Nanoscience and Nanotechnology* **2002**, *2*, doi:10.1166/jnn.2002.118.
9. Raymond, J.; Segrè, D. The effect of oxygen on biochemical networks and the evolution of complex life. *Science (New York, N.Y.)* **2006**, *311*, 1764–7, doi:10.1126/science.1118439.
10. Reiter, R. J.; Tan, D. X.; Manchester, L. C.; Qi, W. Biochemical reactivity of melatonin with reactive oxygen and nitrogen species: A review of the evidence. **2001**, *34*, 237–256, doi:10.1385/CBB:34:2:237.
11. Tyystjärvi, E.; Karunen, J.; Lemmetyinen, H. Measurement of photosynthetic oxygen evolution with a new type of oxygen sensor. *Photosynthesis Research* **1998**, *56*, 223–227, doi:10.1023/A:1005994311121.
12. Wang, X. D.; Wolfbeis, O. S. Optical methods for sensing and imaging oxygen: Materials, spectroscopies and applications 2014, *43*, 3666–3761.
13. Demas, J. N.; DeGraff, B. A.; Coleman, P. B. Oxygen sensors based on luminescence quenching 1999, *71*.

14. Quaranta, M.; Borisov, S. M.; Klimant, I. Indicators for optical oxygen sensors 2012, *4*, 115–157.
15. Ogurtsov, V. I.; Papkovsky, D. B. Modeling of luminescence-based oxygen sensors with non-uniform distribution of excitation and quenching characteristics inside active medium. *Sensors and Actuators B: Chemical* **2003**, *88*, 89–100, doi:https://doi.org/10.1016/S0925-4005(02)00312-X.
16. Yang, Y.-H.; Haile, M.; Park, Y. T.; Malek, F. A.; Grunlan, J. C. Super Gas Barrier of All-Polymer Multilayer Thin Films. *Macromolecules* **2011**, *44*, 1450–1459, doi:10.1021/ma1026127.
17. Elzbieciak, M.; Zapotoczny, S.; Nowak, P.; Krastev, R.; Nowakowska, M.; Warszyński, P. Influence of pH on the structure of multilayer films composed of strong and weak polyelectrolytes. *Langmuir* **2009**, *25*, 3255–3259, doi:10.1021/la803988k.
18. Lakowicz, J. R. Principles of fluorescence spectroscopy. *Principles of Fluorescence Spectroscopy*.
19. Sabri, N.; Aljunid, S. A.; Salim, M. S.; Fouad, S. *Fiber optic sensors: Short review and applications*; 2015; Vol. 204;.
20. Hernandez-Lorenzo, R.; Lopez-Amo, M.; Urquhart, P. Single and double distributed optical amplifier fiber bus networks with wavelength division multiplexing for photonic sensors. *Journal of Lightwave Technology* **1998**, *16*, 485–489, doi:10.1109/50.664053.
21. Wang, X.; Chen, H.; Zhao, Y.; Chen, X.; Wang, X.; Chen, X. Optical oxygen sensors move towards colorimetric determination. *TrAC Trends in Analytical Chemistry* **2010**, *29*, 319–338, doi:10.1016/j.trac.2010.01.004.
22. Socorro, A. B.; Corres, J. M.; Del Villar, I.; Arregui, F. J.; Matias, I. R. Fiber-optic biosensor based on lossy mode resonances. *Sensors and Actuators, B: Chemical* **2012**, *174*, 263–269, doi:10.1016/j.snb.2012.07.039.

Chapter 2

Luminescent optical sensors fabricated by means of the Layer-by-layer nano-assembly technique: state of the art

This chapter reviews the state of the art of photoluminescence-based sensors fabricated by means of the Layer-by-layer nano-assembly technique, including solution-based probes as well as multilayer sensing films. Through the analysis of the main luminescent sensing applications (metal ions detection, dissolved and gaseous oxygen monitoring and biosensing), a wide range of luminescent materials, and the most utilized approaches for their entrapment or assembly into LbL-coatings are revised.[1]

[1] This chapter has been partially published in the review entitled *Luminescence-based optical sensors fabricated by means of the Layer-by-layer nano-assembly technique* in Sensors.

2.1. Introduction

Optical sensing techniques allow the possibility of making remote [1] and non-invasive measurements [2], as well as working in hazardous environments [3]. These, and many other significant advantages over other detection technologies, have attracted the attention of scientists over the last decades [4-5].

Optical sensors can be based on different transduction mechanisms, such as absorption [6-7], resonances [8-10] or photoluminescence [11-13]. The latter consists of the emission of light by a material as a consequence of its previous absorption at lower wavelengths. Depending on the lifetime of this emission (i.e., the average time that takes the intensity to drop by 1/*e*), luminescence can be classified as fluorescence (lifetime is in the range of ps and ns) or as phosphorescence (lifetime longer than ms). Besides, the intensity of this emission, as well as its lifetime, can be quenched or enhanced by the variation of different external parameters: pH [14], temperature [15], biomolecules [16], oxygen [17] or metal ions concentration [18]. This modulation of the intensity (and lifetime) by external parameters has been widely employed for the development of luminescence-based sensors, either in solution [19-20], or onto different substrates [21-23].

Among the existing kinds of luminescent materials (also known as luminophores), quantum dots (QDs) [24-25], nanoparticles (NPs) [26-27], fluoropolymers [28], dyes [29-30] and porphyrins [31-33] have been the most utilized. For the fabrication of sensors, these luminescent materials are usually entrapped or encapsulated in different matrices [34-35] or shells [36-37] which must be designed to facilitate the interaction between the analyte and the sensing material [38].

There are three key requirements that luminescent sensors must meet: good photostability and high selectivity and sensitivity [39]. To achieve these latter characteristics and allow the rapid adsorption/desorption of the target analytes to the sensing films, highly permeable coatings are usually fabricated by means of the dip-coating [40], spin-coating [41], sol-gel [42] or xero-gel [43] techniques. However, when utilizing these

methods, the distribution of the luminophore inside the films cannot be controlled, what gives rise to their aggregation and causes the self-quenching, hence reducing significantly the sensors' sensitivity [44]. This fact can be overcome by employing the layer-by-layer nano-assembly technique for the fabrication of the sensors. This method consists of the deposition of oppositely charged materials (typically polyelectrolytes) by electrostatic forces or other attractive forces acting cooperatively, including interactions such as hydrophobic attraction [45]. LbL has been experimentally demonstrated as a powerful method for the fabrication of luminescence-based sensors, since it is a reproducible technique that allows the utilization of a wide variety of indicators. An accurate selection of the materials and the assembly parameters permits to modify the permeability of the nanostructure [46], promoting the diffusion of the target species or forming a barrier against the undesired ones [47] Furthermore, it also allows to control the layer thickness in the nanometer scale and tailor the space distance between different layers, with the aim of avoiding any kind of undesired interactions [48].

In the last years, luminescence has become a powerful detection mechanism in a broad range of areas, being the most important sensing mechanism in different biological applications [49]. This fact, together with the versatility that the LbL technique offers for the fabrication of custom-made sensors [50], has led to the development of a wide variety of luminescent probes built up by this technique.

Thus, in this chapter a review of the state of the art has been made, analyzing solution-based probes and multilayer sensing films fabricated for different purposes: metal ions detection, dissolved and gaseous oxygen monitoring, and biosensing applications. Furthermore, some new challenges for the fabrication of luminescent sensors by means of the LbL technique are addressed at the end of this chapter.

2.2. Luminescent sensors based on encapsulated indicators

The progress of the *in vivo* measurement systems in the last years has yielded to the development of biocompatible optical sensors [51]. A widespread method for the fabrication of this kind of sensors consists of the encapsulation of the sensitive material in multilayered nanostructures (also called shells or capsules). These walls have to meet a key requirement: protecting the sensitive molecules from external environment while allowing fast diffusion of the target analyte [52]. LbL encapsulation of sensors was first described in the early 2000s [53-54] and, since then, many different applications have been reported [55-58].

Particles encapsulation requires from a template that is coated with a multilayered nanostructure and then dissolved. The main methods for immobilizing the luminophores inside the shells are diffusion and precipitation [57], which are illustrated in Figure 2.1.

In the case of encapsulating the sensing molecules by diffusion, the multilayered coatings are adsorbed onto sacrificial templates, usually dissolvable or degradable inorganic polymeric microspheres. Once the capsules are fabricated, the templates are dissolved in order to leave hollow microspheres, which are suspended in solutions of the sensing molecules, that are loaded inside them just by diffusion [58]. Despite this technique offers the possibility of employing almost any dissolvable template, it also exhibits the lowest loading efficiency.

When the luminophores are encapsulated by precipitation, they co-precipitate with the sacrificial templates before the shell is built and, subsequently, templates are diluted [59]. By employing this technique, the highest loading efficiency rates can be obtained.

When choosing the templates, it is important to take into account two factors: firstly, they must be able to keep their structural properties during the coating process and, secondly, they have to be easily dissolved once the encapsulating nanostructure has been attached to their surface [59]. Typical materials used as templates are calcium carbonate ($CaCO_3$)

[60], silica [61], latex [62] polystyrene [63], or gold [64] nanoparticles and melamine formaldehyde [65] microspheres. The dimensions of the shell depend on their shape and size, which can range from nanometers to microns [66].

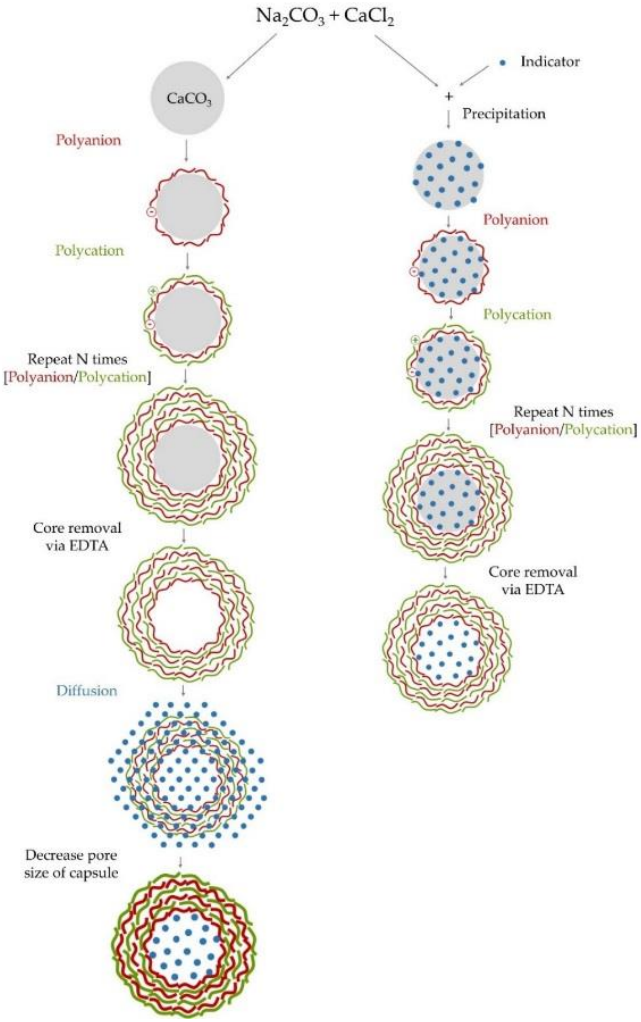

Figure 2.1. Schematic of the encapsulation techniques.

Owing to the versatility of the LbL method, it has been extensively used for micro- and nanoparticles encapsulation [67][68], usually made of polyelectrolytes. That is because, by varying some properties of polyelectrolyte solutions and controlling the deposition conditions, it is possible to tailor the properties of the capsule walls [69]. For instance, the pH of the solutions not only influences the shell thickness [70], but also its permeability [71] and, hence, the diffusion rate of molecules inward.

As mentioned above, capsules are usually made of different polyelectrolyte combinations. The most used pairs are poly(allylamine hydrochloride) (PAH)/poly(styrene sulfonate) (PSS) [72], and poly(diallyldimethylammonium chloride) (PDDA)/poly(styrene sulfonate) (PSS) [73]. Apart from them, other combinations of materials can be employed, for instance, poly-l-lysine/poly(l-glutamatic acid) [74], chitosan/dextran [61] or poly-l-lysine/heparin [75]. However, their use is not as common as the first mentioned polyelectrolyte pairs.

One of the advantages of this technique is the possibility of developing self-referenced sensors by using a sensitive luminophore and a non-sensitive luminophore that acts as an optical reference [61]. Ideally, both of them have the same absorption spectrum and a complementary emission spectrum [51]. In this manner, it is possible to use a single excitation light source and the simultaneous monitoring of the emission peaks: one of them will change in presence of the target analyte, while the other one will remain constant. Apart from encapsulating both luminophores [59], it is also common that one of them is assembled as part of the multilayered coating [76].

The main applications of these sensors (metal ion detection, dissolved oxygen sensing and glucose and lactate monitoring) are analysed in the following subsections.

2.2.1. Encapsulated sensors for ions detection

Metal ions are known to be highly toxic materials [77], so considerable efforts have been made for their detection in aqueous media. Duchesne

and co-workers [78] fabricated a potassium sensor by encapsulating the fluorescent indicators by the diffusion technique: using positively charged melamine formaldehyde (MF) particles as templates, multilayer capsules of PSS and PDDA were fabricated. The MF cores were diluted afterwards in HCl and then, the capsules were immersed in solutions of potassium-binding benzofuran isophthalate tetraammonium salt (PBFI), which diffused through the walls to the hollow cores. The PBFI-loaded sensors exhibited a luminescent peak at 500 nm, which moved towards lower wavelengths and increased in intensity upon the addition of K^+ ions in the 0 – 45 mM range.

Rare-earth (RE) nanocrystals are of great interest for sensing applications because of their optical and chemical properties, such as long lifetime (in the range of μs or ms) [79], high quantum yield or resistance to photobleaching [80]. A fluorescent sensing system based on RE nanocrystals and CdSe/ZnS quantum dots was fabricated by using the LbL technique in [81]: PEI-coated $NaYF_4$:Ce,Tb nanorods were spaced from the CdSe/ZnS QDs by a PSS/PAH bilayer. Under UV illumination (255 nm), a dual emission was observed, with the luminescent peaks centered at 542 nm (RE nanocrystals) and 650 nm (QDs), being the last one the dominant due to the fluorescence resonance energy transfer between the RE nanorods and the QDs. Under exposition to different concentrations of Cu^{2+} or Ag^+ metal ions in the μM range, the luminescent intensity at 650 nm decreased, while that corresponding to the peak centered at 542 nm remained constant. This fact can be observed in Figure 2.2, in which the system was exposed to different metal ions (30 μM): the red color (650 nm) was quenched by Ag^+ ions, while it completely disappeared in the presence of Cu^{2+} ions, demonstrating a high selectivity.

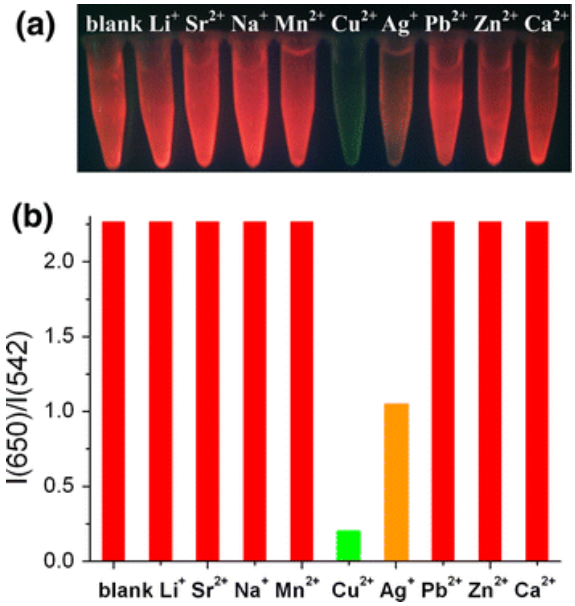

Figure 2.2. Effect of the different metal ions on the RE-QD composites. Reprinted from [81] with permission from Springer.

Other encapsulated sensors for the detection of metal ions are summarized in Table 2.1. Most of them use salts as sensitive indicators (e.g., potassium-binding benzofuran isophthalate tetraammonium salt (PBFI) or sodium-binding benzofuran isophthalate tetraammonium salt (SBFI)), and FluoSpheres as references.

2.2.2. Encapsulated sensors for dissolved oxygen detection

The most extended purpose of this kind of sensors is the detection of low concentrations of dissolved oxygen for biomedical applications, typically utilizing ruthenium porphyrins as indicators. McShane et al. [51] fabricated a self-referred oxygen sensor by employing tris(2,2'-bipyridyl) dichlororuthenium(II) hexahydrate (Ru(bpy)) as sensitive material and fluorescein isothiocyanate (FITC) as the reference one, so the

use of a single light source at 460 nm was possible, and the simultaneous monitoring of the luminescent peaks at 525 nm (FITC) and 620 nm (Ru(bpy)), allowing ratiometric measurement of the fluorescence.

Analyte	Sensitive indicator	Ref indicator	Capsule	Detection range	LOD	Ref
K^+	PBFI	-	$(PSS/PAH)_5$	0 – 45 mM		[62]
K^+	PBFI	Fluo Spheres	$(PAH/PSS)_4$ PAH	0 – 282 mM		[82]
K^+	PBFI	-	2, 3, and 5 bilayers of {PSS/PDDA}	0 – 45 mM	-	[78]
K^+	PBFI	Europium Fluo Spheres	$(PAH/PSS)_4$ PAH	0 – 120 mM	1 mM	[83]
K^+	PBFI	Europium Fluo Spheres	$(PAH/PSS)_4$ PAH	0 – 300 mM	1.2m M	[84]
Na^+	SBFI	-	2, 3, and 5 bilayers of {PSS/PDDA}	0 – 100 mM	-	[53]
Cu^{2+}, Ag^+	CdSe/Zn Se QDs	NaYF4:Ce,Tb RE nanocrystals	PSS/PAH	0-35 μM Cu^{2+} 0-90 μM Ag^+	-	[81]
Pb^{2+}	CdSe/Cd Se QDs	-	chitosan/ xylenol orange	0.05 – 6 μM	20 nM	[56]

Table 2.1. Encapsulated sensors for ions detection.

For the capsules fabrication, 2.6 μm melamine formaldehyde microtemplates were coated with $\{PSS/PAH\text{-}FITC\}_n$ or $\{PSS/PAH\text{-}FITC\}_nPSS$ shells. After the cores dilution, the capsules were suspended in solutions of the oxygen sensitive indicator at different pH values, and Ru(bpy) molecules were loaded by diffusion. The highest loading

efficiency was achieved in the case of the {PSS/PAH-FITC}$_5$PSS shells, when the pH value of the Ru(bpy) solution was 10.4. Suspensions of these sensors were bubbled with O_2 and N_2, and it was observed that in presence of O_2, intensity at 620 nm (Ru(bpy)) decreased while intensity at 525 nm (FITC) remained constant. A total decrease of 15% of the I_{620}/I_{525} ratio was measured when only O_2 was bubbled. Moreover, the sensor response was consistent with the dynamic changes of the gas levels along the time.

2.2.3. Encapsulated sensors for gaseous oxygen detection

The most extended purpose of this kind of sensors is the detection of low concentrations of dissolved oxygen for biomedical applications, typically utilizing ruthenium porphyrins as indicators. McShane et al. [51] fabricated a self-referred oxygen sensor by employing tris(2,2'-bipyridyl) dichlororuthenium(II) hexahydrate (Ru(bpy)) as sensitive material and fluorescein isothiocyanate (FITC) as the reference one, so the use of a single light source at 460 nm was possible, and the simultaneous monitoring of the luminescent peaks at 525 nm (FITC) and 620 nm (Ru(bpy)), allowing ratiometric measurement of the fluorescence (I_{620}/I_{525}). For the capsules fabrication, 2.6 μm melamine formaldehyde microtemplates were coated with {PSS/PAH-FITC}$_n$ or {PSS/PAH-FITC}$_n$PSS shells. After the cores dilution, the capsules were suspended in solutions of the oxygen sensitive indicator at different pH values, and Ru(bpy) molecules were loaded by diffusion. The highest loading efficiency was achieved in the case of the {PSS/PAH-FITC}$_5$PSS shells, when the pH value of the Ru(bpy) solution was 10.4. Suspensions of these sensors were bubbled with O_2 and N_2, and it was observed that in presence of O_2, intensity at 620 nm (Ru(bpy)) decreased while intensity at 525 nm (FITC) remained constant. A total decrease of 15% of the I_{620}/I_{525} ratio was measured when only O_2 was bubbled. Moreover, the sensor response was consistent with the dynamic changes of the gas levels along the time.

A palladium porphyrin was encapsulated in [59] by the co-precipitation technique: the carboxylate modified FluoSpheres (FS), used as reference, and the Pd-meso-tetra(4-carboxyphenyl) porphine (PdTCPP) co-precipitated with the calcium carbonate ($CaCO_3$) nanoparticles. They were first stabilized in poly(vinylsulfonic acid) (PVSA) and then, coated with the multilayer $(PDDA/PSS)_{10}$ structure, and the $CaCO_3$ cores were diluted. When the capsules were excited at 405 nm, they emitted luminescence at 515 nm (FS) and 700 nm (PdTCPP). Under exposition to different dissolved oxygen concentrations, the intensity of the emission peak centered at 515 nm remained constant, while that of the peak at 700 nm decreased proportionally to the oxygen concentration. Thus, the ratio I_{700}/I_{515} was used to characterize the sensor, which had a detection limit of 7.62 μM. A schematic illustration of this sensor and its response towards oxygen in displayed in Figure 2.3.

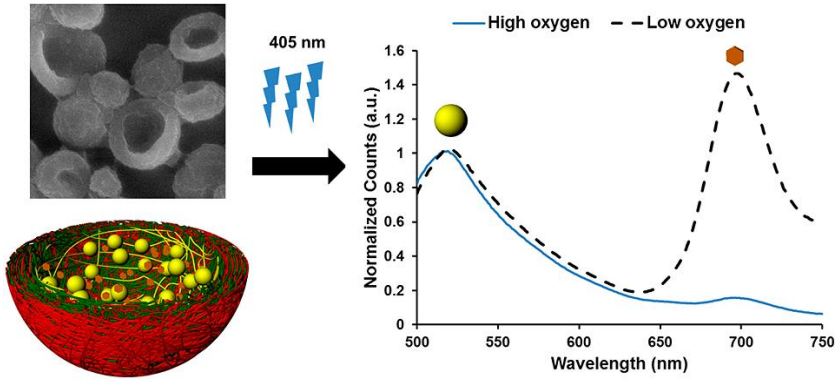

Figure 2.3. SEM image of the nano-capsules after the dilution of the core (up left), schematic representation of the encapsulated sensors (down left) and luminescence spectra of the sensors when exposed to high and low dissolved oxygen concentrations (right). Reprinted with permission from [59]. Copyright 2014 American Chemical Society.

Other dissolved oxygen probes were developed with different ruthenium porphyrins, such as tris(4,7-diphenyl-1,10-phenanthroline)ruthenium(II) dichloride (Ru(dpp)) or $[Ru(Ph_2phen)_3]^{2+}$. They are summarized in Table 2.2.

Sensitive indicator	Reference indicator	Capsule	Detection range	Ref
Ru(dpp)	green polystyrene FluoSpheres	$(PAH/PSS)_3$	0 – 1500 mM	[83]
Ru(dpp)	carboxylate-modified nanospheres	$(PAH/PSS)_3$	ON/OFF probe	[72]
Ru(dpp)	-	$(PSS/PAH)_4/PSS$	0 – 0.6 mM	[85]
Ru(bpy)	FITC	$(PSS/PAH\text{-}FITC)_5/PSS$		[51]
Ru(bpy)	FITC	$(PSS/PDDA)_5$/ PSS	ON/OFF probe	[73]
$[Ru(Ph2phen)_3]^{2+}$	carboxylate-modified FluoSpheres	$(PAH/PSS)_3$	0 – 1.5 mM	[86]
PdTCPP	carboxylate-modified FluoSpheres	$(PDDA/PSS)_{10}$	0 – 250 μM	[59]

Table 2.2. Encapsulated sensors for dissolved oxygen detection.

2.2.4. Encapsulated sensors for glucose and lactate monitoring

A particular application of dissolved oxygen sensors is glucose monitoring [87]. To this end, glucose binding proteins, usually glucose-oxidase [85] or apo-glucose-oxidase [88] are loaded inside the multilayered shells, as well as the sensitive molecules. For instance, Kazakova et al. [85] fabricated 5 μm-microcapsules made of PAH and PSS

loaded with the oxygen-sensitive dye (Ru(dpp)) that entrapped glucose-oxidase. This indicator emitted fluorescence between 560 and 700 nm, and its intensity was inversely proportional to oxygen concentration. Furthermore, glucose concentration was correlated with oxygen reduction during enzymatic degradation by glucose oxidase. The increasing of the fluorescent intensity and the calibration curve of this sensor upon addition of different glucose concentrations are observed in Figure 2.4.

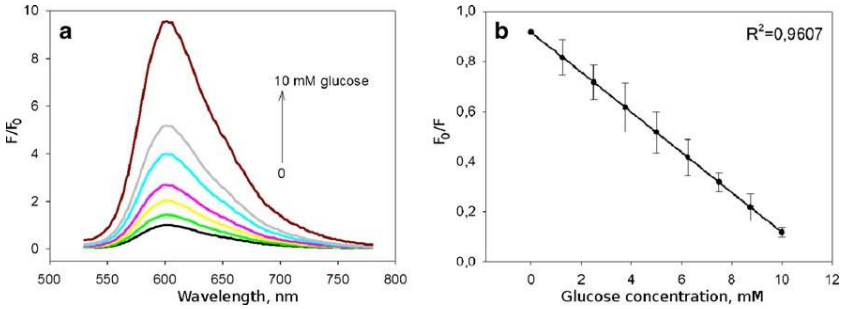

Figure 2.4. (a) Relative fluorescence intensity upon the addition of different glucose concentration. F and F_0 represent the fluorescence intensities in the presence (F) and absence (F_0) of glucose. (b) Calibration curve of the sensor. Reprinted from [85] with the permission from Springer.

The same authors also coated lactate oxidase and peroxide with capsules of PAH and PSS loaded with peroxide sensitive dihydrorhodamine 123 (DHR123), which was sensitive to hydrogen peroxide. Addition of lactate in presence of lactate oxidase produced hydrogen peroxide, which oxidized DHR123 in the presence of peroxide, yielding to rhodamine123, a molecule that emitted green fluorescence (510-560 nm), as it can be observed in Figure 2.5.

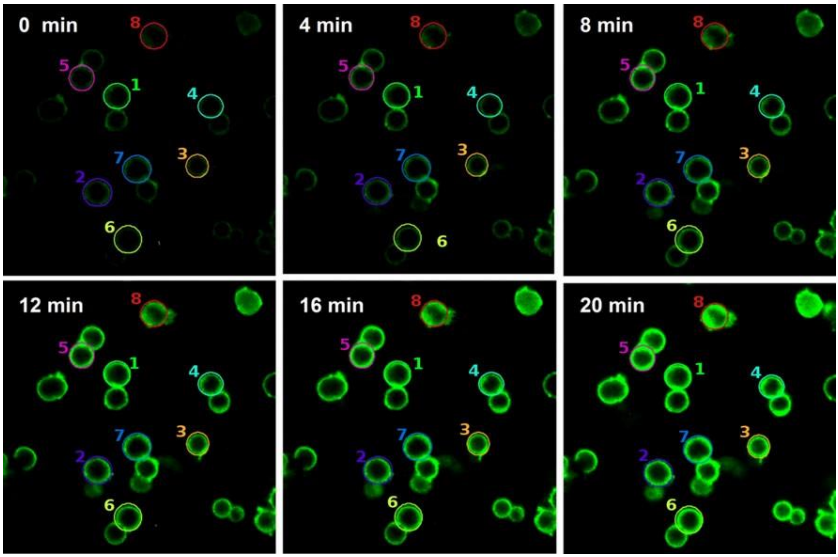

Figure 2.5. Confocal microscopy images of DHR123-labeled capsules containing lactate oxidase in the presence of 0.23 nM peroxidase and 4 mM lactate. Reprinted from [85] with the permission from Springer.

2.3. Luminophores immobilized in multilayer films for sensing applications

Luminescence-based sensors are also fabricated onto different substrates, by coating them with films in which the sensitive luminophores are embedded. These luminescent coatings exhibit many different advantages over solution-based sensors, such as the possibility of fabricating them onto almost every kind of substrates [89][90], or their easy storage and portability [91]. Other valuable features are their regeneration and reusability [92], as well as the good chemical stability of luminophores in solid state [93]. Furthermore, they can be used for vapor/gas detection [94], an application field where the encapsulated probes are hardly used [95].

The luminescent indicators can be entrapped in those multilayer structures by different methods, which are displayed in Figure 2.6. If they are immobilized during the fabrication process, this can be done by direct assembly (in the case they are not neutral materials), or by mixing, covalently linking or entrapping them inside charged materials. When the immobilization of the indicator occurs after the fabrication of the film, it is carried out by immersing the film in a solution of the dye. Examples of the above mentioned cases are explained in the following subsections.

2.3.1. LbL luminescent coatings for the detection of metal ions

A wide variety of indicators have been employed for the fabrication of luminescent films for the detection of metal ions, ranging from ligand-capped quantum dots to fluorescent conjugated polymers, including porphyrins and water-soluble dyes. To this latter category belongs 1-hydroxypyrene-3,6,8-trisulfonate, HPTS, a luminescent indicator widely used for pH monitoring [96-97]. For its deposition by the LbL technique, Lee and coworkers [98] attached it covalently to the polyanion PAA and, by using PAH as cationic polyelectrolyte, they fabricated the multilayer structure $[PAH/PAA\text{-}HPTS]_n$ onto glass slides. HPTS emitted luminescence at 485 nm when it was illuminated at 410 nm. The

maximum of the luminescent peak decreased linearly, but with different quenching constants, in the presence of electron-deficient metal cations, such as Fe^{3+} and Hg^{2+}, the nitro compound 2,4-dinitrotoluene, DNT, or the dicationic electron acceptor methyl viologen, MV^{2+} [99], as can be observed in Figure 2.7. Furthermore, this luminescence was not affected by other metal ions, for instance, Ba^{2+}, Ca^{2+}, K^{+}, Zn^{2+}, Cd^{2+}, and Pb^{2+}.

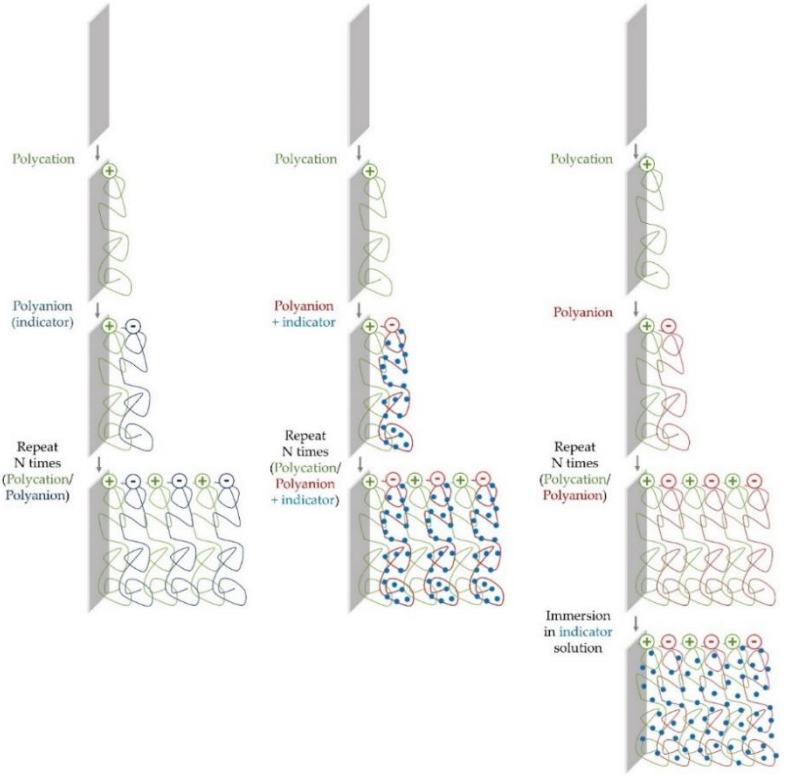

Figure 2.6. Schematic fabrication luminescent films: the non-neutral indicator is directly assembled into the film (left pathway), the neutral indicator is mixed, covalently linked or entrapped into a charged material and then it is assembled into the coating (central pathway), or the fabricated film is immersed into a solution of the dye (right pathway).

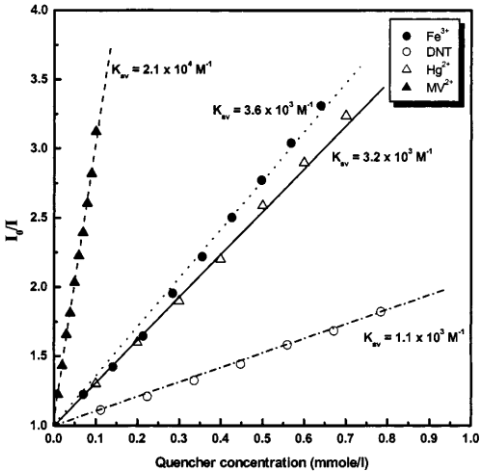

Figure 2.7. Stern–Volmer plots of multilayer films of PAH/PAA–HPTS as a function of different quencher concentrations. Reprinted with permission from [99]. Copyright © 2000, American Chemical Society.

Different fluorescent probes for mercury(II) ions detection based on the water soluble porphyrin 5,10,15,20-tetrakis(4-sulfonatophenyl)porphyrin (TPPS) were compared in [100]. PDDA was employed as cationic polyelectrolyte and TPPS, PSS or solutions with different ratios of TPPS:PSS were used as anionic counterparts. On one hand, it was observed that, when TPPS and PSS were co-deposited, giving rise to the structure $(PDDA/TPPS:PSS)_n$, higher quantum yields were observed when the PSS:TPPS ratio increased from 1:1 to 1:100. On the other hand, when depositing TPPS alternately (i.e. $(PDDA/PSS/PDDA/TPPS)_n$) the amount of adsorbed porphyrin was higher than when it was mixed with PSS, and also a good quantum yield was also achieved. A detailed analysis of this structure demonstrated that films with one or two tetralayers exhibited the best properties to be used as Hg(II) sensors, since they combined good optical properties with the lowest response time. In the case of (PDDA/PSS/PDDA/TPPS), the sensor was exposed to Hg(II) concentrations in the range between $3.3 \cdot 10^{-8}$ and $3.3 \cdot 10^{-5}$ M. For the higher concentrations, a longer time was required to

reach the equilibrium as a consequence of the adsorption process of the analyte within the films.

Fluoropolymers have also attracted interest for the development of optical sensors because of their high luminescence quantum yields. For instance, poly(9,9-bis(3'-phosphatepropyl)fluorenealt-1,4-phenylene) sodium salt (PFPNa), was synthesized and deposited with PDDA, by employing the LbL [101]. PFPNa polymer had absorption and luminescence peaks at 364 and 410 nm respectively, whose intensities were proportional to the pH of the aqueous solutions. The latter one was also inversely proportional to Fe^{3+} concentration. Furthermore, the sensor sensitivity was demonstrated to be almost independent on the number of bilayers (Figure 2.8a), so the 1-bilayer coating was employed as the sensing structure. In this case, fluorescence was quenched 400-fold for 10 μM of Fe3+ concentration (Figure 2.8b), and the detection limit for this metal ion was 10^{-7} M. Another thin-film sensor that employs a fluoropolymer for metal ion detection is reported in [102].

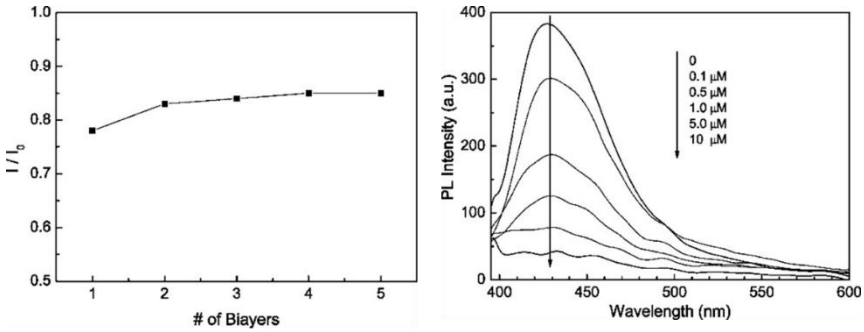

Figure 2.8. (a) Fluorescence response of $(PDDA/PFPNa)_n$ structures upon addition of 0.1 μM Fe^{3+}. (b) Quenching of the fluorescent peak when the sensor $(PDDA/PFPNa)_1$ is exposed to different Fe^{3+} concentrations. Reprinted with permission from [101]. Copyright 2008 American Chemical Society.

Negatively charged mercaptosuccinic acid (MSA) capped CdTe QDs have been assembled with the cationic polyelectrolyte PDDA onto quartz slides by means of the LbL technique. These QDs exhibited a luminescent peak centered at 589 nm, whose intensity decreased proportionally with the increment of Hg(II) for concentrations ranging from 0.01 μM to 1 μM [103]. Hg(II) removal from the sensing film was possible by adding glutathione (GSH) to the sample solutions, which also led to the recovery of the initial luminescent intensity. In subsequent research, this multilayer structure was employed to monitor Hg^{2+} and Cu^{2+} synchronously [104]: despite both ions quenched the luminescent intensity, the quenching constant of Hg^{2+} was higher than that of Cu^{2+}. Finally, by cross-linking the outermost layer of PDDA/CdTe QDs multilayers by bovine serum albumin (BSA) [105], a bi-color film was developed: it exhibited two luminescent peaks centered at 553 nm (green) and 657 nm (red), being green the dominant color. In the presence of Hg(II), the intensity of the first peak decreased (as shown in Figure 2.9a) and, for Hg(II) concentrations higher than 10^{-6} M, it was totally quenched, what made the sensing film to change its color from green to red. This color change was detectable by the naked-eye, as can be seen in Figure 2.9b.

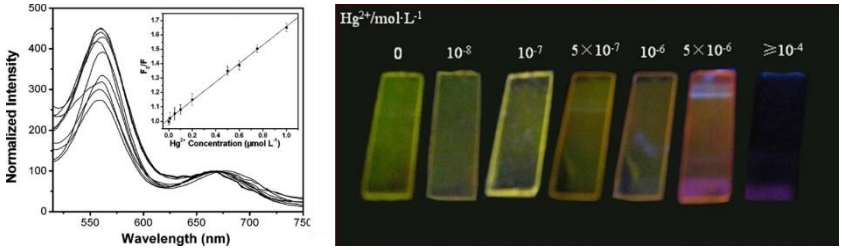

Figure 2.9. (a) Luminescence spectra of the bi-color film under exposure to different Hg^{2+} concentrations: 0, 0.01, 0.05, 0.1, 0.2, 0.5, 0.6, 0.75, and 1 μM. The inset shows the Stern-Volmer plot of the sensor. (b) Colors of the sensing films under exposure to different Hg^{2+} concentrations: 0, 0.01, 0.1, 0.5, 1, 1.5 and higher than 100 μM. Reprinted from [105] with permission from Elsevier.

Apart from CdTe QDs, carbon nanoparticles have also been employed for the fabrication of Hg(II) sensitive luminescent films [106]. Their functionalization with PEG200 and N-acetyl-L-cysteine (NAC) made possible the assembly of the carbon dots with PEI onto the tapered tip of a 600 μm-core optical fiber by means of the LbL technique, as well as the detection of mercury ions. Although the fluorescence quenching mechanism of these sensors was not completely determined, it was likely to be due to the interaction between the –SH groups of NAC and Hg(II) ions. Sensing coatings from 1 to 6 bilayers of (PEI/Carbon dots) were analyzed: all of them exhibited a reproducible and reversible behavior towards Hg(II) (see Figure 2.10 for the particular case of the 6 layers structure), and it was found that an increase of the number of bilayers led to a decrease of the detection limit (0.1 μM Hg(II) for one bilayer and 0.01 μM Hg (II) for six bilayers) and an increase of the quenching constant. However, cross-sensitivity towards other metal ions was not studied.

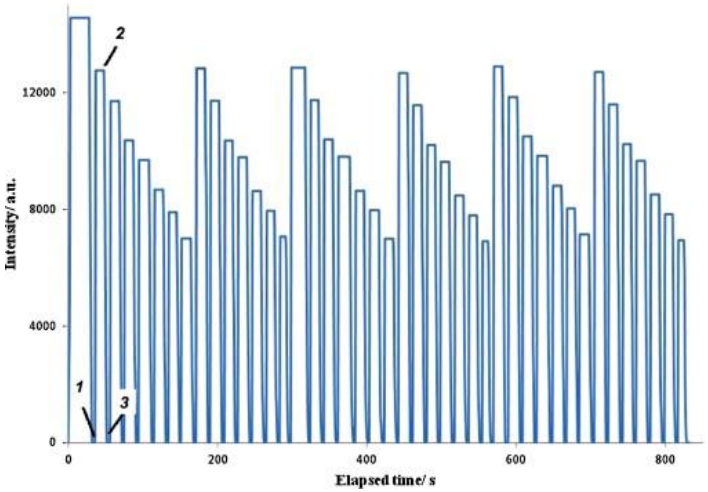

Figure 2.10. Steady-state fluorescence measurements over time (λ_{ex} = 380 nm, λ_{em} = 500 nm) of the dry optical fiber with six layers, immersed in Hg(II) aqueous solutions with in the following concentrations: 0, 0.01, 0.05, 0.1, 0.799, 1.99 and 2.69 μM. (1) The fiber was immersed in water, (2) removed from water, and (3) immersed in Hg(II) 0.01 μM. Reprinted from [106] with permission from Elsevier.

An ultrasensitive Cu(II) sensor was developed taking advantage of the fluorescence enhancement produced by Ag nanoprisms onto 16-mercaptohexadecanoic acid (16-MHA) capped CdSe quantum dots (QDs) [107]. Si or glass slides were coated by a layer of silver nanoprisms, which was separated from the outer QDs layer by a (PDDA/PSS) spacer of the optimal thickness [108] fabricated by means of LbL. The Ag nanoprisms, together with a UV photobrightening process, enhanced the luminescence, which was selectively quenched by Cu^{2+} ions, with a detection limit as low as 5 nM. The enhancement produced by the photobrightening and the Ag nanoprisms is clearly observable in Figure 2.11.

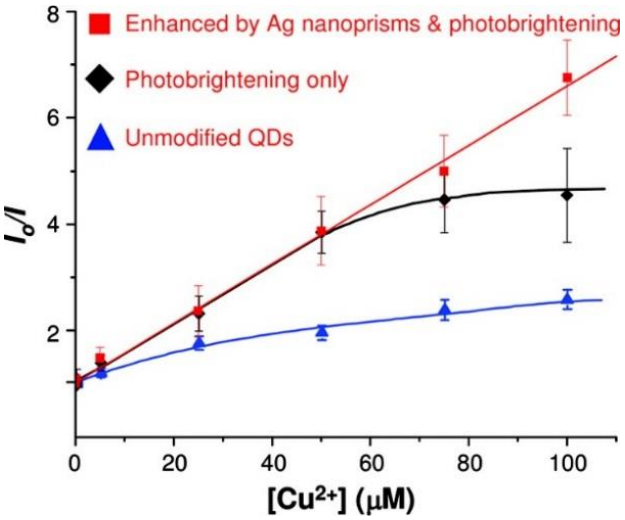

Figure 2.11. Stern–Volmer plot for the quenching of CdSe PL by Cu^{2+}. Reprinted from [107] with permission from Elsevier.

Table 2.3 summarizes all the metal ion sensors analyzed in this section.

Analyte	Sensitive indicator	Sensing film	Detection range	LOD	Cross Sens	Ref
Fe^{3+}, Hg^{2+}	HPTS	$[PAH/PAA\text{-}HPTS]_n$	0 – 0.5 mM Fe^{3+} 0 – 1 mM Hg^{2+}	1.28 ppm Fe^{3+} 1.79 ppm Hg^{2+}	-	[98], [99]
Hg^{2+}	TPPS	(PDDA/PSS/PDDA/TPPS)	0 – $3.3 \cdot 10^{-5}$ M	< $3.3 \cdot 10^{-8}$ M	Cd^{2+}, Pb^{2+}, Cu^{2+}	[100]
Hg^{2+}	$PPESO_3$	$(PDDA/PPESO_3)_3$	0 – 1 mM	10^{-7} M	Fe^{3+}, Al^{3+}	[102]
Fe^{3+}	PFPNa	$(PDDA/PFPNa)_1$	0 – 10 μM	10^{-7} M	-	[101]
Hg^{2+}	MSA-capped CdTe QDs	$(PDDA/QDs)_{10}$	0 – 1 μM	< 10^{-8} M	Cu^{2+}, Ag^{1+}	[103]
Cu^{2+}, Hg^{2+}	MSA-capped CdTe QDs	$(PDDA/QDs)_5$	0 – 1 μM Cu^{2+} 0 – 0.5 μM Hg^{2+}	< 10^{-8} M Cu^{2+} < $5 \cdot 10^{-9}$ M Hg^{2+}	High concs. of Ni^{2+}, Cr^{3+}, Au^{3+}, Ag^{+}	[104]
Hg^{2+}	MPA-capped CdTe QDs	$(PDDA/QDs)_5/PDDA/PSS/PDDA/(QDs)_5/BSA$	0.01 – 1 μM	$4.5 \cdot 10^{-9}$ M	-	[105]
Hg^{2+}	Carbon dots	$(PEI/Carbon\ dots)_{1\text{-}6}$	0.01 – 2.69 μM for $(PEI/Carbon\ dots)_6$	10^{-8} M for $(PEI/Carbon\ dots)_6$	-	[106]
Cu^{2+}	(16-MHA) capped CdSe QDs	Ag NPs /(PDDA/PSS)/QDs	0 – 100 μM	$5 \cdot 10^{-9}$ M	-	[107]

Table 2.3. Luminescent films fabricated by LbL for ions detection.

2.3.2. LbL luminescent coatings for dissolved oxygen sensing

In neutral solutions singlet oxygen ($^1O_2$) reacts with ascorbate (AscH) producing H_2O_2, which quenches the fluorescent emission of CdTe QDs [109]. Taking advantage of this reaction, a singlet oxygen sensitive coating was fabricated by means of the LbL technique [110]: first, a glass slide was coated with the base layers $(PDDA/PAA)_3$/PDDA, onto which ten bilayers of (CdTe QDs/PDDA) were deposited. With the aim of avoiding any interference between the CdTe QDs and the ascorbate, a spacer structure $(PDDA/PAA)_2$/PDDA was introduced and, finally, two bilayers of PDDA/ascorbate were built. The sensing films were introduced in a phenylalanine solution, which produced singlet oxygen under UV illumination. Then, $^1O_2$ reacted with ascorbate producing H_2O_2, which etched the QDs surface, giving rise to their luminescence quenching, as it is shown in Figure 2.12.

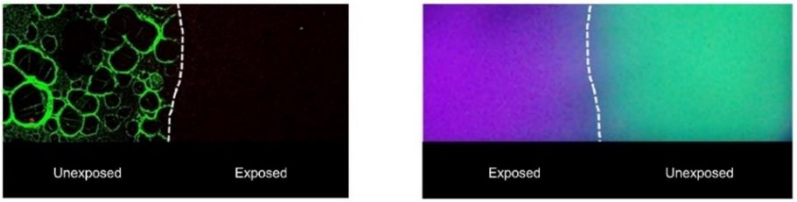

Figure 2.12. (a) Microscopic image of the interface between a part exposed to phenylalanine (right) and a part unexposed (left). (b) UV image of the phenylalanine-exposed part (left), where only the UV light (excitation) is visible, and the unexposed part (right), where the luminescence (534 nm, green) is observable. Reprinted from [110] with the permission from Korean Chemical Society.

This sensing structure detected $^1O_2$ concentration as low as 10^{-15} M, as shown in Figure 2.13, where the luminescent intensity of the sensing film after incubation in solutions of different phenylalanine concentrations and the calibration curve are displayed. For each concentration, intensity decreased for 5 minutes, when a steady stage was reached. This response

time was thought to be due to the time required by H_2O_2 to etch the QDs [48].

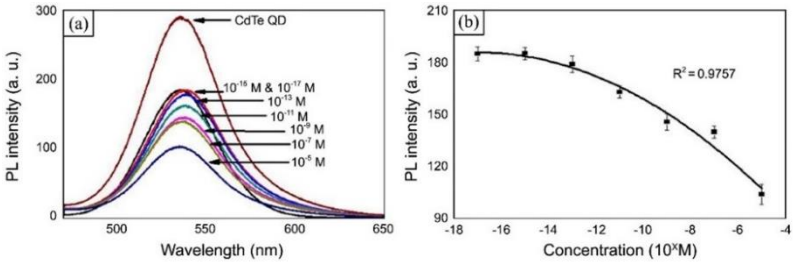

(a) (b)

Figure 2.13. (a) Luminescent intensity of the film before and after incubation in solutions of different phenylalanine concentrations, and (b) the corresponding calibration curve. After incubation and exposition to UV light, singlet oxygen is produced, which reacts with ascorbate producing H_2O_2, which quenches the luminescence. Reprinted from [110] with the permission from Korean Chemical Society.

Other dissolved oxygen sensors were developed by utilizing ruthenium porphyrins as sensitive materials. For instance, Grant and coworkers fabricated a self-referenced optical fiber sensor based on a polymer/polymer-dye multilayer structure, by combining the oxygen sensitive porphyrin bis(2,2'-bipyridine)''-methyl-4-carboxybipyridine-ruthenium-N-succinimidyl-ester bis(hexafluoro-phosphate), $Ru(bpy)_2(mcbpy)$, with PAH and the reference dye, FITC, with the same cationic polyelectrolyte [111]. The multilayer architecture $(PAH\text{-}Ru(bpy)_2(mcbpy)/PSS)_{10}$ + $\{PAH\text{-}FITC/PSS)_5$ was built on the tip of a 400 μm-core optical fiber, which was connected to a two (200 μm) to one (400 μm) coupler. Under illumination at 450 nm, the sensing film exhibited two luminescent peaks, centered at 524 nm and 630 nm, which corresponded to the two dyes, FITC and $Ru(bpy)_2(mcbpy)$ respectively. The fluorescence peak ratio (I_{630nm}/I_{524nm}) changed from 0.82 to 0.75 under dissolved oxygen concentration variations from 0 to 1400 mM.. In a subsequent research [112] the number of dye layers was increased up to 15, but no enhancement of the sensor performance was observed.

A study of the adsorption of Ru(bpy) onto planar substrates by LbL was performed in [113]: this porphyrin was attempted to be assembled from a pure dye solution as well as from solutions of different dye-polyion concentrations. In the first case, the multilayer structure PEI/(PSS/PDDA)$_2$/(PSS/Ru(bpy))$_{20}$ was deposited onto glass slides. Despite Ru(bpy) was positively charged, it was observed that it was barely adsorbed to PSS and, what is more, it was desorbed when the substrates were immersed in the anionic solution. When mixing Ru(bpy) with PSS, sensing coatings with the structure PEI/(PSS/PDDA)$_2$/(PSS-Ru(bpy)/PDDA)$_{20}$ and different ratios of Ru(bpy):PSS (1:80, 1:40 and 1:20) were analyzed. As the Ru(bpy):PSS ratio increased, also did the fluorescence intensity. The fluorescence quenching of the sensor fabricated with the 1:20 (Ru(bpy):PSS) ratio exhibited a Stern-Volmer trend, being able to detect changes of less than the 3% of the dissolved oxygen concentration in the range between 0 and 12 mg/L. This fact made it suitable for monitoring oxygen concentrations within biological environments. However, a further investigation [114] concluded that the best approach for adsorbing the luminescent dye to the substrate was not the polyelectrolyte-dye mixing, but their covalent linkage: this bond prevented any kind of dye desorption when the substrate was immersed into the oppositely charged solution.

2.3.3. LbL luminescent films for biosensing applications

Li et al used the multilayer structure (PAH/CdTe QDs)$_x$(PAH/PSS)$_3$(PAH/GO)$_y$ to determine the concentration of blood glucose in real serum samples with good reproducibility and accuracy [48]: the GO enzyme catalysed the reaction between oxygen and glucose producing H_2O_2, which etches the surface of the QDs, quenching their luminescence. Under illumination at 380 m, the initial structure (PAH/CdTe QDs)$_{12}$(PAH/PSS)$_3$(PAH/GO)$_3$ showed a luminescence peak centered at 630 nm. The luminescent properties of this coating were analyzed for different temperature and pH values in the ranges from 28 to 45 ^{o}C, and from 6 to 9, respectively. In the case of temperature, the largest quenching rate was obtained for 37 ^{o}C, whereas a pH value of 7.4

was chosen as the optimal one. Figure 2.14 shows the luminescence quenching of that structure at different temperatures (a), upon different glucose concentrations (b), and in Figure 2.15 the absolute quenching rate of this structure is plotted.

Under those conditions (at 37 ^{o}C and pH 7.4), the response upon addition of 4 mM glucose of three different structures (as shown in Figure 2.16) was studied with the aim of optimizing the number of (PAH/CdTe QDs) and (PAH/GOD) bilayers.

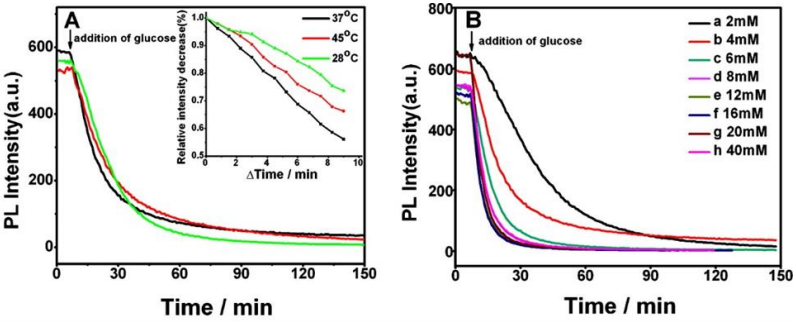

Figure 2.14. (a) Quenching of the luminescence peak centered at 630 nm of the multilayer structure $(PAH/CdTe)_{12}(PAH/PSS)_3(PAH/GOD)_3$ when it is exposed to a 4 mM glucose solution at different temperatures. The time-dependent luminescence intensity of that peak during the first 9 minutes of the reaction for each temperature is shown in the inset. (b) Luminescence quenching of the same film for different glucose concentrations: (a) 2, (b) 4, (c) 6, (d) 8, (e) 12, (f) 16, (g) 20, and (h) 40 mM over 150 minutes. Copyright 2009 American Chemical Society.

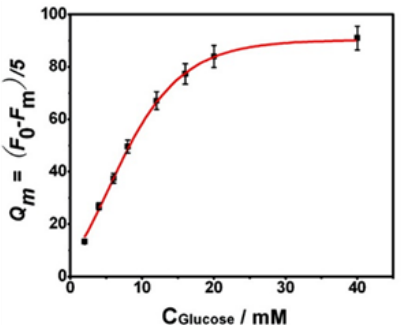

Figure 2.15. Quenching rate (Q_m) of the sensor over 5 minutes as a function of the glucose concentration. F_0 and F_m correspond to the luminescence intensity in the absence (F_0) and presence (F_m) of glucose. All measurements were carried out in a 20 mM phosphate buffer at pH 7.4. Copyright 2009 American Chemical Society.

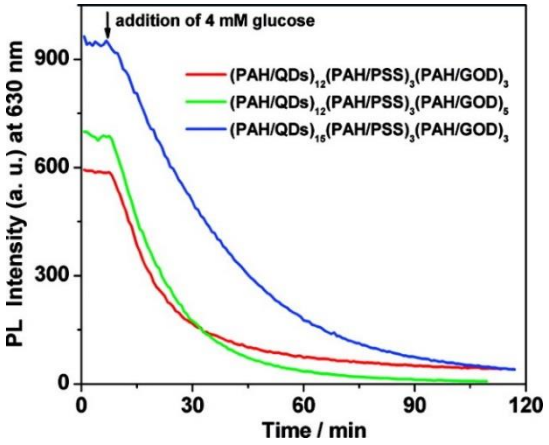

Figure 2.16. Luminescence quenching at 630 nm (λ_{ex} = 380 nm) when different structures of (PAH/CdTe QDs)$_x$(PAH/PSS)$_3$(PAH/GOD)$_y$ were exposed to 4 mM glucose. All measurements were carried out at 37 ^{o}C in a 20 mM phosphate buffer at pH 7.4. Copyright 2009 American Chemical Society.

For a given number of (PAH/GOD) bilayers (in this case, 3), it was observed that the quenching rate of the sensor decreased with the

increase of the number of QDs layers was fixed at 12. For this amount of (PAH/CdTe QDs) bilayers, the quenching constant increased linearly with the number of enzyme layers as a consequence of the good permeability of the GOD layers towards glucose. The $(PAH/PSS)_3$ spacer was introduced in order to avoid any kind of influence of the GOD-glucose reaction on the QDs. The structure $(PAH/CdTe\ QDs)_{12}(PAH/PSS)_3(PAH/GOD)_5$ was chosen as the optimal for determining blood glucose concentration in serum samples: it exhibited a linear luminescence quenching in the glucose concentration range between 0.5 – 16 mM, being 0.5 mM the detection limit. Furthermore, no sample pretreatment was needed.

Since it was isolated, graphene and some related structures have been employed for diverse sensing applications [115]. Graphene oxide multilayer arrays were assembled by means of the LbL technique by Jung et al [116] for the fabrication of aptasensor microarrays. These multilayers were prepared by assembling oppositely charged graphene oxide sheets: negatively charged ones (GO^-) were prepared by introducing COOH groups, while the positively charged sheets (GO^+) were obtained thanks to the NH_2 groups. An aminated glass slide was coated with ten bilayers of (GO^-/GO^+), and then FAM-labeled thrombin aptamer was immobilized on them. The FAM luminescence, centered at 530 nm, was quenched by graphene oxide, due to the high energy transfer between the dye and graphene. In the presence of thrombin, fluorescence was recovered owing to the high affinity between aptamers and thrombin. Oppositely, other analytes such as bovine serum albumin (BSA), streptavidin (STA), glucose, or human immunoglobin (IgG) antibody did not altered the quenched fluorescence of FAM-aptamer-labeled GO multilayers, probing the high specificity of the aptamer-based sensor. For the particular case of ten bilayers of (GO^-/GO^+) and 2 μM aptamer concentration, the fluorescence intensity from FAM was quenched over 85% and the detection limit for thrombin was 0.001 nM, exhibiting 30-fold higher sensitivity than the solution-based graphene FRET aptasensor [117]. Furthermore, this sensor was reused four times by simply cleaning it with distilled water.

2.3.4. LbL luminescent coating for gaseous oxygen sensing

Another approach to immobilize these ruthenium porphyrins into the multilayer structures consisted of the fabrication of the multilayer film and its further immersion in the dye solution, with the consequent diffusion of the indicator inside the coating. In [118], three kind of sensors were fabricated onto the tip of 62.5 μm-core optical fiber. The first type consisted of a hygroscopic polymer membrane made of polyglutamic acid (PGA, anionic material) and poly-Lysine (cationic material). The second coating was a water absorbing polymer membrane composed of PAA (anionic polyelectrolyte) and PAH (cationic polyelectrolyte) and the third one, a porous composite membrane, was a multilayer structure of porous glass beads and PAH built onto a PAA layer. After the deposition of 50 bilayers of each structure onto the optical fiber tips, they were immersed in 80 mM Ru(bpy) solutions. When the sensors were illuminated at 450 nm, no phosphorescence was observed in the case of the water absorbing polymer membrane, whereas the hygroscopic polymer membrane and the porous composite membrane exhibited a phosphorescent peak centered at 625 nm, being the last one, the only one that was quenched when the sensor was exposed to 95-100% oxygen concentrations. Apart from the influence of the multilayer structure on the behavior of the sensors, the effect of the number of pairs of layers was also studied. It was found that a 125-bilayers structure did not show phosphorescence, which was attributed to the difficulty of introducing the ruthenium porphyrin in such a thick membrane. On the other hand, the 5-bilayers sensor had a similar sensitivity to that of 50-bilayers, and it also demonstrated a high resolution for low oxygen concentrations. Although in this work the influence of the embedding matrix on the sensor's performance was studied, no research about the distribution of the indicator inside these matrices has been carried out. What is more, these indicator was not deposited by LbL, but in a coating that had been previously fabricated employing that technique.

It is important to remark the lack of previous works related to the fabrication of optical oxygen gas sensors by means of LbL. This could be perhaps explained by the fact that most of the oxygen fluorophores, such

as metallic porphyrins are water-insoluble. This PhD thesis will be focused on this specific topic.

2.4. Challenges of the LbL assembly of luminescent materials

One of the requirements for the utilization of the LbL as a fabrication technique is the need of the materials to be dissolved in water-based solutions. Thus, in principle, all the materials that are going to be deposited by this method must be water-soluble, what constitutes a restriction on the compounds used as indicators. The overcoming of this drawback would open the door to the utilization of new materials: for instance, there exists a wide variety of optically and chemically stable porphyrins that have never been used for the fabrication of luminescence-based sensors by means of the LbL technique, such as platinum metalloporphyrins.

Besides, it would be of great interest to analyze the parameters of the sensing films that determine the behavior of that kind of sensors. Apart from the number of deposited bilayers, which has been the subject of study in previous works (although water-insoluble indicators were not employed), there are other properties that influence the sensitivity and kinetics of these sensors, for instance, their behavior towards water, their morphology or the distribution of the luminophores inside the sensing films. Analyzing the relevance of each one of the above mentioned parameters would shed light for the optimization of these sensors.

Luminescence-based sensors must also struggle with the self-quenching effect. In this respect, utilizing the LbL as the fabrication technique would permit to tailor the spacing distance between the luminescent layers, not only leading to more homogeneous distribution of the luminophores inside the films, but also attenuating the self-quenching effect.

2.5. Conclusions

It is obvious that luminescence has become a powerful detection mechanism for biological and environmental applications. This sensing method also takes advantage of the wide variety of sensitive luminophores that exists: fluoropolymers, porphyrins or semiconductor quantum dots, among others. These materials can be encapsulated in multilayer shells for their utilization in solution-based probes, or they can be entrapped inside nanostructured films and used as solid-state sensors. In both cases, the LbL nano-assembly technique permits to tailor the properties of the sensors in the nanometer scale, making feasible the fabrication of custom-made devices that not only exhibit good photostability, but also high selectivity and sensitivity for almost any kind of sensing applications.

The remarkable characteristics of the sensors exposed in this study suggest that the combination of luminescence and the LbL nano-assembly technique is a promising approach for the fabrication of sensing devices for real applications. Environmental and biosensing purposes are probably the most encouraging fields, owing to the facility for fabricating arrays of sensor capable of detecting several analytes with a single measurement. Because of all these features, a deeper research in the field of luminescent sensors built up by the LbL approach has been carried out, giving rise to the current PhD thesis.

Up to now, water-insoluble materials have been barely used for the fabrication of luminescence-based sensors by means of the LbL technique. This difficulty perhaps justify the lack of works related to the fabrication of oxygen gas sensors by means of the LbL. This challenge will be dealt with in the following chapter. The achievement of this goal, together with the versatility of the LbL to tailor the properties of the multilayer films could lead to the development of highly optimized sensors in terms of sensitivity and kinetics.

Bibliography

1. Sun, C.; Chen, Y.; Zhang, G.; Wang, F.; Liu, G.; Ding, J. Multipoint Remote Methane Measurement System Based on Spectrum Absorption and Reflective TDM. *IEEE Photonics Technology Letters* **2016**, *28*, doi:10.1109/LPT.2016.2601625.
2. Pasinszki, T.; Krebsz, M.; Tung, T. T.; Losic, D. Carbon nanomaterial based biosensors for non-invasive detection of cancer and disease biomarkers for clinical diagnosis. *Sensors (Switzerland)* **2017**, *17*, doi:10.3390/s17081919.
3. Tan, C. H.; Tan, S. T.; Lee, H. B.; Ginting, R. T.; Oleiwi, H. F.; Yap, C. C.; Jumali, M. H. H.; Yahaya, M. Automated room temperature optical absorbance CO sensor based on In-doped ZnO nanorod. *Sensors and Actuators, B: Chemical* **2017**, *248*, doi:10.1016/j.snb.2017.02.161.
4. Del Villar, I.; Arregui, F. J.; Zamarreño, C. R.; Corres, J. M.; Bariain, C.; Goicoechea, J.; Elosua, C.; Hernaez, M.; Rivero, P. J.; Socorro, A. B.; Urrutia, A.; Sanchez, P.; Zubiate, P.; Lopez, D.; De Acha, N.; Ascorbe, J.; Matias, I. R. Optical sensors based on lossy-mode resonances. *Sensors and Actuators, B: Chemical* **2017**, *240*, doi:10.1016/j.snb.2016.08.126.
5. Qazi, H. H.; Bin Mohammad, A. B.; Akram, M. Recent Progress in Optical Chemical Sensors. *Sensors* **2012**, *12*, 16522–16556, doi:10.3390/s121216522.
6. Baldini, F.; Bacci, M.; Cosi, F.; Del Bianco, A. Absorption-based optical-fibre oxygen sensor. *Sensors and Actuators: B. Chemical* **1992**, *7*, doi:10.1016/0925-4005(92)80398-H.
7. Miki, H.; Matsubara, F.; Nakashima, S.; Ochi, S.; Nakagawa, K.; Matsuguchi, M.; Sadaoka, Y. A fractional exhaled nitric oxide sensor based on optical absorption of cobalt tetraphenylporphyrin derivatives. *Sensors and Actuators, B: Chemical* **2016**, *231*, doi:10.1016/j.snb.2016.02.145.
8. Zhang, W.; Ye, W.; Wang, C.; Li, W.; Yue, Z.; Liu, G. Silver nanoparticle arrays enhanced spectral surface plasmon resonance optical sensor. *Micro and Nano Letters* **2014**, *9*, doi:10.1049/mnl.2014.0203.
9. Pedro J. Rivero; A. Urrutia; J. Goicoechea; I. R. Matías; F. J. Arregui; A Lossy Mode Resonance optical sensor using silver nanoparticles-loaded films for monitoring human breathing. *Sensors and Actuators B: Chemical* **2013**, *187*, 40–44, doi:10.1016/J.SNB.2012.09.022.
10. Marques, L.; Hernandez, F. U.; Korposh, S.; Clark, M.; Morgan, S.; James, S.; Tatam, R. P. Sensitive protein detection using an optical fibre long period grating sensor anchored with silica core gold shell nanoparticles. In; SPIE, 2014; Vol. 9157.
11. Payne, S. J.; Fiore, G. L.; Fraser, C. L.; Demas, J. N. Luminescence oxygen sensor based on a ruthenium(II) star polymer complex. *Analytical Chemistry* **2010**, *82*, doi:10.1021/ac9020837.
12. Bian, W.; Ma, J.; Liu, Q.; Wei, Y.; Li, Y.; Dong, C.; Shuang, S. A novel phosphorescence sensor for Co^{2+} ion based on Mn-doped ZnS quantum dots. *Luminescence* **2014**, *29*, doi:10.1002/bio.2520.
13. Ferrari, L.; Rovati, L.; Fabbri, P.; Pilati, F. Disposable fluorescence optical pH sensor for near neutral solutions. *Sensors (Switzerland)* **2013**, *13*, doi:10.3390/s130100484.

14. Hong-Shui Lv; Shu-Ya Huang; Bao-Xiang Zhao; Jun-Ying Miao; A new rhodamine B-based lysosomal pH fluorescent indicator. *Analytica Chimica Acta* **2013**, *788*, 177–182, doi:10.1016/J.ACA.2013.06.038.
15. Ross, D.; Gaitan, M.; Locascio, L. E. Temperature measurement in microfluidic systems using a temperature-dependent fluorescent dye. *Analytical Chemistry* **2001**, *73*, doi:10.1021/ac0103701.
16. Song, C; Zhi, A; Liu, Q; Yang, J; Jia, G; Shervin, J; Tang, L; Hu, X; Deng, R; Xu, C; Zhang, G. Rapid and sensitive detection of β-agonists using a portable fluorescence biosensor based on fluorescent nanosilica and a lateral flow test strip. *Biosensors and Bioelectronics* **2013**, *50*, 62–65, doi:10.1016/J.BIOS.2013.06.022.
17. Yoshihara, T.; Murayama, S.; Tobita, S. Ratiometric molecular probes based on dual emission of a blue fluorescent coumarin and a red phosphorescent cationic iridium(III) complex for intracellular oxygen sensing. *Sensors (Switzerland)* **2015**, *15*, doi:10.3390/s150613503.
18. Zhang, H.; Zhang, G.; Xu, J.; Wen, Y.; Lu, B.; Zhang, J.; Ding, W. Novel highly selective fluorescent sensor based on electrosynthesized poly(9-fluorenecarboxylic acid) for efficient and practical detection of iron(III) and its agricultural application. *Sensors and Actuators B: Chemical* **2016**, *230*, 123–129, doi:10.1016/j.snb.2016.02.046.
19. Kuo-xi Xu; Xin-mei Xie; Hua-jie Kong; Ping Li; Jing-lai Zhang; Xiao-bin Pang; Selective fluorescent sensors for malate anion using the complex of phenanthroline-based Eu(III) in aqueous solution. *Sensors and Actuators B: Chemical* **2014**, *201*, 131–137, doi:10.1016/J.SNB.2014.04.086.
20. Kuo, S.-Y.; Li, H.-H.; Wu, P.-J.; Chen, C.-P.; Huang, Y.-C.; Chan, Y.-H. Dual colorimetric and fluorescent sensor based on semiconducting polymer dots for ratiometric detection of lead ions in living cells. *Analytical Chemistry* **2015**, *87*, doi:10.1021/ac504845t.
21. Chang, J; Li, H; Hou, T; Li, F. Paper-based fluorescent sensor for rapid naked-eye detection of acetylcholinesterase activity and organophosphorus pesticides with high sensitivity and selectivity. *Biosensors and Bioelectronics* **2016**, *86*, 971–977, doi:10.1016/J.BIOS.2016.07.022.
22. Chao, M. R.; Hu, C. W.; Chen, J. L. Glass substrates crosslinked with tetracycline-imprinted polymeric silicate and CdTe quantum dots as fluorescent sensors. *Analytica Chimica Acta* **2016**, *925*, 61–69, doi:10.1016/J.ACA.2016.04.037.
23. Hale, Z. M.; Payne, F. P. Fluorescent sensors based on tapered single-mode optical fibres. *Sensors and Actuators B: Chemical* **1994**, *17*, 233–240, doi:10.1016/0925-4005(93)00876-Z.
24. Shang, Z. B.; Wang, Y.; Jin, W. J. Triethanolamine-capped CdSe quantum dots as fluorescent sensors for reciprocal recognition of mercury (II) and iodide in aqueous solution. *Talanta* **2009**, *78*, doi:10.1016/j.talanta.2008.11.025.
25. Kim, Y.; Chang, J. Y. Fabrication of a fluorescent sensor by organogelation: CdSe/ZnS quantum dots embedded molecularly imprinted organogel nanofibers. *Sensors and Actuators, B: Chemical* **2016**, *234*, doi:10.1016/j.snb.2016.04.161.
26. Wang, H.; He, Y. Recent advances in silicon nanomaterial-based fluorescent sensors. *Sensors (Switzerland)* **2017**, *17*, doi:10.3390/s17020268.

27. Senkbeil, S.; Lafleur, J. P.; Jensen, T. G.; Kutter, J. P. Gold nanoparticle-based fluorescent sensor for the analysis of dithiocarbamate pesticides in water. In *Proceedings of the 16th International Conference on Miniaturized Systems for Chemistry and Life Sciences, MicroTAS 2012*; 2012.
28. Gilliard Jr., R. J.; Iacono, S. T.; Budy, S. M.; Moody, J. D.; Smith Jr., D. W.; Smith, R. C. Chromophore-derivatized semifluorinated polymers for colorimetric and turn-on fluorescent anion detection. *Sensors and Actuators, B: Chemical* **2009**, *143*, doi:10.1016/j.snb.2009.08.047.
29. Payman, Hashemi; Razieh Afzari, Z. A wide range pH optical sensor with mixture of Neutral Red and Thionin immobilized on an agarose film coated glass slide. *Sensors and Actuators B: Chemical* **2008**, *135*, 112–115, doi:10.1016/J.SNB.2008.08.010.
30. M.Amini;, A. A. E. A highly selective optical sensor for catalytic determination of ultra-trace amounts of nitrite in water and foods based on brilliant cresyl blue as a sensing reagent. *Sensors and Actuators B: Chemical* **2010**, *147*, 61–66, doi:10.1016/J.SNB.2010.03.014.
31. Magna, G.; Catini, A.; Kumar, R.; Palmacci, M.; Martinelli, E.; Paolesse, R.; di Natale, C. Conductive photo-activated porphyrin-ZnO nanostructured gas sensor array. *Sensors (Switzerland)* **2017**, *17*, doi:10.3390/s17040747.
32. Cheng-Shane, Chu; Chih-Yung, C. Highly sensitive fiber-optic oxygen sensor based on palladium tetrakis (4-carboxyphenyl)porphyrin doped in ormosil. *Journal of Luminescence* **2014**, *154*, 475–478, doi:10.1016/J.JLUMIN.2014.05.025.
33. Roales, J.; Pedrosa, J. M.; Guillén, M. G.; Lopes-Costa, T.; Castillero, P.; Barranco, A.; González-Elipe, A. R. Free-base carboxyphenyl porphyrin films using a TiO<inf>2</inf> columnar matrix: Characterization and application as NO<inf>2</inf> sensors. *Sensors (Switzerland)* **2015**, *15*, doi:10.3390/s150511118.
34. Nivens, D. A.; Zhang, Y.; Angel, S. M. A fiber-optic pH sensor prepared using a base-catalyzed organo-silica sol–gel. *Analytica Chimica Acta* **1998**, *376*, 235–245, doi:10.1016/S0003-2670(98)00505-4.
35. Sas, S.; Danko, M.; Bizovská, V.; Lang, K.; Bujdák, J. Highly luminescent hybrid materials based on smectites with polyethylene glycol modified with rhodamine fluorophore. *Applied Clay Science* **2017**, *138*, doi:10.1016/j.clay.2016.12.034.
36. Mollarasouli, K. A.-Z. F. A novel and facile synthesis of TGA-capped CdSe@Ag2Se core-shell quantum dots as a new substrate for high sensitive and selective methyldopa sensor. *Sensors and Actuators B: Chemical* **2016**, *237*, 387–399, doi:10.1016/J.SNB.2016.06.116.
37. Lu, D.; Yang, L.; Tian, Z.; Wang, L.; Zhang, J. Core-shell mesoporous silica nanospheres used as Zn 2+ ratiometric fluorescent sensor and adsorbent. *RSC Advances* **2012**, *2*, doi:10.1039/c2ra01106a.
38. Properties and applications of proteins encapsulated within sol–gel derived materials. *Analytica Chimica Acta* **2002**, *461*, 1–36, doi:10.1016/S0003-2670(02)00229-5.
39. Guan, W.; Zhou, W.; Lu, J.; Lu, C. Luminescent films for chemo- and biosensing. *Chemical Society Reviews* **2015**, *44*, doi:10.1039/c5cs00246j.

40. Ertekin, K; Tepe, M.; Yenigül, B.; Akkaya, E. U.; Henden, H. Fiber optic sodium and potassium sensing by using a newly synthesized squaraine dye in PVC matrix. *Talanta* **2002**, *58*, 719–727, doi:10.1016/S0039-9140(02)00329-6.
41. Brolo, A. G.; Kwok, S. C.; Moffitt, M. G.; Gordon, R.; Riordon, J.; Kavanagh, K. L. Enhanced fluorescence from arrays of nanoholes in a gold film. *Journal of the American Chemical Society* **2005**, *127*, doi:10.1021/ja0548687.
42. McDonagh, C.; MacCraith, B. D.; McEvoy, A. K. Tailoring of Sol-Gel Films for Optical Sensing of Oxygen in Gas and Aqueous Phase. *Analytical Chemistry* **1998**, *70*.
43. Chu, C.-S.; Lo, Y.-L. Fiber-optic carbon dioxide sensor based on fluorinated xerogels doped with HPTS. *Sensors and Actuators, B: Chemical* **2008**, *129*, doi:10.1016/j.snb.2007.07.082.
44. Zhao, Z.; Lu, P.; Lam, J. W. Y.; Wang, Z.; Chan, C. Y. K.; Sung, H. H. Y.; Williams, I. D.; Ma, Y.; Tang, B. Z. Molecular anchors in the solid state: Restriction of intramolecular rotation boosts emission efficiency of luminogen aggregates to unity. *Chemical Science* **2011**, *2*, doi:10.1039/c0sc00521e.
45. Decher, G. Fuzzy Nanoassemblies: Toward Layered Polymeric Multicomposites. *Science* **1997**, *277*, 1232–1237, doi:10.1126/science.277.5330.1232.
46. Elzbieciak, M.; Zapotoczny, S.; Nowak, P.; Krastev, R.; Nowakowska, M.; Warszyński, P. Influence of pH on the structure of multilayer films composed of strong and weak polyelectrolytes. *Langmuir* **2009**, *25*, 3255–3259, doi:10.1021/la803988k.
47. Yang, Y.-H.; Haile, M.; Park, Y. T.; Malek, F. A.; Grunlan, J. C. Super Gas Barrier of All-Polymer Multilayer Thin Films. *Macromolecules* **2011**, *44*, 1450–1459, doi:10.1021/ma1026127.
48. Li, X.; Zhou, Y.; Zheng, Z.; Yue, X.; Dai, Z.; Liu, S.; Tang, Z. Glucose biosensor based on nanocomposite films of CdTe quantum dots and glucose oxidase. *Langmuir* **2009**, *25*, doi:10.1021/la900066z.
49. Aslan, K.; Gryczynski, I.; Malicka, J.; Matveeva, E.; Lakowicz, J. R.; Geddes, C. G. Metal-enhanced fluorescence: an emerging tool in biotechnology. *Current Opinion in Biotechnology* **2005**, *16*, 55–62, doi:10.1016/J.COPBIO.2005.01.001.
50. Ariga, K.; Hill, J. P.; Ji, Q. Layer-by-layer assembly as a versatile bottom-up nanofabrication technique for exploratory research and realistic application. *Physical Chemistry Chemical Physics* **2007**, *9*, doi:10.1039/b700410a.
51. McShane, M. J.; Brown, J. Q.; Guice, K. B.; Lvov, Y. M. Polyelectrolyte Microshells as Carriers for Fluorescent Sensors: Loading and Sensing Properties of a Ruthenium-Based Oxygen Indicator. *Journal of Nanoscience and Nanotechnology* **2002**, *2*, doi:10.1166/jnn.2002.118.
52. Arregui, F. J. *Sensors based on nanostructured materials*; 2009; ISBN 9780387777528.
53. Duchesne, T. A.; Brown, J. Q.; Guice, K. B.; Lvov, Y. M.; McShane, M. J. Encapsulation and stability properties of nanoengineered polyelectrolyte capsules for use as fluorescent sensors. *Sensors and Materials* **2002**, *14*.
54. McShane, M. J. Potential for glucose monitoring with nanoengineered fluorescent biosensors. *Diabetes Technology and Therapeutics* **2002**, *4*, doi:10.1089/152091502760306625.

55. Bornhoeft, L. R.; Biswas, A.; McShane, M. J. Composite hydrogels with engineered microdomains for optical glucose sensing at low oxygen conditions. *Biosensors* **2017**, *7*, doi:10.3390/bios7010008.
56. Zhao, Q.; Rong, X.; Chen, L.; Ma, H.; Tao, G. Layer-by-layer self-assembly xylenol orange functionalized CdSe/CdS quantum dots as a turn-on fluorescence lead ion sensor. *Talanta* **2013**, *114*, doi:10.1016/j.talanta.2013.04.016.
57. McShane, M.; Ritter, D. Microcapsules as optical biosensors. *Journal of Materials Chemistry* **2010**, *20*, doi:10.1039/c0jm01251c.
58. Antipov, A. A.; Shchukin, D.; Fedutik, Y.; Petrov, A. I.; Sukhorukov, G. B.; Möhwald, H. Carbonate microparticles for hollow polyelectrolyte capsules fabrication. *Colloids and Surfaces A: Physicochemical and Engineering Aspects* **2003**, *224*, doi:10.1016/S0927-7757(03)00195-X.
59. Biswas, A.; Nagaraja, A. T.; McShane, M. J. Fabrication of nanocapsule carriers from multilayer-coated vaterite calcium carbonate nanoparticles. *ACS Applied Materials and Interfaces* **2014**, *6*, doi:10.1021/am5061195.
60. Biswas, A.; Banerjee, S.; Gart, E. V.; Nagaraja, A. T.; McShane, M. J. Gold Nanocluster Containing Polymeric Microcapsules for Intracellular Ratiometric Fluorescence Biosensing. *ACS Omega* **2017**, *2*, doi:10.1021/acsomega.7b00199.
61. Zhang, G.; Shu, F. P.; Robinson, C. J. Design and characterization of a nano-encapsulated self-referenced fluorescent nitric oxide sensor for wide-field optical imaging. In *Annual International Conference of the IEEE Engineering in Medicine and Biology - Proceedings*; 2007.
62. Brown, J. Q.; Lvov, Y. M.; McShane, M. J. Nanoengineered polyelectrolyte microcapsules as fluorescent potassium ion sensors. In *Annual International Conference of the IEEE Engineering in Medicine and Biology - Proceedings*; 2002; Vol. 2.
63. Lee, D.; Rubner, M. F.; Cohen, R. E. Formation of nanoparticle-loaded microcapsules based on hydrogen-bonded multilayers. **2005**, *17*, 1099–1105, doi:10.1021/cm048441v.
64. Marinakos, S. M.; Novak, J. P.; Brousseau III, L. C.; House, A. B.; Edeki, E. M.; Feldhaus, J. C.; Feldheim, D. L. Gold particles as templates for the synthesis of hollow polymer capsules. Control of capsule dimensions and guest encapsulation. *Journal of the American Chemical Society* **1999**, *121*, doi:10.1021/ja990945k.
65. Donath, E.; Sukhorukov, G. B.; Caruso, F.; Davis, S. A.; Möhwald, H. Novel hollow polymer shells by colloid-templated assembly of polyelectrolytes. *Angewandte Chemie - International Edition* **1998**, *37*.
66. Sadovoy, A.; Teh, C. Encapsulated biosensors for advanced tissue diagnostics. In *Biophotonics for Medical Applications*; Elsevier, 2015; pp. 321–330 ISBN 9780857096623.
67. He, C.; Hu, Y.; Yin, L.; Tang, C.; Yin, C. Effects of particle size and surface charge on cellular uptake and biodistribution of polymeric nanoparticles. *Biomaterials* **2010**, *31*, doi:10.1016/j.biomaterials.2010.01.065.
68. Sukhorukov, G. B.; Donath, E.; Lichtenfeld, H.; Knippel, E.; Knippel, M.; Budde, A.; Möhwald, H. Layer-by-layer self assembly of polyelectrolytes on colloidal particles. *Colloids and Surfaces A: Physicochemical and Engineering Aspects* **1998**, *137*, doi:10.1016/S0927-7757(98)00213-1.

69. Bertrand, P.; Jonas, A.; Laschewsky, A.; Legras, R. Ultrathin polymer coatings by complexation of polyelectrolytes at interfaces: Suitable materials, structure and properties. *Macromolecular Rapid Communications* **2000**, *21*.
70. Shiratori, S. S.; Rubner, M. F. pH-dependent thickness behavior of sequentially adsorbed layers of weak polyelectrolytes. *Macromolecules* **2000**, *33*, 4213–4219, doi:10.1021/ma991645q.
71. Mendelsohn, J. D.; Barrett, C. J.; Chan, V. V.; Pal, A. J.; Mayes, A. M.; Rubner, M. F. Fabrication of microporous thin films from polyelectrolyte multilayers. **2000**, *16*, 5017–5023, doi:10.1021/la000075g.
72. Zhang, G.; Shitole, P. S.; Pujari, R. A.; Charnani, V. S.; McShane, M. J.; Robinson, C. J. Intrinsic optical signal imaging of a ratiometric fluorescence oxygen nanosensor. In *2005 3rd IEEE/EMBS Special Topic Conference on Microtechnology in Medicine and Biology*; 2005; Vol. 2005.
73. Guice, K. B.; Lvov, Y. M.; McShane, M. J. Nanoengineered microcapsules for the fluorescent sensing of oxygen 2nd Joint Conference of the IEEE Engineering in Medicine and Biology Society and the Biomedical Engineering Society. In *Annual International Conference of the IEEE Engineering in Medicine and Biology - Proceedings*; 2002; Vol. 2.
74. Zheng-Liang Zhi, Faaizah Khan, J. C. P. Multilayer nanoencapsulation: A nanomedicine technology for diabetes research and management. *Diabetes Research and Clinical Practice* **2013**, *100*, 162–169, doi:10.1016/J.DIABRES.2012.11.027.
75. Saxl T, Khan F, Matthews DR, Zhi ZL, Rolinski O, Ameer-Beg S, P. J. Fluorescence lifetime spectroscopy and imaging of nano-engineered glucose sensor microcapsules based on glucose/galactose-binding protein. *Biosensors and Bioelectronics* **2009**, *24*, 3229–3234, doi:10.1016/J.BIOS.2009.04.003.
76. Acquah, I.; Roh, J.; Ahn, D. J. Dual-fluorophore silica microspheres for ratiometric acidic pH sensing. *Macromolecular Research* **2017**, doi:10.1007/s13233-017-5117-6.
77. Afkhami, A.; Soltani-Felehgari, F.; Madrakian, T.; Ghaedi, H.; Rezaeival, M. Fabrication and application of a new modified electrochemical sensor using nano-silica and a newly synthesized Schiff base for simultaneous determination of Cd2+, Cu2+ and Hg2+ ions in water and some foodstuff samples. *Analytica Chimica Acta* **2013**, *771*, 21–30, doi:10.1016/J.ACA.2013.02.031.
78. Duchesne, T. A.; Brown, J. Q.; Guice, K. B.; Nayak, S. R.; Lvov, Y. M.; McShane, M. J. Nanoassembled fluorescent microshells as biochemical sensors. In *Proceedings of SPIE - The International Society for Optical Engineering*; 2002; Vol. 4624.
79. Stouwdam, J. W.; Van Veggel, F. C. J. M. Near-infrared Emission of Redispersible Er3+, Nd3+, and Ho3+ Doped LaF3 Nanoparticles. *Nano Letters* **2002**, *2*, doi:10.1021/nl025562q.
80. Kömpe, K.; Borchert, H.; Storz, J.; Lobo, A.; Adam, S.; Möller, T.; Haase, M. Green-Emitting CePO4:Tb/LaPO4 Core-Shell Nanoparticles with 70 % Photoluminescence Quantum Yield. *Angewandte Chemie - International Edition* **2003**, *42*, doi:10.1002/anie.200351943.

81. Xiang, Y.; Xu, X.-Y.; He, D.-F.; Li, M.; Liang, L.-B.; Yu, X.-F. Fabrication of rare-earth/quantum-dot nanocomposites for color-tunable sensing applications. *Journal of Nanoparticle Research* **2011**, *13*, doi:10.1007/s11051-010-0042-z.
82. Pujari, R. A.; Shitole, P. S.; Charnani, V. S.; McShane, M. J.; Robinson, C. J. Wide-field extrinsic optical signal imaging of fluorescence potassium sensors. In *2006 3rd IEEE International Symposium on Biomedical Imaging: From Nano to Macro - Proceedings*; 2006; Vol. 2006.
83. Brown, J. Q.; Guice, K. B.; McShane, M. J. Internally-Referenced Chemical Transducers Using Molecular Probes Assembled on Fluorescent Nanoparticles. In *Proceedings of IEEE Sensors*; 2003; Vol. 2.
84. Brown, J. Q.; McShane, M. J. Core-referenced ratiometric fluorescent potassium ion sensors using self-assembled ultrathin films on europium nanoparticles. *IEEE Sensors Journal* **2005**, *5*, doi:10.1109/JSEN.2005.859252.
85. Kazakova, L. I.; Shabarchina, L. I.; Anastasova, S.; Pavlov, A. M.; Vadgama, P.; Skirtach, A. G.; Sukhorukov, G. B. Chemosensors and biosensors based on polyelectrolyte microcapsules containing fluorescent dyes and enzymes. *Analytical and Bioanalytical Chemistry* **2013**, *405*, doi:10.1007/s00216-012-6381-0.
86. Guice, K. B.; Caldorera, M. E.; McShane, M. J. Nanoscale internally referenced oxygen sensors produced from self-assembled nanofilms on fluorescent nanoparticles. *Journal of Biomedical Optics* **2005**, *10*, doi:10.1117/1.2147419.
87. Pickup, J. C.; Zhi, Z.-L.; Khan, F.; Saxl, T. E. Nanomedicine in diabetes management: Where we are now and where next. *Expert Review of Endocrinology and Metabolism* **2010**, *5*, doi:10.1586/eem.10.63.
88. Chinnayelka, S.; McShane, M. J. Competitive binding assays in microcapsules as "smart tattoo" biosensors. In *Proceedings of IEEE Sensors*; 2005; Vol. 2005.
89. Zamarreño, C. R.; Bravo, J.; Goicoechea, J.; Matias, I. R.; Arregui, F. J. Response time enhancement of pH sensing films by means of hydrophilic nanostructured coatings. *Sensors and Actuators, B: Chemical* **2007**, *128*, doi:10.1016/j.snb.2007.05.046.
90. Chang-Yen, D. A.; Gale, B. K. An Integrated Optical Glucose Sensor Fabricated Using PDMS Waveguides on a PDMS Substrate. In *Proceedings of SPIE - The International Society for Optical Engineering*; 2004; Vol. 5345.
91. Chu, C.-S.; Chu, S.-W. Optical oxygen sensor based on time-resolved fluorescence. In *Proceedings of SPIE - The International Society for Optical Engineering*; 2015; Vol. 9655.
92. Chan, W. H.; Yang, R. H.; Wang, K. M. Development of a mercury ion-selective optical sensor based on fluorescence quenching of 5,10,15,20-tetraphenylporphyrin. *Analytica Chimica Acta* **2001**, *444*, 261–269, doi:10.1016/S0003-2670(01)01106-0.
93. Lee, D.; Jung, J.; Bilby, D.; Kwon, M. S.; Yun, J.; Kim, J. A novel optical ozone sensor based on purely organic phosphor. *ACS Applied Materials and Interfaces* **2015**, *7*, doi:10.1021/am5087165.
94. Yusoff, N. H.; Salleh, M. M.; Yahaya, M. *Enhanced the performance of fluorescence gas sensor of porphyrin dye by using TiO<inf>2</inf> nanoparticles*; 2008; Vol. 55–57; ISBN 9780878493562.

95. Ali, R.; Lang, T.; Saleh, S. M.; Meier, R. J.; Wolfbeis, O. S. Optical sensing scheme for carbon dioxide using a solvatochromic probe. *Analytical Chemistry* **2011**, *83*, doi:10.1021/ac200298j.
96. Safavi, A; Bagheri, M. Novel optical pH sensor for high and low pH values. *Sensors and Actuators B: Chemical* **2003**, *90*, 143–150, doi:10.1016/S0925-4005(03)00039-X.
97. Wencel, D.; MacCraith, B. D.; McDonagh, C. High performance optical ratiometric sol–gel-based pH sensor. *Sensors and Actuators B: Chemical* **2009**, *139*, 208–213, doi:10.1016/J.SNB.2008.12.066.
98. Lee, S.-H., Kumar, J., Tripathy, S. K. Fluorescence quenching based thin film sensors employing electrostatic layer-by-layer self-assembly. In *Materials Research Society Symposium - Proceedings*; 2011; pp. 891–896.
99. Lee, S. H.; Kumar, J.; Tripathy, S. K. Thin film optical sensors employing polyelectrolyte assembly. *Langmuir* **2000**, *16*, 10482–10489, doi:10.1021/la0011836.
100. Caselli, M. Porphyrin-based electrostatically self-assembled multilayers as fluorescent probes for mercury(ii) ions: A study of the adsorption kinetics of metal ions on ultrathin films for sensing applications. *RSC Advances* **2015**, *5*, doi:10.1039/c4ra09814e.
101. Qin, C.; Cheng, Y.; Wang, L.; Jing, X.; Wang, F. Phosphonate-Functionalized Polyfluorene as a Highly Water-Soluble Iron(III) Chemosensor. *Macromolecules* **2008**, *41*, 7798–7804, doi:10.1021/ma801282m.
102. Yanan Li, Hui Huang, Yan Li, X. S. Highly sensitive fluorescent sensor for mercury (II) ion based on layer-by-layer self-assembled films fabricated with water-soluble fluorescent conjugated polymer. *Sensors and Actuators B: Chemical* **2013**, *188*, 772–777, doi:10.1016/J.SNB.2013.07.093.
103. Chao Wang, Jianwu Zhao, Yan Wang, Nan Lou, Qiang Ma, X. S. Sensitive Hg (II) ion detection by fluorescent multilayer films fabricated with quantum dots. *Sensors and Actuators B: Chemical* **2009**, *139*, 476–482, doi:10.1016/J.SNB.2009.03.012.
104. Qiang Ma, Enna Ha, Fengping Yang, X. S. Synchronous determination of mercury (II) and copper (II) based on quantum dots-multilayer film. *Analytica Chimica Acta* **2011**, *701*, 60–65, doi:10.1016/J.ACA.2011.04.051.
105. Yang F, Ma Q, Yu W, S. X. Naked-eye colorimetric analysis of Hg2+ with bi-color CdTe quantum dots multilayer films. *Talanta* **2011**, *84*, 411–415, doi:10.1016/J.TALANTA.2011.01.054.
106. Gonçalves HM, Duarte AJ, Davis F, Higson SP, E. da S. J. Layer-by-layer immobilization of carbon dots fluorescent nanomaterials on single optical fiber. *Analytica Chimica Acta* **2012**, *735*, 90–95, doi:10.1016/J.ACA.2012.05.015.
107. Chan, Y.-H.; Chen, J.; Liu, Q.; Wark, S. E.; Son, D. H.; Batteas, J. D. Ultrasensitive Copper(II) Detection Using Plasmon-Enhanced and Photo-Brightened Luminescence of CdSe Quantum Dots. *Analytical Chemistry* **2010**, *82*, 3671–3678, doi:10.1021/ac902985p.
108. Chan, Y.-H.; Chen, J.; Wark, S. E.; Skiles, S. L.; Son, D. H.; Batteas, J. D. Using patterned arrays of metal nanoparticles to probe plasmon enhanced luminescence of CdSe quantum dots. *ACS Nano* **2009**, *3*, doi:10.1021/nn900317n.

109. Kramarenko, G. G.; Hummel, S. G.; Martin, S. M.; Buettner, G. R. Ascorbate reacts with singlet oxygen to produce hydrogen peroxide. *Photochemistry and Photobiology* **2006**, *82*, doi:10.1562/2006-01-12-RN-774.
110. Ahmed, S. R.; Koh, K.; Kang, N. L.; Lee, J. Highly Sensitive Fluorescent Probes for the Quantitative Determination of Singlet Oxygen (1O 2). *Bulletin of the Korean Chemical Society* **2012**, *33*, doi:10.5012/bkcs.2012.33.5.1608.
111. Grant, P. S.; Kaul, S.; Chinnayelka, S.; McShane, M. J. Fiber Optic Biosensors Comprising Nanocomposite Multilayered Polymer and Nanoparticle Ultrathin Films. In *Annual International Conference of the IEEE Engineering in Medicine and Biology - Proceedings*; 2003; Vol. 4.
112. Grant, P.; Barnidge, M.; McShane, M. Spectroscopic Fiber Probes for Chemical Sensing Based on LbL Self Assembled Ultra-Thin Films. In *Proceedings of IEEE Sensors*; 2003; Vol. 2, pp. 895–898.
113. Chang-Yen, D. A.; Lvov, Y.; McShane, M. J.; Gale, B. K. Electrostatic self-assembly of a ruthenium-based oxygen sensitive dye using polyion–dye interpolyelectrolyte formation. *Sensors and Actuators B: Chemical* **2002**, *87*, 336–345, doi:10.1016/S0925-4005(02)00267-8.
114. Grant, P. S.; McShane, M. J. Development of multilayer fluorescent thin film chemical sensors using electrostatic self-assembly. *IEEE Sensors Journal* **2003**, *3*, doi:10.1109/JSEN.2002.807484.
115. Tung, T. T.; Nine, M. J.; Krebsz, M.; Pasinszki, T.; Coghlan, C. J.; Tran, D. N. H.; Losic, D. Recent Advances in Sensing Applications of Graphene Assemblies and Their Composites. *Advanced Functional Materials* **2017**, doi:10.1002/adfm.201702891.
116. Jung, Y. K.; Lee, T.; Shin, E.; Kim, B.-S. Highly tunable aptasensing microarrays with graphene oxide multilayers. *Scientific Reports* **2013**, *3*, doi:10.1038/srep03367.
117. Chang, H.; Tang, L.; Wang, Y.; Jiang, J.; Li, J. Graphene fluorescence resonance energy transfer aptasensor for the thrombin detection. *Analytical Chemistry* **2010**, *82*, doi:10.1021/ac9025384.
118. Ban, S.; Hosoki, A.; Nishiyama, M.; Seki, A.; Watanabe, K. Optical fiber oxygen sensor using layer-by-layer stacked porous composite membranes. In *Proceedings of SPIE - The International Society for Optical Engineering*; 2016; Vol. 9754.

Chapter 3

Layer-by-Layer assembly of a water-insoluble platinum porphyrin for oxygen monitoring

In this chapter, a luminescence-based optical fiber oxygen sensor has been built up by means of the LbL nanoassembly technique. The main drawback of the sensitive porphyrin, Pt-TFPP, for its deposition by LbL is its water-insolubility. In order to overcome this, it is suggested in this work to entrap the porphyrins into anionic micelles. The LbL assembly of this material has been checked out by Energy-Dispersive X-ray spectroscopy and by analyzing the absorption spectrum of the obtained microstructure. Finally, its performance as an oxygen sensor has also been tested.[1]

[1] This Chapter has been partially published in the paper entitled *Layer-by-Layer assembly of a water-insoluble platinum complex for optical oxygen sensors* in the journal Sensors and Actuators: B.

3.1. Introduction

Oxygen monitoring is of great importance in many different research fields, such as medicine [1], biotechnology [2], environmental science [3], agriculture [4] or food packaging industry [5]. Hence, many efforts have been devoted to the development of accurate oxygen sensors. The Clark electrode [6] was one the earliest devices reported for oxygen monitoring, which consisted of the detection of a current flow caused by the reduction of oxygen. Although many electronic devices have been fabricated since then [7-8], they exhibit many drawbacks and limitations [8].

In the last years, optical devices and, in particular, optical fiber sensors, have appeared as an alternative [9] to the electronic ones, owing to the interesting features that optical fiber offers: for instance, due to its dieletric nature it is immune towards electromagnetic fields [10] and it permits to multiplex several sensing devices over long distances in a single fiber [11]. Furthermore, optical fiber sensors do not consume oxygen during the sensing process [12], and they have shown high accuracy [13] and good sensitivity and reversibility [14]. Among the different optical techniques for oxygen detection [15-16], luminescence quenching is the most widespread one [17]: in the presence of oxygen, the luminescent intensity of an indicator decreases reversely [18].

Ruthenium-based porphyrins and palladium- or platinum-metalloporphyrins are the most utilized oxygen indicators. The latter ones owe their high affinity towards oxygen to their chemical structure. In nature there are numerous examples of metalloporphyrins, in fact, we ourselves carry out metalloporphyrins in our bodies since hemoglobin, the responsible of oxygen transport in blood, is formed by proteins that contain iron porphyrins .Furthermore, they are well-known due to their strong phosphorescence at room temperature, large Stokes' shift and good absorption coefficients [19]. In consequence, they have become the most popular indicators for the fabrication of luminescent oxygen sensors operating in physiologically relevant concentrations. Oppositely, their water-insolubility [20] limits the variety of techniques that can be employed for the fabrication of sensors.

These indicators are usually entrapped in polymeric [21][22] or sol-gel [23] matrices for their deposition onto planar substrates, such as quartz or glass slides, or optical fiber. As a good sensitivity is a key requirement for oxygen sensors [24], these matrices must be highly permeable in order to allow a rapid adsorption/desorption of the gas. Besides, to achieve highly photostable sensors, it is desirable to control the distribution of the luminophore inside the matrix, so its aggregation and the self-quenching effect are avoided. These conditions (good sensitivity and high photostability) can be obtained by fabricating the sensors by means of the Layer-by-Layer nano-assembly technique, which briefly consists of the adsorption of oppositely charged materials (usually polyelevtrolytes) by electrostatic forces or other attractive forces, for instance, hydrophobic interactions [25]. An accurate selection of the materials and the deposition parameters permits to tailor the layer thickness in the nanometer scale [26], as well as to modify the permeability of the coating [27], promoting the adsorption of the target analyte and forming a barrier against undesired molecules. Thus, many different luminescence-based sensors have been built by this technique. However, as it has been explained in the previous chapter, only water-soluble indicators have been utilized so far for the fabrication of luminescent sensors by means of the LbL technique.

Taking advantage of the above mentioned features of the metalloporphyrins, as well as of the versatility of the LbL technique would permit the development of highly sensitive and stable oxygen sensors. Thus, achieving the layer-by-layer assembly of water-insoluble porphyrins comes across as a challenging opportunity, being the main objective of this chapter.

3.2. Theoretical considerations

Photoluminescence is the emission of energy in the form of light in the visible or near-visible spectrum from any substance [28]. That energy has been previously absorbed, promoting the transition of electrons from the ground state to the electronically excited states. When these electrons return to the ground state emission occurs, as it is illustrated in the Jablonski diagram shown in Figure 3.1.

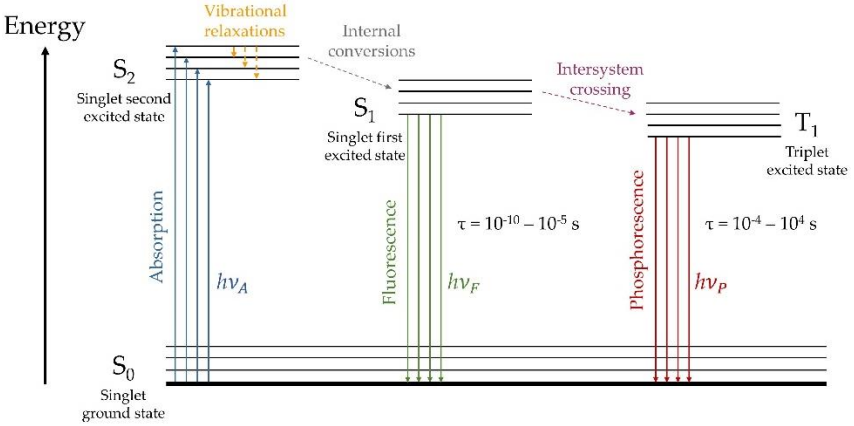

Figure 3.1. Jablonski diagram, where the main electronic states and transitions between them are illustrated.

The energy difference between the ground and the excited states determines the wavelength at which each phenomenon takes place, according to the Planck-Einstein relation:

$$E = h\upsilon_X = h\frac{c}{\lambda_X} \qquad \text{(eq. 3.1)}$$

where h corresponds to the Planck constant, ν is the frequency of light, c is the speed of light in vacuum and λx is the wavelength of the absorbed (X = A) or emitted light (X = F corresponds the fluorescence, whereas X = P means phosphorescence).

Due to the large energy difference between the ground (S_0) and the excited states (S_1, S_2 and T_1), electrons transition from the former state to the latter ones cannot be accomplished by thermal processes, but it must be induced by the absorption of light. Once absorption occurs and electrons populate the excited states S_2 and S_1, they promptly relax to the lowest vibrational level of S_1, and usually return to the ground state emitting photons. This process is termed fluorescence. In some other occasions, intersystem crossing takes place and electrons from S_1 move towards triplet excited state, T_1, and then they decay to the ground state (transition from T_1 to S_1 is forbidden), giving rise to the phenomenom known as phosphorescence.

The time needed by an excited electron to return from an excited state to the ground one is known as lifetime. As transitions from the singlet states to the ground state are faster than those from the triplet state, fluorescence lifetimes are shorter than the phosphorescence ones. As the lifetime determines the time that the luminophore is available to interact with the environment, it is a key parameter for the design of luminescence-based sensors.

Furthermore, the energy difference between the first singlet excited state and the ground state is larger than the energy difference between the triplet excited state and the ground one, what implies that those wavelengths at which fluorescence takes place are shorter than those at which phosphorescence occurs.

Although many transitions between the different states of energy are possible, only fluorescence and phosphorescence are radiative. Among the non-radiative relaxations, the following ones affect most the behavior of luminescence-based sensors:

- Photobleaching: the long-term exposure to high-intensity illumination can cause a photochemical modification of the luminophore, preventing the transition of electrons from the ground state to the excited states and backwards and, thus, avoiding the emission of photons.

- Quenching: consists of the relaxation of electrons to the ground state without emitting photons. It can be caused by the presence of a molecule (quencher) of by high concentrations of the luminophore, which promote the luminescent particles to collide each other, with the concomitant quenching. In this case, the phenomenon is termed self-quenching.

The luminescence quenching caused by some molecules (quenchers) can be utilized to monitor their concentration. Thus, most of the luminescent sensors are based on this principle, which can be mathematically modelled by the Stern-Volmer equation:

$$\frac{I_0}{I} = 1 + K_{SV}[Q] \qquad \text{(eq. 3.2)}$$

where I_0 represents the intensity in the absence of the quencher, I is the emitted intensity at a certain concentration, K_{SV} is the quenching constant and $[Q]$ is the quencher concentration expressed in %. This mathematical model supposes that the luminophore is uniformly distributed into the entrapping matrix and, in consequence, all the sensing molecules are equally quenched [29]. However, this does not always occur, and when the luminescent particles are heterogeneously distributed into the embedding matrix, not all them are equally affected by the quencher. This situation can be mathematically described by the two-sites model proposed by Carraway et al. [30]:

$$\frac{I_0}{I} = \left(\frac{f_1}{1+K_{SV,1}[Q]} + \frac{f_2}{1+K_{SV,2}[Q]}\right)^{-1} \qquad \text{(eq. 3.3)}$$

where f_1 and f_2 ($f_2 = 1 - f_1$) are the different populations of the luminophore, and $K_{SV,1}$ and $K_{SV,2}$ their respective quenching constants.

3.3. Experimental considerations

3.3.1. Pt-TFPP as a luminescent indicator of oxygen

To the category of metalloporphyrins belongs the indicator chosen for this work, platinum tetrakis(pentafluorophenyl)porphyrin (Pt-TFPP), whose chemical structure is shown in Figure 3.2. The reasons of selecting this specific indicator are explained below.

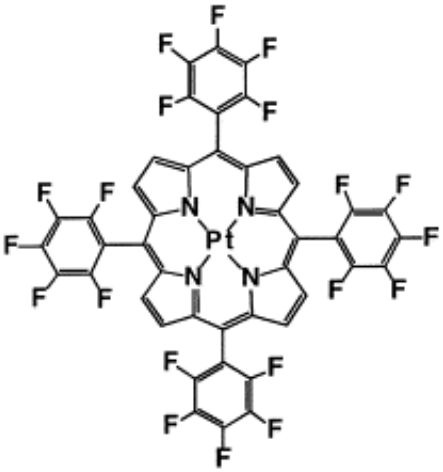

Figure 3.2. Chemical structure of Pt-TFPP.

Its absorption spectrum exhibits a Soret band (maximum absorption) centered at 392 nm, and secondary absorption peaks located at 507 and 542 nm. When illuminated at those wavelengths, Pt-TFPP shows a luminescence peak at 650 nm, whose intensity depends inversely on the oxygen concentration. Both absorption and emission spectra are displayed in Figure 3.3. This material presents a long decay time (about 60 μs) and an acceptable brightness, as well as good chemical stability and low photodegradation [31]. As it is a highly fluorinated compound, this metalloporphyrin also exhibits high photostability, a crucial

parameter when prolonged measurements are carried out. Furthermore, it shows a much lower degree of thermal quenching than other compounds, for instance, Eu(III) complexes. These features, along with its commercial availability, make Pt-TFPP an adequate indicator for gaseous oxygen.

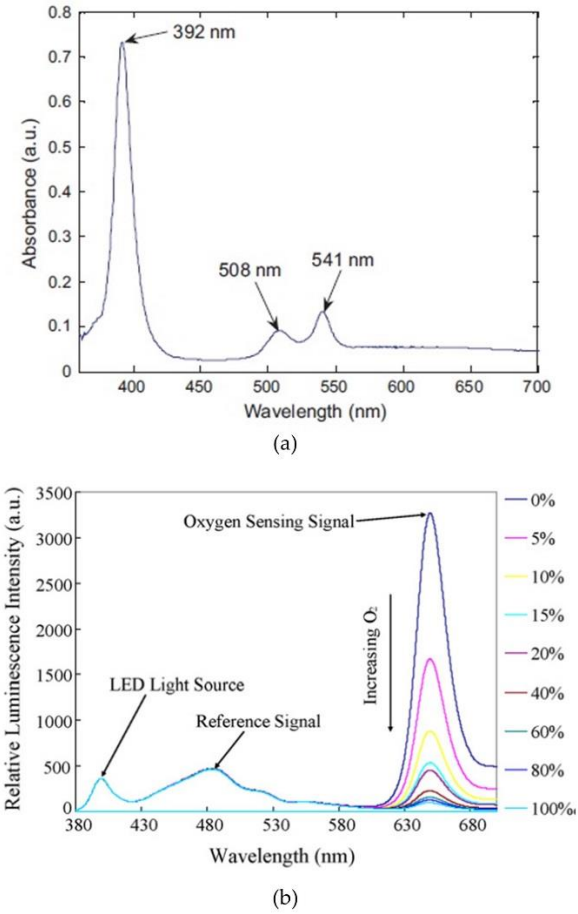

Figure 3.3. (a) Absorption and (b) emission spectra of Pt-TFPP in the presence of different oxygen concentrations. Reprinted from [23].

3.3.2. Optical set-up

The optical set-up employed consisted of a reflection architecture, which provided a good robustness to the sensing system. Thus, the luminophore was deposited on the unclad tip of the optical fiber. This, and other approaches for placing the dye on the tip of the fiber are shown in Figure 3.4.

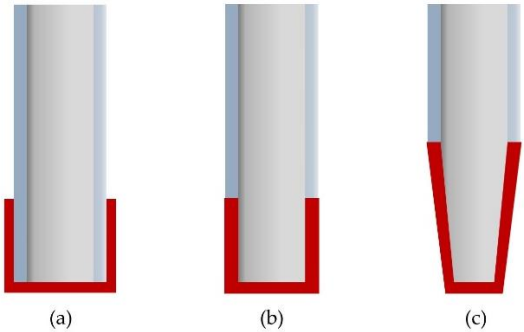

Figure 3.4. Configuration schemes for optical fiber sensors based on luminescence: (a) intrinsic configuration onto the clad tip of the fiber, (b) intrinsic configuration onto the unclad tip of the fiber, (c) taper configuration.

The sensor was fabricated onto the tip of an unclad optical fiber of 400 μm-core, which was connected to the common branch of a 200 μm-core UV-VIS bifurcated fiber. Each one of the independent branches of the bifurcated fiber was connected to the light source, a LED centered at 390 nm, and to the spectrometer USB2000FLG.

3.3.3. Experimental set-up

The characterization of the sensor was carried out into a dark and hermetic chamber in order to avoid any external contamination, from gases and/or light. There, it was exposed to a constant gaseous nitrogen flow of 250 mL/min. The gas flow concentration was accurately adjusted by a LabView® virtual software which controlled the flow through the EL-Mass Flow Meters (obtained from Bronkhorst) connected to each one of the high purity gas bottles (higher than 99.998% and 99.95% in the cases of nitrogen and oxygen, respectively). The complete experimental set-up utilized for the characterization of the sensors is displayed in Figure 3.5.

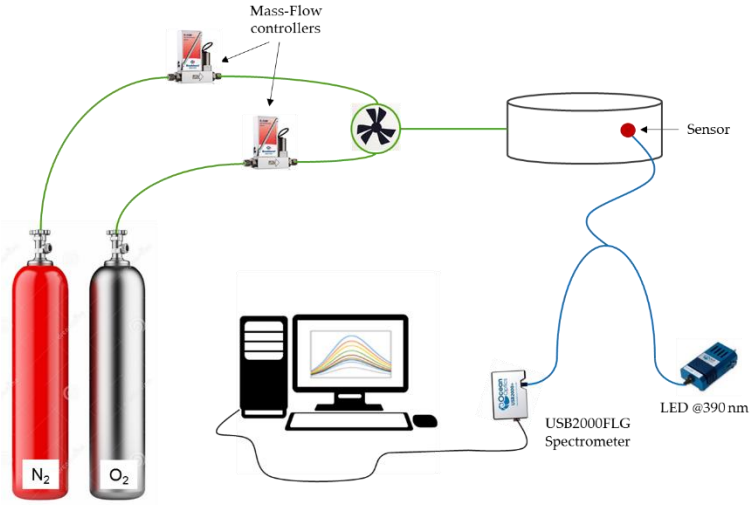

Figure 3.5. Experimental set-up employed for sensors characterization: the green-colored lines correspond to gas tubes, the blue-colored represent the bifurcated optical fiber, and the grey one is the electrical connection between the spectrometer and the computer.

Furthermore, when working with luminescence-based sensors, signal changes caused by fluctuations of the light source must be avoided, thus, the intensity of the luminescent peak was always relativized to the intensity of the light source.

3.4. Layer-by-Layer assembly of water-insoluble porphyrins

High permeability is a fundamental feature of oxygen sensors [32], thus, polymeric [33][34] and sol-gel [35] matrices have been typically employed for their fabrication. However, these coatings exhibit non-negligible drawbacks: the distribution of the luminophore inside them cannot be controlled [36], and the deposition mechanisms utilized are not highly reproducible [37], which can be overcome by employing the LbL technique. This procedure requires the materials to be dissolved in water, and to show opposite surface charges in order to get assembled. In the case of Pt-TFPP, it does not exhibit any superficial charge and it is water-insoluble. Thus, it can be neither assembled with an oppositely charged polyelectrolyte, nor added to a polyelectrolyte solution in order to be deposited.

3.4.1. Incorporation of Pt-TFPP into zirconium phosphate films fabricated by LbL adsorption and reaction method

A procedure for the incorporation of water-insoluble porphyrins in LbL films was described by Wang et al. [38]: it consisted of dissolving the oxygen-sensitive porphyrin Rudpp in a mixture of an aqueous phosphate solution and ethanol (4:1 v/v). The use of this solvent permitted two different facts: on one side, it made possible the presence of the water-insoluble Rudpp in the phosphate solution and it was evaporated once the films were built, without any influence on the properties of the as-built films. On the other side, it provided a hydrophobic environment, which facilitated the adsorption of Rudpp into the film. The final films were obtained by utilizing these materials as the anionic ones, and zirconium sulfate as cationic counterpart. Furthermore, they exhibited a porous structure, which facilitated the permeation of oxygen into inside them.

Owing to the proper features of these films for the fabrication of hydrophobic and permeable coatings, which are desirable characteristics

of oxygen sensors, they were tried to be reproduced onto glass slides with the only difference of the oxygen-sensitive material: Rudpp was replaced by Pt-TFPP. However, although low concentrations of Pt-TFPP (1mg/ml) were used, its precipitation was not avoided. Furthermore, when exposing the as-coated glass slides to UV illumination, no luminescence was observed, demonstrating that Pt-TFPP had not been properly assembled.

3.4.2. Incorporation of Pt-TFPP into LbL films by using micelles

Another possibility consists of using micelles [39], i.e., aggregates of amphiphilic molecules having a polar head and a non-polar tail. When micelles are formed, the polar heads of the molecules are pointing out to the surrounding media, forming an outer shell, and the non-polar tails remain in the interior. This shell can be used to entrap water-insoluble molecules in its interior, avoiding their further aggregation and precipitation, as it is shown in Figure 3.6.

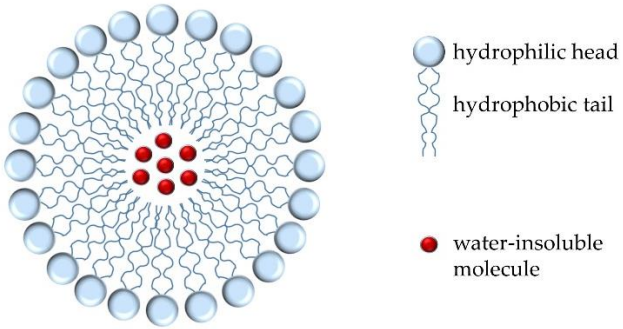

Figure 3.6. Schematic representation of a micelles entrapping a water-insoluble dye.

For the entrapment of the water-insoluble luminophore inside the micelles, it is first dissolved in an organic solvent less polar than water,

for instance, acetone, and a surfactant is dissolved in water. Then, the two solutions are mixed, forming an emulsion that contains the luminophore entrapped inside the surfactant micelles. In this manner, the sensing material is present in a water solution after solvent evaporation and, what is more, it can be deposited by means of the LbL technique owing to the superficial charge of the polar heads of the surfactant that are pointing out. In this case, the anionic surfactant Sodium Dodecyl Sulfate (SDS) was chosen as the anionic counterpart.

The cationic material employed was poly(allylamine hydrochloride) (PAH, M_w ~58000 g mol^{-1}), a weak polyelectrolyte which has been widely used for the fabrication of sensing films by means of the LbL technique [40]. It gives rise to hydro-gel structures and, at high pH it is barely ionized, forming thick layers (around 5 nm at pH 9) [41]. Its concentration was 10 mM.

Firstly, the nanostructure $[PAH/Pt\text{-}TFPP_{SDS}]_{10}$ was deposited onto a glass slide, and it was analyzed by means of the EDX technology. As it is displayed in Figure 3.7, Platinum and Fluor were present in the deposited layer, what implied that the Pt-TFPP had been assembled. Furthermore, Sulfur was also detected, what meant that micelles had been formed, and the presence of Oxygen corresponded to PAH, the only one material that possess that molecule. Thus, the three chemical compounds that formed the sensing nanostructure had been deposited onto the glass slide.

Another method to probe the deposition of the sensitive material is the analysis of the absorption spectrum of the coating, which was carried out with a Jasco V-630 Spectrophotometer. The absorption spectrum of the $[PAH/Pt\text{-}TFPP_{SDS}]_{10}$ nanostructure, utilizing a 0.8 mg/ml Pt-TFPP concentration, is plotted in Figure 3.8: it showed three absorption peaks, centered at 389, 504 and 544 nm, which correspond to the indicator, demonstrating its presence in the coating.

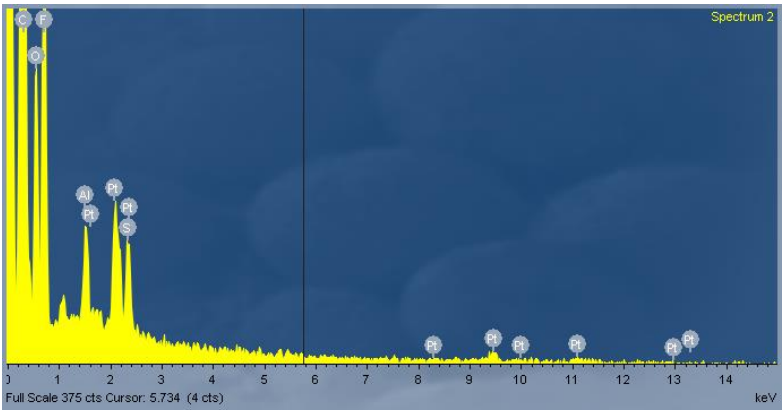

Figure 3.7. EDX analysis of the multilayer nanostructure [PAH/Pt-TFPP$_{SDS}$]$_{10}$ deposited onto a glass slide. Reprinted from [42].

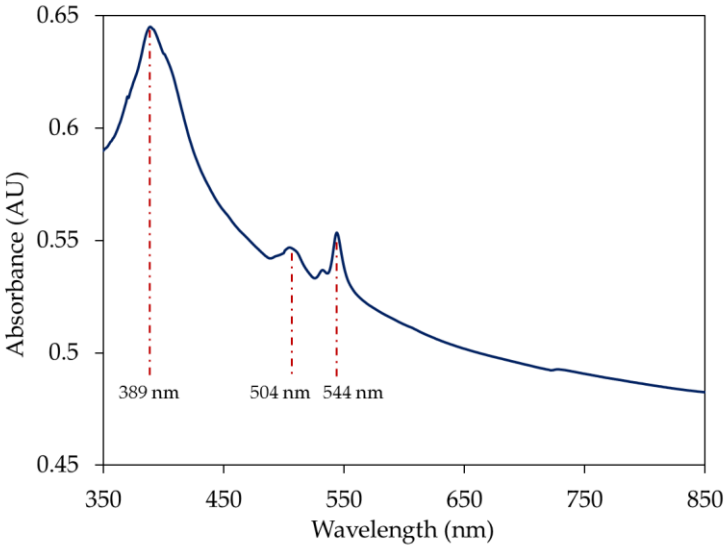

Figure 3.8. Absorption spectra of the [PAH/Pt-TFPP$_{SDS}$]$_{10}$ coating.

Once it was demonstrated that it was possible to assembly Pt-TFPP inside a LbL-built nanostructure by utilizing micelles, the same

deposition was carried out onto the tip of an optical fiber. Thus, by analyzing a Scanning Electron Microscope (SEM) image of the coating, which is shown in Figure 3.9, its suitability for oxygen sensing purposes was checked out.

As it can be observed, it exhibited a noticeable roughness, as well as a good porosity, which are desirable features of oxygen sensing coatings.

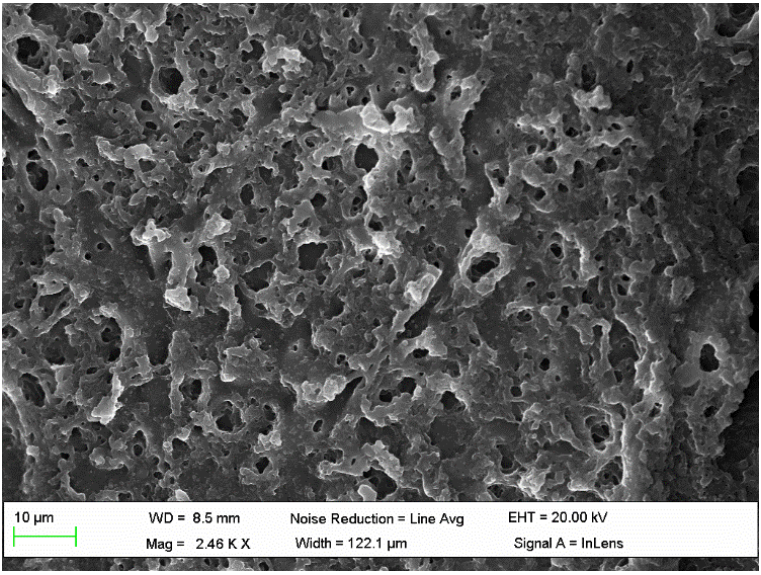

Figure 3.9. Scanning Electron Microscope (SEM) image from a [PAH/Pt-TFPP$_{SDS}$]$_{10}$ film. Reprinted from [42].

3.4.3. Sensor characterization

For analyzing the performance of the [PAH/Pt-TFPP$_{SDS}$]$_{10}$ nanostructure as oxygen sensor, it was deposited onto the tip of a 400 µm-core optical fiber, which was connected to a 200 µm-core bifurcated fiber.

First of all, the Pt-TFPP concentration of the sensing films was optimized: utilizing the experimental set-up shown in Figure 3.5, the relative intensities (I_{650}/I_{410}) emitted at room conditions (21% O_2, 22 ºC and 35% RH) by several sensors fabricated with different Pt-TFPP concentrations in the range between 0.01 and 1 mg/ml were compared. The sensors built up using Pt-TFPP concentrations of 0.04 and 0.8 mg/ml exhibited the highest relative intensities, so they were exposed to the continuous illumination of a LED centered at 390 nm for 90 min. In this manner, the photobleaching effect on the two sensors was analyzed: whereas the intensity of the sensor fabricated by utilizing 0.8 mg/ml of Pt-TFPP decreased a 7% of the total after 90 minutes, the intensity corresponding to the sensor of 0.04 mg/ml of Pt-TFPP increased a 2%, as it is displayed in Figure 3.10. Thus, this concentration was chosen as the optimal one for the development of the oxygen sensor.

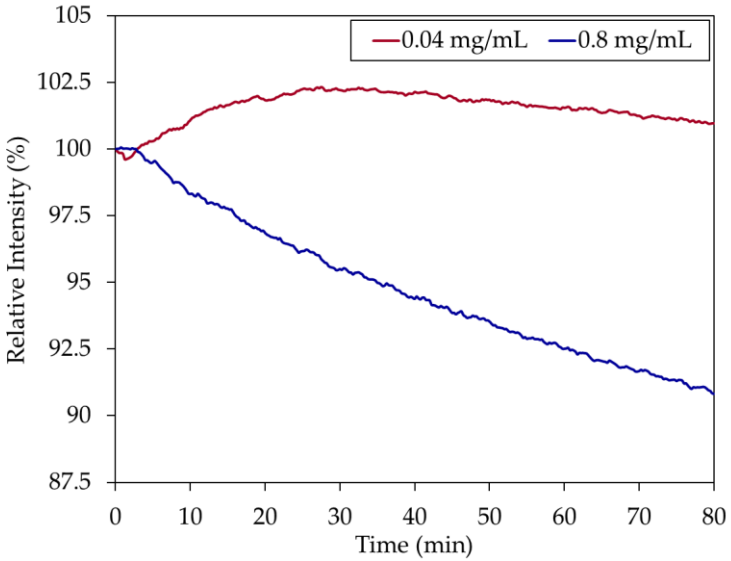

Figure 3.10. Photobleaching of the two sensors fabricated with the $(PAH/Pt\text{-}TFPP_{SDS})_{10}$ structure but different Pt-TFPP concentrations: 0.04 mg/ml (red line) and 0.8 mg/ml (blue line).

In order to establish a relationship between the oxygen concentration and the relative intensity of the luminescence peak (I_{650}/I_{410}), the sensor was exposed to concentrations of that gas from 0% to 100% in steps of 5%. In Figure 3.11 the relative luminescence intensities for different oxygen concentrations in steps of 10% are plotted. As it was expected, the presence of oxygen quenched the luminescent intensity of the sensor: the maximum of the intensity corresponded to the 0% of oxygen concentration, and the minimum was reached for 100% of oxygen.

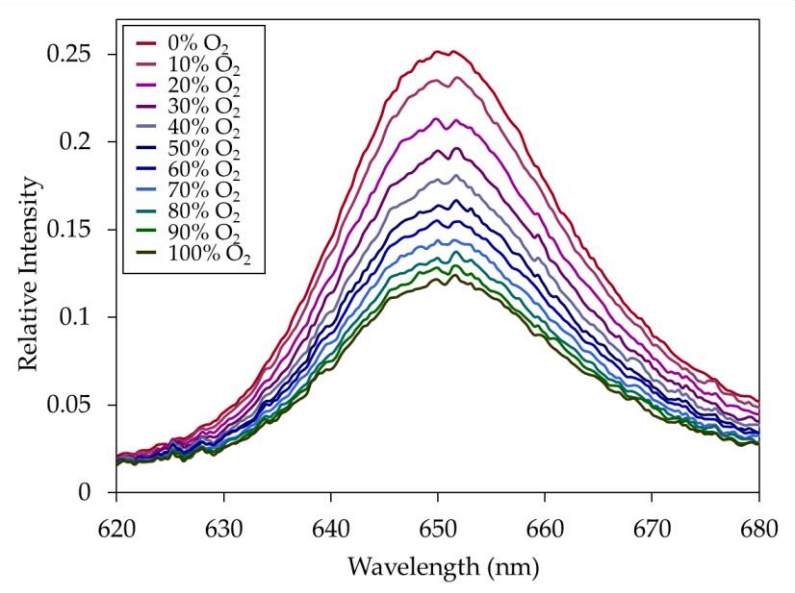

Figure 3.11. Relative luminescence intensity of the $[PAH/Pt\text{-}TFPP_{SDS}]_{10}$ sensor when it is exposed to different oxygen concentrations.

As explained in section 3.2, optical sensors based on the luminescence quenching principle are calibrated according to the Stern-Volmer equation. This equation requires the luminescent intensities measured for every oxygen concentration to be relativized to that obtained in its absence, in order to obtain the quenching constant of the sensor (K_{SV}). The resultant calibration curve is displayed in Figure 3.12: it showed a linear

tendency (R^2 = 0.9991) with a quenching constant of 0.0113, and demonstrated the capability of the sensor to clearly distinguish every change of 5% of the oxygen concentration.

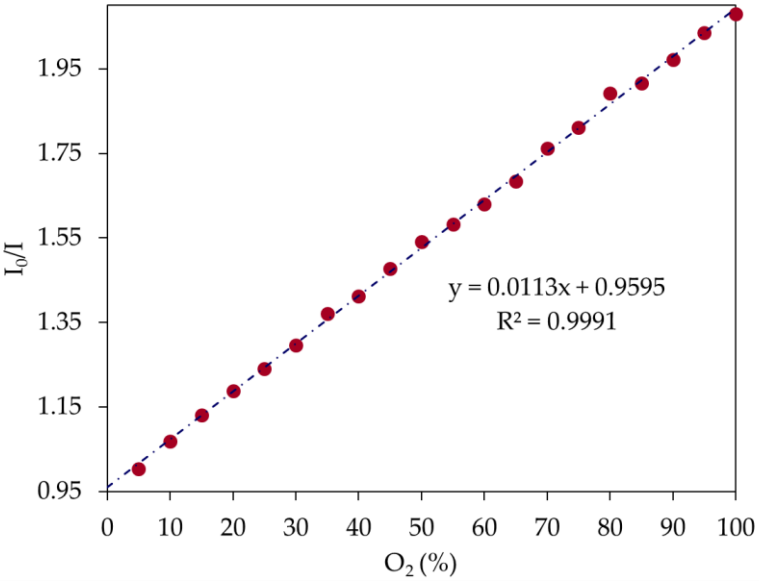

Figure 3.12. Stern-Volmer curve of the sensor.

Other important characteristics of these oxygen sensors are their reproducible behaviour towards incremental and decremental changes of oxygen concentration, their capability for recovering the baseline (intensity in the absence of oxygen) and their temporal stability. These three features are shown in Figure 3.13, where the dynamic response of the sensor was studied in two different stages spaced 24 hours. The first cycle consisted of oxygen concentrations of 0% - 20% - 0% - 15% - 0% - 10% - 0%, whereas in the second one, the concentrations were changed in the opposite way. Analyzing the graph, it can be concluded that the sensor satisfied the three requirements: first, the relative intensity for each concentration was the same in both cycles, second, the baseline was

recovered after every change of the oxygen concentration and, finally, the sensor exhibited the same behavior after a pause of 24 hours.

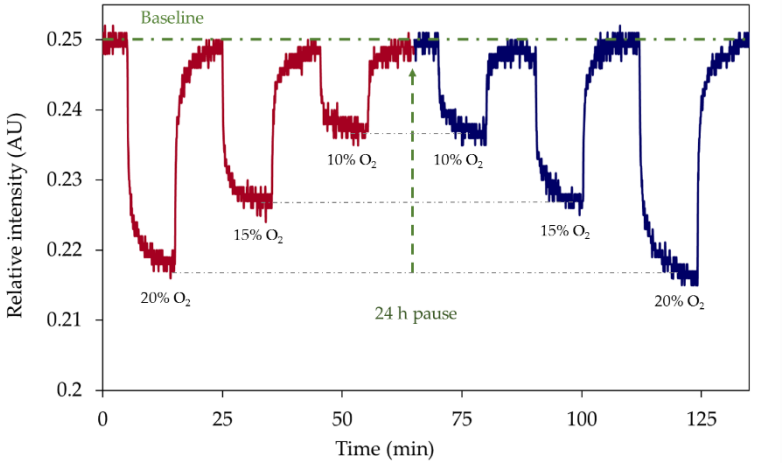

Figure 3.13. Dynamic response of the sensor when it is exposed to dynamic variations of the oxygen concentration in opposite directions and at different moments.

Finally, the kinetics of the sensor were analysed by exposing it towards changes in the oxygen concentration from 0% to 100% and vice-versa, as shown in Figure 3.14. The response time of a sensor is defined as the time needed by the intensity to change from 10% to 90% of the total intensity when switching from 100% N_2 to 100% O_2 atmospheres, and the recovery time is calculated as the time it took the intensity to vary from 90% to 10% of the total variation range, when changing from a completely oxygenated environment, to a totally de-oxygenated one. The response time of the sensor was 5.9 minutes, whereas the recovery time was 9.1 minutes.

The long response and recovery times, as well as the low sensitivity of the sensor, could be explained by different reasons: for instance, the diameters of the fiber cores (400 μm for the sensor and 200 μm for the bifurcated fiber) were not the most appropriate for analyzing

luminescence-based sensors, as it will be demonstrated in the following chapter. Thus, it is probable that not all the luminescent intensity emitted by the sensor was coupled to the spectrometer. In addition, due to its fragility, it was not possible to polish the tip of the 400 μm-core fiber properly, so it could not be ensured that the sensor was built onto a flat surface: this fact probably affected to the uniformity of the nanostructure. Furthermore, the polymeric matrix that embeds the fluorophore and the parameters of the LbL deposition (pH) have still to be optimized.

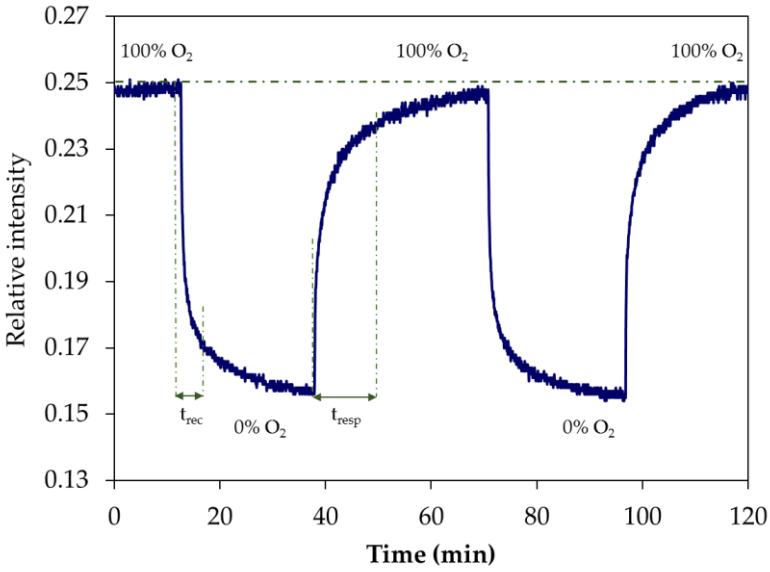

Figure 3.14. Dynamic response of the sensor under exposition towards changes in the oxygen concentration from 0% to 100%. Response and recovery times of the sensor are highlighted.

3.5. Conclusions

Despite its water-insolubility, the oxygen indicator Pt-TFPP has been deposited by means of the LbL technique thanks to its entrapment in anionic micelles of SDS. This approach opens the door to the deposition of other metalloporphyrins by LbL. When combining the anionic micelles of SDS, which entrap Pt-TFPP, with the cationic polyelectrolyte PAH, the sensing structure is rough and porous, giving rise to a linear oxygen sensor in the whole range of oxygen concentrations. The LbL assembly of a water-insoluble metalloporphyrin for the first time opens the door to the analysis of the influence of the features of different polymeric matrices on the performance of luminescent sensors.

It is clear the need to optimize the coupling of light from the sensor to the spectrometer which would allow to increase the amount of luminescent light detected and to decrease the background noise, hence enhancing the signal to noise ratio of the sensor. Other aspects to be taken into account would be the influence of the polymeric matrix as well as the parameters of the LbL deposition. All these factors will be studied in the next chapter.

Bibliography

1. Litscher, G.; Jobstmann, R.; Neumann, I.; Prietl, B.; Schwarz, G.; Klein, G. Non-Invasive Monitoring of Regional Cerebral Oxygen. Saturation - Experiences in Intensive Care Medicine | Nichtinvasive Überwachung der regionalen zerebralen Sauerstoffsättigung - Erfahrungen aus der Intensivmedizin. Biomedizinische Technik 1995, 40, doi:10.1515/bmte.1995.40.3.70.
2. Super, A.; Jaccard, N.; Cardoso Marques, M. P.; Macown, R. J.; Griffin, L. D.; Veraitch, F. S.; Szita, N. Real-time monitoring of specific oxygen uptake rates of embryonic stem cells in a microfluidic cell culture device. Biotechnology Journal 2016, 11, doi:10.1002/biot.201500479.
3. Liu, W.-C.; Chen, W.-B. Monitoring sediment oxygen demand for assessment of dissolved oxygen distribution in river. Environmental Monitoring and Assessment 2012, 184, doi:10.1007/s10661-011-2364-4.
4. Meng, X.; Huang, J.; Xie, Q.; Chen, W. Online monitoring equipment for aquaculture based on unmanned automatic cruise boat. Nongye Jixie Xuebao/Transactions of the Chinese Society for Agricultural Machinery 2015, 46, doi:10.6041/j.issn.1000-1298.2015.03.040.
5. Liu, Z.; Yan, C.; Wang, X.; Han, X. Design for real-time monitoring system of high oxygen modified atmosphere box of vegetable and fruit for preservation; 2011; Vol. 344 AICT; ISBN 9783642183324.
6. Qlark, L. C. Monitor and control of blood and tissue oxygen tensions. 1956, 2, 41–48.
7. Park, C. O.; Fergus, J. W.; Miura, N.; Park, J.; Choi, A. Solid-state electrochemical gas sensors. Ionics 2009, 15, doi:10.1007/s11581-008-0300-6.
8. A new type of amperometric oxygen sensor based on a mixed-conducting composite membrane. Sensors and Actuators B: Chemical 2001, 72, 35–40, doi:10.1016/S0925-4005(00)00629-8.
9. Wang, X.; Wolfbeis, O. S. Optical methods for sensing and imaging oxygen: materials, spectroscopies and applications. Chemical Society reviews 2014, 43, 3666–761, doi:10.1039/c4cs00039k.
10. Sabri, N.; Aljunid, S. A.; Salim, M. S.; Fouad, S. Fiber optic sensors: Short review and applications; 2015; Vol. 204;.
11. Hernandez-Lorenzo, R.; Lopez-Amo, M.; Urquhart, P. Single and double distributed optical amplifier fiber bus networks with wavelength division multiplexing for photonic sensors. Journal of Lightwave Technology 1998, 16, 485–489, doi:10.1109/50.664053.
12. Wang, X.; Chen, H.; Zhao, Y.; Chen, X.; Wang, X.; Chen, X. Optical oxygen sensors move towards colorimetric determination. TrAC Trends in Analytical Chemistry 2010, 29, 319–338, doi:10.1016/j.trac.2010.01.004.
13. Applications of a high accuracy optical fiber displacement sensor to vibrometry and profilometry. Sensors and Actuators A: Physical 2004, 116, 85–90, doi:10.1016/J.SNA.2004.03.038.
14. Fiber optic profenofos sensor based on surface plasmon resonance technique and molecular imprinting. Biosensors and Bioelectronics 2016, 79, 150–157,

doi:10.1016/J.BIOS.2015.11.095.
15. Lou, X.; Somesfalean, G.; Chen, B.; Zhang, Z. Oxygen measurement by multimode diode lasers employing gas correlation spectroscopy. 2009, 48, 990–997.
16. Chung, K. E.; Lan, E. H.; Davidson, M. S.; Dunn, B. S.; Valentine, J. S.; Zink, J. I. Measurement of dissolved oxygen in water using glass-encapsulated myoglobin. 1995, 67, 1505–1509.
17. Demas, J. N.; DeGraff, B. A.; Coleman, P. B. Oxygen sensors based on luminescence quenching 1999, 71.
18. Lu, X.; Winnik, M. A. Luminescence quenching in polymer/filler nanocomposite films used in oxygen sensors 2001, 13, 3449–3463.
19. Quaranta, M.; Borisov, S. M.; Klimant, I. Indicators for optical oxygen sensors 2012, 4, 115–157.
20. Elosua, C.; de Acha, N.; Lopez-Torres, D.; Matias, I. R.; Arregui, F. J. Luminescent Optical Fiber Oxygen Sensor following Layer-by-layer Method. Procedia Engineering 2014, 87, 987–990, doi:10.1016/j.proeng.2014.11.324.
21. Response characteristics of thin film oxygen sensors, Pt and Pd octaethylporphyrins in polymer films. Sensors and Actuators B: Chemical 2002, 82, 200–208, doi:10.1016/S0925-4005(01)01006-1.
22. Lee, S. K.; Okura, I. Photostable Optical Oxygen Sensing Material: Platinum Tetrakis(pentafluorophenyl)porphyrin Immobilized in Polystyrene. 1997, 34, 185–188.
23. Chu, C.-S.; Lo, Y.-L. Ratiometric fiber-optic oxygen sensors based on sol–gel matrix doped with metalloporphyrin and 7-amino-4-trifluoromethyl coumarin. Sensors and Actuators B: Chemical 2008, 134, 711–717, doi:10.1016/j.snb.2008.06.022.
24. Guan, W.; Zhou, W.; Lu, J.; Lu, C. Luminescent films for chemo- and biosensing. Chemical Society Reviews 2015, 44, doi:10.1039/c5cs00246j.
25. Decher, G. Fuzzy Nanoassemblies: Toward Layered Polymeric Multicomposites. Science 1997, 277, 1232–1237, doi:10.1126/science.277.5330.1232.
26. Choi, J.; Rubner, M. F. Influence of the degree of ionization on weak polyelectrolyte multilayer assembly. 2005, 38, 116–124, doi:10.1021/ma048596o.
27. Elzbieciak, M.; Zapotoczny, S.; Nowak, P.; Krastev, R.; Nowakowska, M.; Warszyński, P. Influence of pH on the structure of multilayer films composed of strong and weak polyelectrolytes. Langmuir 2009, 25, 3255–3259, doi:10.1021/la803988k.
28. Lakowicz, J. R. Principles of Fluorescence Spectroscopy; Lakowicz, J. R., Ed.; Springer US: Boston, MA, 2006; ISBN 978-0-387-31278-1.
29. Carraway, E. R.; Demas, J. N.; DeGraff, B. A. Luminescence quenching mechanism for microheterogeneous systems. Analytical Chemistry 1991, 63.
30. Carraway, E. R.; Demas, J. N.; DeGraff, B. A.; Bacon, J. R. Photophysics and photochemistry of oxygen sensors based on luminescent transition-metal complexes. Analytical Chemistry 1991, 63, 337–342.
31. Puklin, E.; Carlson, B.; Gouin, S.; Costin, C.; Green, E.; Ponomarev, S.; Tanji, H.; Gouterman, M. Ideality of pressure-sensitive paint. I. Platinum tetra(pentafluorophenyl)porphine in fluoroacrylic polymer. Journal of Applied

Polymer Science 2000, 77, doi:10.1002/1097-4628(20000923)77.
32. Poly(norbornene)s as matrix materials for platinum tetrakis(pentafluorophenyl)porphyrin based optical oxygen sensors. European Polymer Journal 2008, 44, 2558–2566, doi:10.1016/J.EURPOLYMJ.2008.06.012.
33. Draxler, S.; Lippitsch, M. E.; Klimant, I.; Kraus, H.; Wolfbeis, O. S. Effects of polymer matrices on the time-resolved luminescence of a ruthenium complex quenched by oxygen. Journal of Physical Chemistry 1995, 99.
34. Response characteristics of luminescent oxygen sensors. Sensors and Actuators B: Chemical 1995, 29, 251–257, doi:10.1016/0925-4005(95)01691-0.
35. Chu, C.-S.; Lo, Y.-L. Highly sensitive and linear calibration optical fiber oxygen sensor based on Pt(II) complex embedded in sol–gel matrix. Sensors and Actuators B: Chemical 2011, 155, 53–57, doi:10.1016/j.snb.2010.11.023.
36. Hartmann, P.; Leiner, M. J. P.; Lippitsch, M. E. Luminescence quenching behavior of an oxygen sensor based on a Ru(II) complex dissolved in polystyrene. 1995, 67, 88–93.
37. An experimental study about the utilization of Liquicoat® solutions for the fabrication of pH optical fiber sensors. Sensors and Actuators B: Chemical 2002, 87, 289–295, doi:10.1016/S0925-4005(02)00248-4.
38. Wang, Q.; Yu, D.; Wang, Y.; Sun, J.; Shen, J. Incorporation of water-soluble and water-insoluble ruthenium complexes into zirconium phosphate films fabricated by the layer-by-layer adsorption and reaction method. Langmuir : the ACS journal of surfaces and colloids 2008, 24, 11684–90, doi:10.1021/la802364z.
39. Su, F.; Alam, R.; Mei, Q.; Tian, Y.; Youngbull, C.; Johnson, R. H.; Meldrum, D. R. Nanostructured oxygen sensor - using micelles to incorporate a hydrophobic platinum porphyrin. PLoS ONE 2012, 7, 1–7, doi:10.1371/journal.pone.0033390.
40. Optical fiber pH sensor based on lossy-mode resonances by means of thin polymeric coatings. Sensors and Actuators B: Chemical 2011, 155, 290–297, doi:10.1016/J.SNB.2010.12.037.
41. Shiratori, S. S.; Rubner, M. F. pH-Dependent Thickness Behavior of Sequentially Adsorbed Layers of Weak Polyelectrolytes. Macromolecules 2000, 33, 4213–4219, doi:10.1021/ma991645q.
42. Elosua, C.; De Acha, N.; Hernaez, M.; Matias, I. R.; Arregui, F. J. Layer-by-Layer assembly of a water-insoluble platinum complex for optical fiber oxygen sensors. Sensors and Actuators, B: Chemical 2015, 683–689, doi:10.1016/j.snb.2014.10.042.

Chapter 4

Comparative study of polymeric matrices embedding Pt-TFFP by means of the Layer-by-Layer nanoassembly technique

In this chapter, the optimization of the sensors was investigated from different angles. First, the optical fiber setup was evaluated. Then, the influence of three different entrapping matrices on the behavior of oxygen sensors is analyzed, this is the main body of the chapter. Once the optimum matrix was chosen, the cross-sensitivity and the reproducibility of the devices were also analyzed. Finally, the influence of the parameters of fabrication (pH of the solutions) in the optimum matrix was also evaluated.[1]

[1] This chapter has been partially published in the papers entitled *Comparative study of polymeric matrices embedding oxygen-sensitive fluorophores by means of Layer-by-Layer technique* and in *Layer-by-Layer assembly of a water–insoluble platinum complex for optical fiber oxygen sensors* both published in Sensors and Actuators: B.

4.1. Introduction

Entrapping matrices play a key role in the behavior of oxygen sensors [1], permitting its adsorption and acting as a barrier against the undesired species [2]. Thus, as explained in the previous chapter, oxygen sensing films are required to exhibit good permeability [3] as well as high porosity [4]. To date, these requirements have been met by employing sol-gel [5], xero-gel [6] and plastic [7] matrices.

Furthermore, the distribution of the luminophore inside the sensing films also determines the sensitivity of oxygen sensors [8]. Although this parameter cannot be controlled by the above mentioned techniques [8], it could be done by utilizing the LbL nanoassembly technique for fabricating the sensors. This method permits to tailor the properties of the sensing structures (thickness and roughness) in the nanometer scale and to modify the permeability of the coatings. Thus, with the goal of analyzing the influence of the polymeric matrices embedding the luminescent indicator, three different cationic polyelectrolytes were utilized for the development of the oxygen sensors. These polycations were poly(diallyldimethylammonium chloride) (PDDA), polyethyleneimine (PEI) and poly(allylamine hydrochloride) (PAH), which were chosen because of their distinct morphological characteristics: whereas the first one gives rise to flat layers [9], the thickness of PEI and PAH layers can be tailored by changing the pH value of their solutions. Both, the affinity for water and the morphology of the three different nanostructures were analyzed: first, hydrophobic coatings are well-known for oxygen sensing purposes as they exhibit good gas permeability [10]. This fact would permit the development of sensors of short response and recovery times. Additionally, the hydrophobicity of these coatings would also decrease the cross-sensitivity of these sensors towards the relative humidity [11].

All those sensors were fabricated employing the sensing material as in the previous chapter, Pt-TFPP, owing to its good chemical and optical properties [12].

Finally, the cross-sensitivity and the aging process of the most sensitive sensor have been analyzed. Additionally, the performance of such sensor has been optimized by tailoring the pH of its cationic solution.

In order to carry out that study and to achieve an optimal deposition of the sensing film, the core diameters of the optical fibers employed have been previously analyzed, as well as the pre-treatment process of the fiber.

4.2. Experimental considerations

4.2.1. Optimization of the optical set-up

When using the reflection architecture for characterizing a sensor, that sensor is connected to the common branch of a bifurcated fiber, whereas the light source and the spectrometer are connected to each one of the independent branches. The coupling of light from the bifurcated fiber to the sensor and backwards suffers from some optical losses due to the different diameters of the fiber cores. Thus, optimizing the dimensions of the fibers is critical in order to minimize the optical losses of the system. The relationship between the diameter of the optical fiber of the sensor and the diameter of the fibers used in the bifurcated fiber is key but the optimal ratio has not been reported in the literature yet. In Figure 4.1 it is shown a schematic representation of the connection of the sensor to the bifurcated fiber. It is assumed that the diameter of the bifurcated fibers is R, whereas the diameter of the sensor fiber can have a different size, r. The intersection area between each branch of the bifurcated fiber and the sensor is denoted as A_S, and it is governed by the following equation:

$$A_S = r^2 \arccos\left(\frac{r}{2R}\right) + R^2 \arccos\left(1 - \frac{r^2}{2R^2}\right) - \frac{1}{2} r\sqrt{4R^2 - r^2} \quad \text{(eq 4.1)}$$

The amount of light that travels from the excitation light source towards the sensor is affected by the transmission factor F_1, which is the ratio between A_S and the total section of the optical fiber connected to the light source. The light that is emitted from the luminescent sensor towards the spectrometer is affected by the transmission factor F_2, which is the ratio between A_S and the total section of the optical fiber connected to the sensor. Their mathematical expressions are the next ones:

$$F_1 = \frac{A_S}{\pi R^2} \quad \text{(eq. 4.2a)} \qquad F_2 = \frac{A_S}{\pi r^2} \quad \text{(eq. 4.2b)}$$

Therefore, a global figure of merit of the connection (F_T) can be defined as the product of these both factors F_1 and F_2:

$$F_T = \frac{A_S^2}{\pi^2 R^2 r^2} \qquad \text{(eq. 4.3)}$$

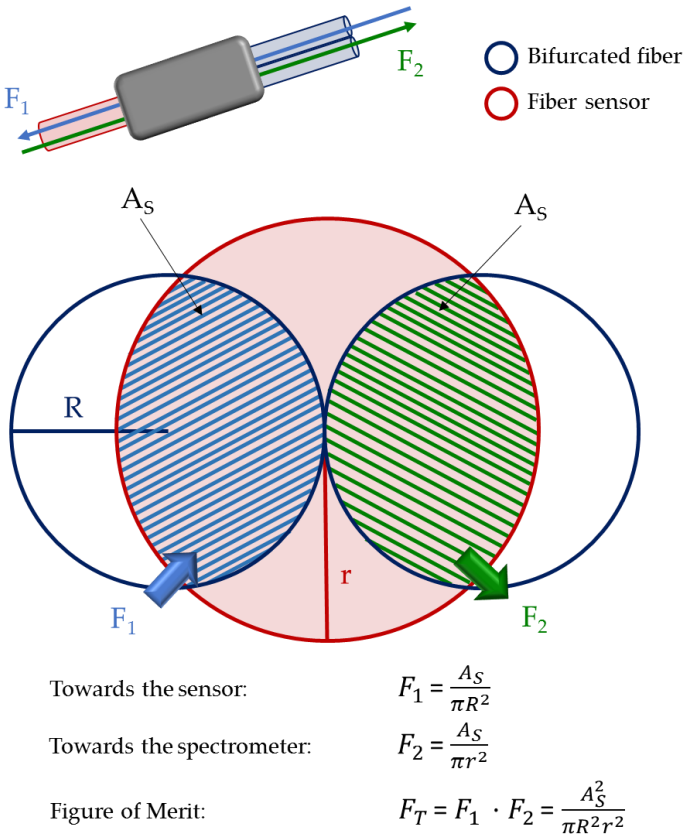

Figure 4.1. Schematic representation of the connection of the bifurcated fiber (radius r) and the sensor (radius R). F_1 represents the light coupled from the light source to the sensor, F_2 is the light guided from the sensor towards the spectrometer and F_T is the figure of merit of the connection.

These three parameters are graphically represented in Figure 4.2: as it can be observed there, the maximum of the total figure of merit ($F_T = 0.26$) of the system is achieved when the relationship between the radius of the sensor (r) and that of the bifurcated fiber (R) is r = 1.8R. This value corresponds approximately to a bifurcated fiber of 600 μm-core diameter and a sensor of 1000 μm-core diameter. In the case of the classic approach, where the fiber probe and the bifurcated fiber have the same diameter, the figure of merit is 0.15, so that with the proposed set-up the reflected optical collected by the spectrometer is enhanced around 70%. In consequence, with the aim of optimizing the signal level in the spectrometer, these dimensions have been chosen for the development of the sensors analyzed in this chapter. For building the sensors on fibers of that thickness, their tips must be polished in order to achieve flat and smooth surfaces: in this manner a proper coupling of the luminescent light to the fiber occurs, and the deposition of the sensing coating on the tip of the fiber is uniform.

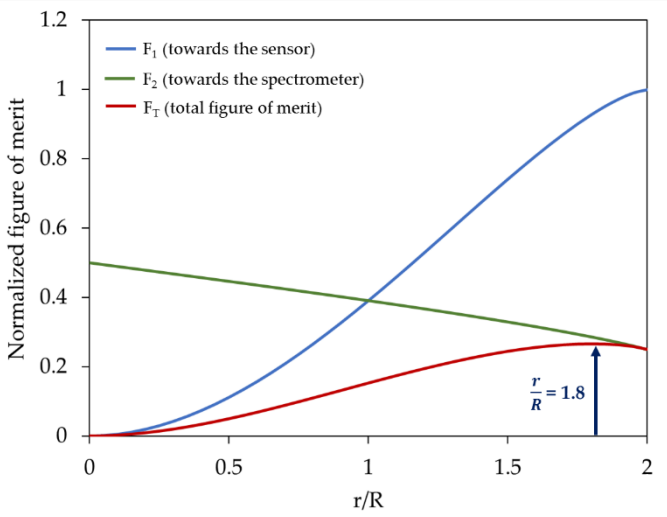

Figure 4.1. Figures of merit of the light that travels from the light source towards the spectrometer (grey line) and from the sensor towards the spectrometer (green line) and figure of merit of the complete system (red line).

4.2.2. Sensing material and entrapping matrices

As it was mentioned previously, this chapter is focused on the study of the influence of different polymeric matrices on the behavior of luminescent oxygen sensors. Thus, the sensitive porphyrin that was employed in the previous chapter has been utilized in the current one: Pt-TFPP. Besides, it has also been entrapped into the anionic micelles formed by SDS.

The main advantage that the LbL technique offers is the possibility to tailor the morphological properties of the sensing structures in the nanometer scale. For instance, when utilizing weak polyelectrolytes, their ionization degree strongly depends on their pH value [13]. In the case of weak cationic polyelectrolytes, they are highly ionized at low pH values, giving rise to flat polymeric chains. Meanwhile, at high pH values, their ionization degree is low, and the obtained layers tend to be thick. Oppositely, there also exist strong polyelectrolytes, whose ionization degree is barely adjustable [14].

The three cationic polyelectrolytes chosen for this study are PDDA, PEI and PAH. The first one, PDDA, is a strong polyelectrolyte widely used for the fabrication of nanostructures employing the LbL technique [15][16]. It gives rise to thin layers of 1 nm thickness [9]. The second polyelectrolyte, PEI, is a weak polyelectrolyte, which is barely ionized at pH 10 (its natural pH) [17]. At that pH value, it gets strongly assembled onto silica surfaces [18] and promotes the adsorption of SDS [19]. The third one, PAH, has been extensively deposited by the LbL technique [20][21], owing to the ease to tailor its properties by changing its pH value [13]. It is also a weak polyelectrolyte, which forms thick layers (around 5 nm at pH 9) at high pH values, due to its low ionization degree in such circumstances [22].

Apart from the cationic polyelectrolytes, the effect of the number of pairs of layers of the sensing structures were studied for each cationic polyelectrolyte. Thus, sensors built up by 10, 20, 30, 40 and 50 pairs of layers were characterized.

4.3. Results

4.3.1. Characterization of the sensing layers

The three different cationic polyelectrolytes that were employed for the fabrication of the sensors gave rise to three different sensing structures: $[PDDA/Pt_{SDS}]_{10}$, $[PEI/Pt_{SDS}]_{10}$ and $[PAH/Pt_{SDS}]_{10}$. To verify the deposition of the layers and ensure the proper assembly of Pt-TFPP inside them, the contact angle of the surfaces as well as the absorption spectra of the films were monitored throughout the construction process onto glass slides. At its end, the morphological properties (thickness and roughness) of the final structures were also analyzed.

As mentioned above, in order to promote a better and faster adsorption of oxygen (i.e., short response and recovery times), the sensing matrices must be as porous and gas permeable as possible. On one side, as rougher coatings exhibit higher porosities, they are expected to promote a better gas adsorption, hence enhancing the sensitivity of the sensors. On the other side, as hydrophobic films show better permeability to gases than hydrophilic ones, the structures that present higher contact angles are supposed to demonstrate faster kinetics. . Thus, the following study analyzes the relationship of the morphology and the affinity for water (contact angle) of the sensing films, with their performances as oxygen sensors, in terms of sensitivity and kinetics.

The absorption spectra at different fabrication stages (2, 6 and 10 pairs of layers) are plotted in Figure 4.3. In all the cases, the absorbance was maximum at 390 nm, which corresponded to the absorption peak of Pt-TFPP [23]. What is more, its value increased as the construction process progressed, indicating the assembly of Pt-TFPP. After the deposition of 10 pairs of layers, absorbance (measured in arbitrary units) at 390 nm was 0.022 in the case of $[PDDA/Pt_{SDS}]_{10}$, 0.025 for $[PEI/Pt_{SDS}]_{10}$ and 0.76 for $[PAH/Pt_{SDS}]_{10}$. These different values were caused by the different thicknesses of the three structures, as it will be observed later.

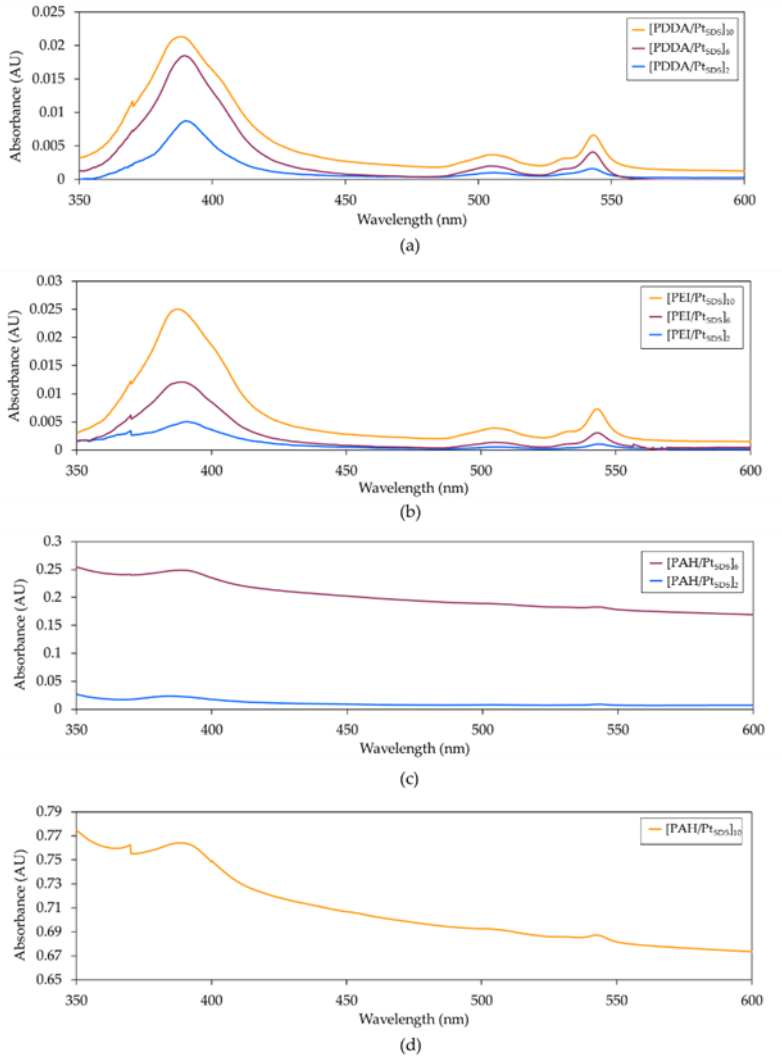

Figure 4.2. Absorption spectra of the three sensing structures at different stages of the construction process: (a) $[PDDA/Pt_{SDS}]_N$, for N = 2, 6 and 10, (b) $[PEI/Pt_{SDS}]_N$, for N = 2, 6 and 10, (c) $[PAH/Pt_{SDS}]_N$, for N = 2 and 6, and (d) $[PAH/Pt_{SDS}]_{10}$.

Throughout the construction process onto glass slides, the contact angle after each deposition step was measured for the three sensing structures, as it is displayed in Figure 4.4. After the pre-treatment process (washing with soap, immersion in KOH and rinse in ultrapure water), the three glass slides presented a contact angle of 25º. When they were coated with the first layer of the cationic polyelectrolytes, it decreased to 15º in the case of PDDA, increased up to 40º for PEI and remained constant for PAH (25º). Once the first layer of the micelles entrapping the Pt-TFPP molecules were deposited, the contact angle increased for the three cases: up to 81º for PDDA, 89º for PEI and 100º in the case of PAH, as a consequence of the hydrophobicity of the sensing material. For the next layer of cationic polyelectrolytes, the value of the contact angle decreased again: up to 52º, 76º and 70º for PDDA, PEI and PAH. This cyclical variation took place until the end of the construction process, demonstrating that every single layer had been deposited.

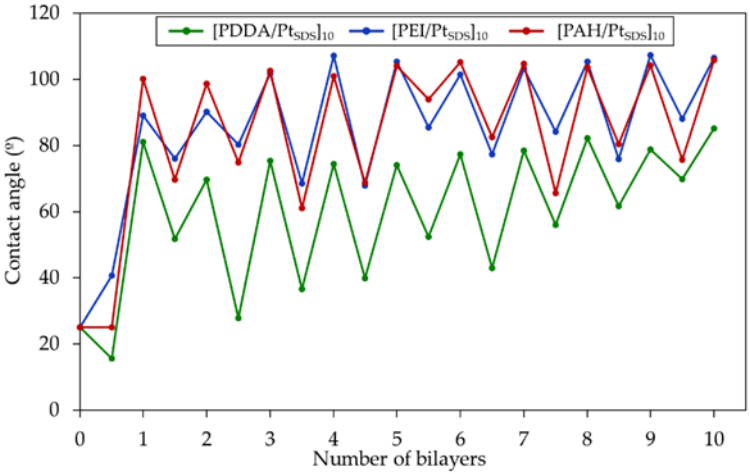

Figure 4.3. Contact angle of the three films utilized for the fabrication of the oxygen sensors. At each deposition step, the Pt_{SDS} increases the contact angle, whereas the cationic polyelectrolyte decreases its value- The $[PEI/Pt_{SDS}]_{10}$ and $[PAH/Pt_{SDS}]_{10}$ coating show the same hydrophobic behaviour, whereas $[PDDA/Pt_{SDS}]_{10}$ exhibits a lower contact angle.

The structures [PEI/Pt$_{SDS}$]$_{10}$ and [PAH/Pt$_{SDS}$]$_{10}$ exhibited a more hydrophobic behavior (contact angles of 103º and 105º, respectively) than [PDDA/Pt$_{SDS}$]$_{10}$ (79º), so they were expected to be more permeable to gas than the latter one, and thus, to show higher sensitivities.

The morphological properties of the three structures were analysed by an Atomic Force Microscope (AFM): after scratching the samples, three profile images were obtained and their thicknesses (measured in nm) were calculated. For measuring the roughness (RMS value in nm), three different areas of each sample were analysed. The obtained values are summarized in Table 4.1. The three structures exhibited dissimilar values of the thickness and roughness: the one built up with PAH was 179.93 nm thick and 21.03 nm rough, oppositely to the one made of PDDA, whose thickness and roughness were 15.1 nm and 6.63 nm, respectively. Meanwhile, the structure fabricated employing PEI exhibited an intermediate behaviour: its thickness was 36.54 nm, and its roughness was 9.5 nm.

Structure	Thickness (nm)	Roughness (nm)
[PDDA/Pt$_{SDS}$]$_{10}$	15.1	6.63
[PEI/Pt$_{SDS}$]$_{10}$	36.54	9.5
[PAH/Pt$_{SDS}$]$_{10}$	179.93	21.03

Table 4.1. Thickness and roughness obtained from AFM images of the three sensing structures.

The same construction processes were carried out onto the tip of unclad optical fibers of 1 mm-core diameter, which were examined with a Scanning Electron Microscope (SEM). The obtained SEM images are shown in Figure 4.5, and they confirm the roughness results measured with the AFM: whereas the structure built with PDDA is the less rough one, the PAH matrix is the roughest.

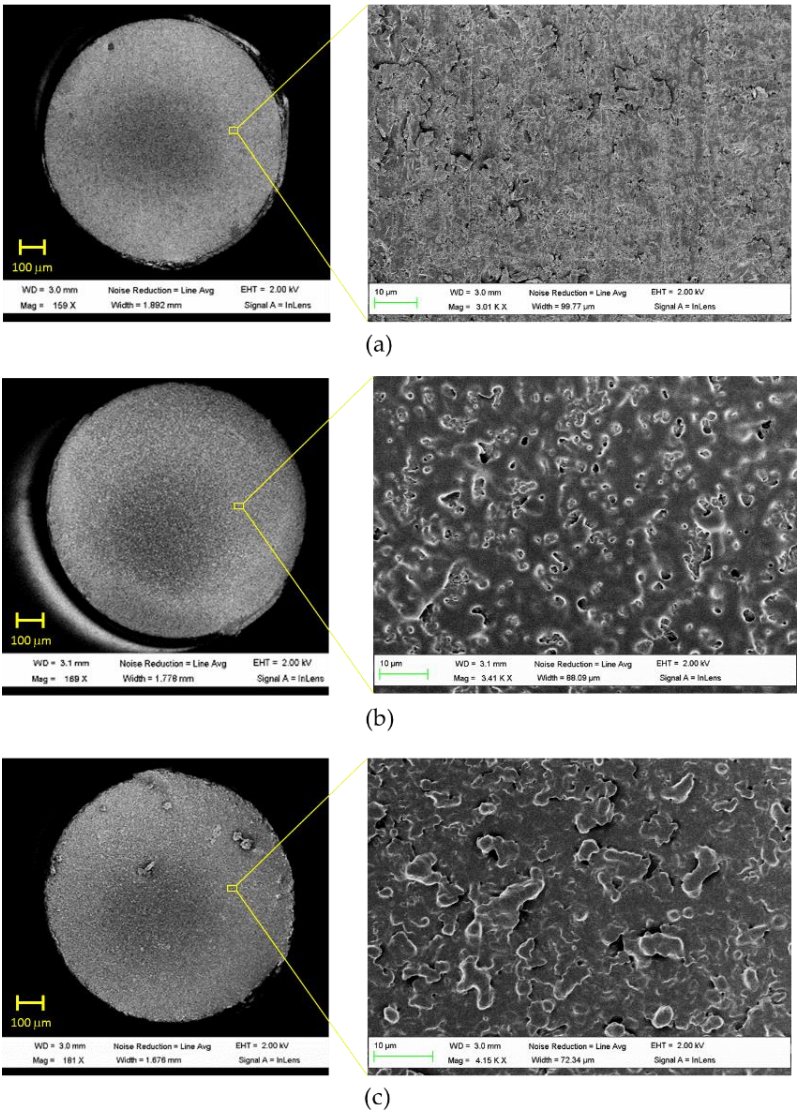

Figure 4.4. Detailed SEM images from the sensing films deposited on the cleaved end of optical fibers for (a) $[PDDA/Pt_{SDS}]_{10}$, (b) $[PEI/Pt_{SDS}]_{10}$ and (c) $[PAH/Pt_{SDS}]_{10}$.

In the following section, it will be analyzed in detail which one of these properties (the affinity for water or the morphology of the films) influences more the response of the sensors towards oxygen, in terms of sensitivity and kinetics.

4.3.2. Characterization of the sensors

The continuous exposure to a light source degrades the luminescent molecules, yielding to the decrease of the emitted intensity. Thus, the photobleaching suffered by each sensor was analyzed by exposing them for 90 nm to the illumination of a LED centered at 390 nm. Every 10 minutes, the oxygen concentration was reduced to 0% (in order to maximize the luminescence and have the same atmosphere in each measurement), and the emitted intensity was monitored. The mathematical expressions of the photobleaching of each sensor are summarized in Table 4.2: all of them follow an exponential trend which can be mathematically compensated when calibrating the sensors. Besides, it can be observed that the intensity of the sensor built up of PAH will be the first one to be stabilized, whereas it will take longer to the intensity decay of $[PDDA/Pt_{SDS}]_{10}$ to reach stability.

Sensor	Photobleaching
$[PDDA/Pt_{SDS}]_{10}$	$1- 0.15e^{-\frac{316.8}{t}}$
$[PEI/Pt_{SDS}]_{10}$	$1- 0.18e^{-\frac{486}{t}}$
$[PAH/Pt_{SDS}]_{10}$	$1- 0.18e^{-\frac{986.4}{t}}$

Table 4.2. Mathematical expressions of the photobleaching suffered by each sensor. The time (t) is measured in seconds.

The sensitivity of the three sensors was analyzed by exposing them to different oxygen concentrations in the range from 0% to 100%. According to the mathematical models presented in equations 3.2 and 3.3, the different quenching constants of the sensors were calculated, and they are shown in detail in Table 4.3. The calibrations curves are plotted in Figure 4.6, and their mathematical expressions are presented in Table 4.4.

Sensor	Stern-Volmer constants			
	f_1	k_1	f_2	k_2
$[PDDA/Pt_{SDS}]_{10}$	0.833	0.449	0.167	0.002
$[PEI/Pt_{SDS}]_{10}$	0.986	0.420	0.014	-0.003
$[PAH/Pt_{SDS}]_{10}$	1	1.580	0	-

Table 4.3. Quenching constants of the different population in which the luminophores are distributed in the three coatings.

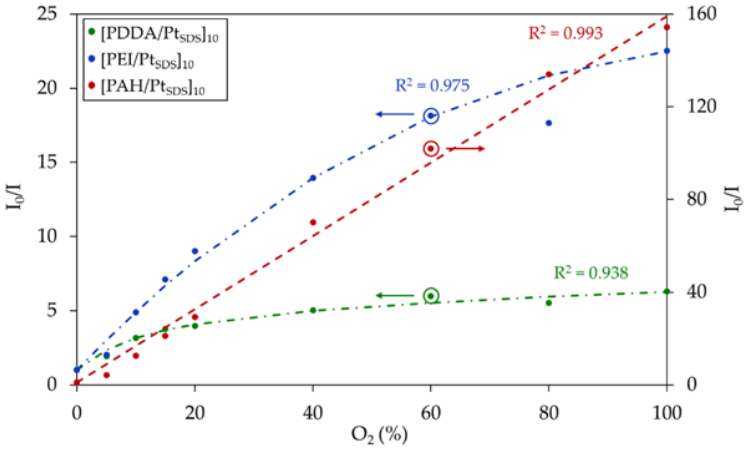

Figure 4.5. Calibration curves of Sensors $[PDDA/Pt_{SDS}]_{10}$, $[PEI/Pt_{SDS}]_{10}$ and $[PAH/Pt_{SDS}]_{10}$.

Sensor	Mathematical model	R^2
$[PDDA/Pt_{SDS}]_{10}$	$\frac{I_0}{I} = \left(\frac{0.833}{1 + 0.449 \cdot [O_2]} + \frac{0.167}{1 + 0.002 \cdot [O_2]}\right)^{-1}$	0.938
$[PEI/Pt_{SDS}]_{10}$	$\frac{I_0}{I} = \left(\frac{0.986}{1 + 0.420 \cdot [O_2]} + \frac{0.014}{1\text{-}0.003 \cdot [O_2]}\right)^{-1}$	0.989
$[PAH/Pt_{SDS}]_{10}$	$\frac{I_0}{I} = 1 + 1.58 \cdot [O_2]$	0.993

Table 4.4. Calibration curves of the three sensors under study.

When comparing the I_0/I_{100} ratios of the three sensors, it can be observed that the one fabricated with PAH exhibited a ratio I_0/I_{100} = 158, six times greater than that of the sensor built up with PEI (I_0/I_{100} = 22.5), and more than thirty times greater than the sensor made of PDDA (I_0/I_{100} = 5). Furthermore, the calibration curve of $[PAH/Pt_{SDS}]_{10}$ was linear and showed a single quenching constant K_{SV} = 1.58, whereas plots of $[PDDA/Pt_{SDS}]_{10}$ and $[PEI/Pt_{SDS}]_{10}$ can be mathematically described with the two-sites model presented in Section 3.2 of the precedent chapter, with a non-negligible K_{SV2}. As it was mentioned in that Section 3.2, when this happens it is an indication that the luminescent particles are heterogeneously distributed into the embedding matrix and not all them are equally affected by oxygen. This fact demonstrated that the luminophore distribution inside these two matrices was not homogeneous and, in consequence, not all the luminescent particles were equally affected by oxygen. According to the mathematical models that fit the experimental curves, in the case of $[PDDA/Pt_{SDS}]_{10}$, the 83.3% of the luminescent population was affected by a quenching constant $K_{SV,1}$ = 0.449, whereas the 16.7% was barely quenched ($K_{SV,2}$ = 0.002). For its part, the luminophore distribution in $[PEI/Pt_{SDS}]_{10}$ was more homogeneous than in $[PDDA/Pt_{SDS}]_{10}$: since the 98.6% of the population was quenched according to $K_{SV,1}$ = 0.420, only the 1.4% of the luminophores was hardly affected by oxygen ($K_{SV,2}$ = -0.003).

When working at low oxygen concentrations, the resolution of the sensors is a crucial parameter. Thus, every sensor was exposed to

variations in the oxygen concentration of 0.1% in the range from 3% to 5% of oxygen (lower oxygen concentrations than the 3% cannot be obtained with the EL-Mass Flow Meters). That parameter, as well as the working range of the sensors, are summarized in Table 4.5. Besides, the recorded relative luminescence spectra for oxygen concentration between 0% and 5% are displayed in Figure 4.7.

Sensor	Linear range [O_2]	Resolution [O_2]
$[PDDA/Pt_{SDS}]_{10}$	0% - 10%	0.5%
$[PEI/Pt_{SDS}]_{10}$	0% - 15%	0.25%
$[PAH/Pt_{SDS}]_{10}$	0% - 100%	0.1%

Table 4.5. Linear range and resolution of the three sensors analyzed.

The distribution of the luminophore inside the sensing coatings also determined the linear range of detectable oxygen concentrations of the three sensors: whereas the response of the $[PDDA/Pt_{SDS}]_{10}$ sensor was linear for oxygen concentrations in the range from 0% to 10%, and the minimum detectable variation was of 0.5% of oxygen, $[PEI/Pt_{SDS}]_{10}$ exhibited a broader linear detection range, up to 15% of oxygen, and it was capable to detect variations of the gas of 0.25%. Oppositely, $[PAH/Pt_{SDS}]_{10}$ worked linearly in the whole range, from 0% to 100% of oxygen, and variations as small as 0.1% of oxygen were detectable by this sensor.

Comparing the sensitivities of the sensors to the characteristics of the films, it does not seem that the hydrophilicity or hydrophobicity of the coatings determined their sensitivity towards oxygen: $[PEI/Pt_{SDS}]_{10}$ and $[PAH/Pt_{SDS}]_{10}$ coatings exhibited similar affinity to water (contact angle), however, the sensitivity of $[PAH/Pt_{SDS})]_{10}$ was six times higher than that of $[PEI/Pt_{SDS}]_{10}$. Oppositely, there was a direct relationship between the

roughness of the coatings and their sensitivity: whereas [PDDA/Pt_{SDS}]$_{10}$ was the coating with lower roughness, it was also the less sensitive and, as the roughness of the films increased, also did the sensitivity, being [PAH/Pt_{SDS})]$_{10}$ the roughest, and also the most sensitive one.

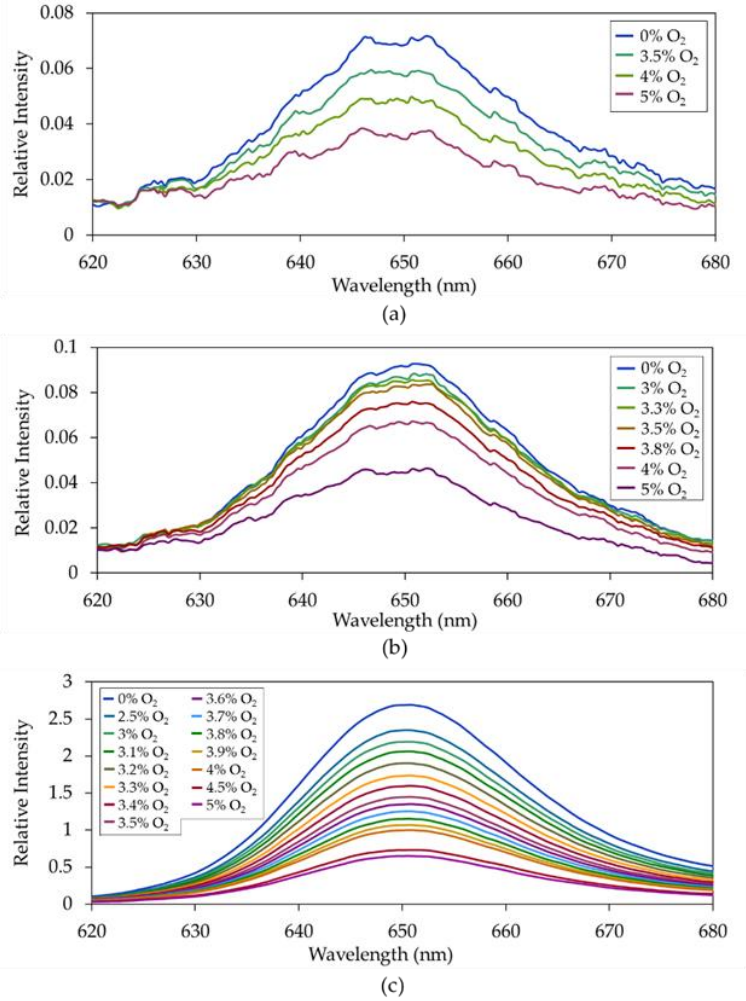

Figure 4.6. Relative intensity of the luminescent peaks of each sensor: (a) [PDDA/Pt_{SDS}]$_{10}$, (b) [PEI/Pt_{SDS}]$_{10}$, and (c) [PAH/Pt_{SDS}]$_{10}$.

For analyzing the kinetics of the three sensors, they were exposed to variations from oxygen-saturated (100%) to completely de-oxygenated (0%) atmospheres. The variations of the normalized intensity (0 for 0% oxygen and 1 for 100% oxygen) under these changes are plotted in Figure 4.8(a), and a falling edge is shown in detail in Figure 4.8(b). $[PDDA/Pt_{SDS}]_{10}$ exhibited the largest response time, 6 seconds, whereas it took 3.6 and 4 seconds to $[PEI/Pt_{SDS}]_{10}$ and $[PAH/Pt_{SDS}]_{10}$, respectively, to respond to change from 0% to 100% oxygen. In the case of the recovery times, the shortest one corresponded to $[PAH/Pt_{SDS}]_{10}$ (12 seconds). Meanwhile, the time needed to recover the baseline by sensors $[PDDA/Pt_{SDS}]_{10}$ and $[PEI/Pt_{SDS}]_{10}$ were considerably greater, 30 and 20.4 seconds, respectively, therefore recovery time is the most critical time parameter. These data are summarized in Table 4.6. It is important to notice that this improvement in the temporal parameters is observed in spite of being the $[PAH/Pt_{SDS}]_{10}$ and $[PEI/Pt_{SDS}]_{10}$ 12- and 2.4-fold thicker than the $[PDDA/Pt_{SDS}]_{10}$ coating respectively, see Table 4.1. This much higher thickness would theoretically worsen the response and recovery time (Fick's law). On the other hand, the PEI and PDDA matrices have shown the same contact angles, see Figure 4.4, therefore the hydrophobicity is not the determinant property to improve the dynamic response of the sensor. Moreover, it seems that there is an inverse correlation between roughness and recovery time: the rougher the coating is, the shorter recovery time. Observing carefully the SEM images of Figure 4.5 it seems that this roughness is an indirect measurement of the porosity of the films and this would explain the enhancement of the recovery time.

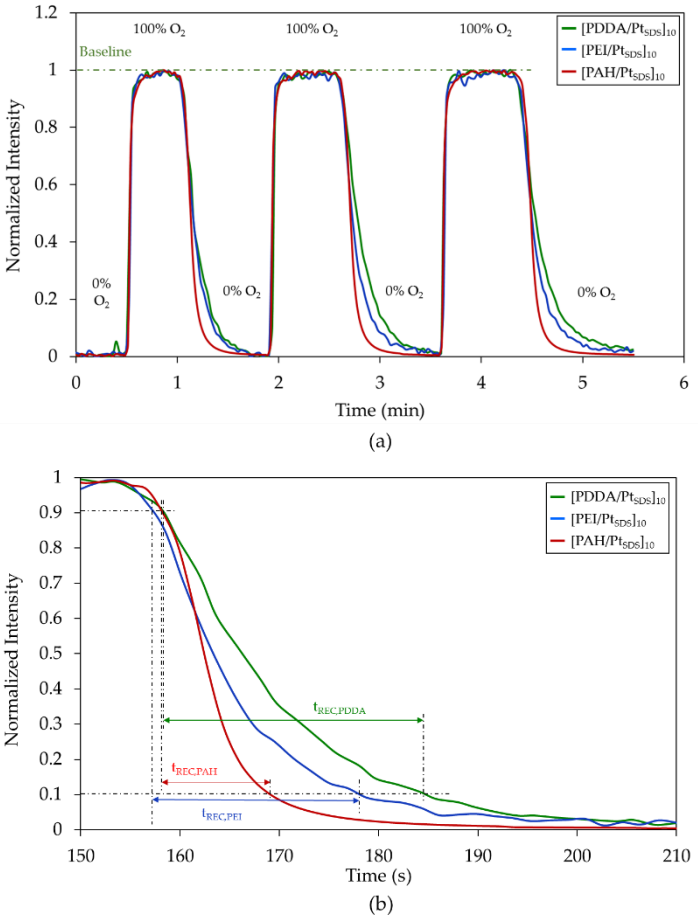

Figure 4.7. (a) Response of the three sensors to dynamic variations of the oxygen concentration from 0% to 100%. (b) Detail of the falling tail of the sensors, where it can be observed that $[PAH/Pt_{SDS}]_{10}$ recovery time is shorter than $[PEI/Pt_{SDS}]_{10}$ and $[PDDA/Pt_{SDS}]_{10}$.

Sensor	Response time (s)	Recovery time (s)
$[PDDA/Pt_{SDS}]_{10}$	6	30
$[PEI/Pt_{SDS}]_{10}$	3.6	20.4
$[PAH/Pt_{SDS}]_{10}$	4.2	12

Table 4.6. Response and recovery times of the three sensors.

4.3.3. Cross-sensitivity and aging process

Apart from the above analyzed parameters, which determine the suitability of the sensors for certain applications, there are others that must be taken into account. For instance, their behavior towards changes of the environmental variables (temperature and relative humidity) and their aging. Thus, all these parameters were analyzed for $[PAH/Pt_{SDS}]_{10}$, which exhibited the best features in terms of sensitivity and kinetics in the previous section.

The $[PAH/Pt_{SDS}]_{10}$ sensor was placed inside a climatic chamber at a constant relative humidity of 35%, and the temperature was increased from 15 ºC to 45 ºC in steps of 5 ºC, causing a decreased of the relative intensity of 2.7% per Celsius degree, owing to the dependency of the luminescence intensity of Pt-TFPP on temperature [5][24]. Once the temperature decreased, the luminescence intensity did not recover its original value, what was probably a consequence of the degradation that the indicator suffers at high temperatures. When the temperature was kept constant at 25 ºC, and the relative humidity was cyclically changed from 20% to 80%, the maximum signal variation was of the 8%, showing a low cross-sensitivity towards this parameter, what was likely to happen because the hydrophobic nature of the sensing coating [25]. Both stages are plotted in Figure 4.9(a) in the case of temperature variations and Figure 4.9(b) for relative humidity changes.

The aging process was tested by calibrating a $[PAH/Pt_{SDS}]_{10}$ sensor at three different moments: a day, two weeks and a month after their fabrication. The resulting curves are plotted in Figure 4.10(a) and the I_0/Ii ratios for oxygen concentrations of 40%, 60% and 100% of oxygen are displayed in Figure 4.10(b). In the first two weeks the value of these ratios decreased around a 10%, and from the 14^{th} day to the 30^{th} day, the decreases were lower than 3.5%. The same happened to the quenching constants of the sensors, demonstrating that the aging process had stabilized. Although for further calibration of the sensors this aging process could be mathematically modeled and compensated, a curing treatment for avoiding the decrease of the sensitivity would be a better option: this was tried to achieve with a thermal treatment of a sensor at 70 ^{o}C in a vacuum atmosphere for an hour. However, no difference between the non-treated and the treated sensors was found. Thus, an alternative chemical curing process should be investigated.

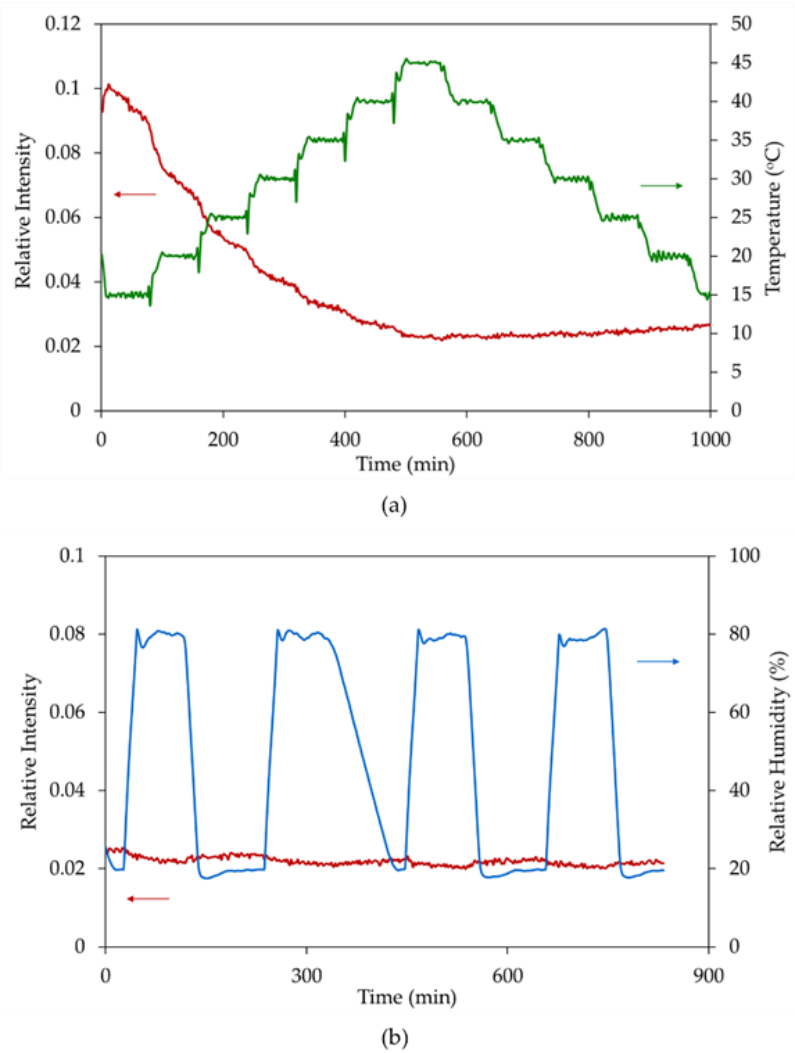

Figure 4.8. Changes in the relative luminescence intensity caused by (a) temperature variations at constant relative humidity (35%) and by (b) relative humidity variations at constant temperature (25 ºC).

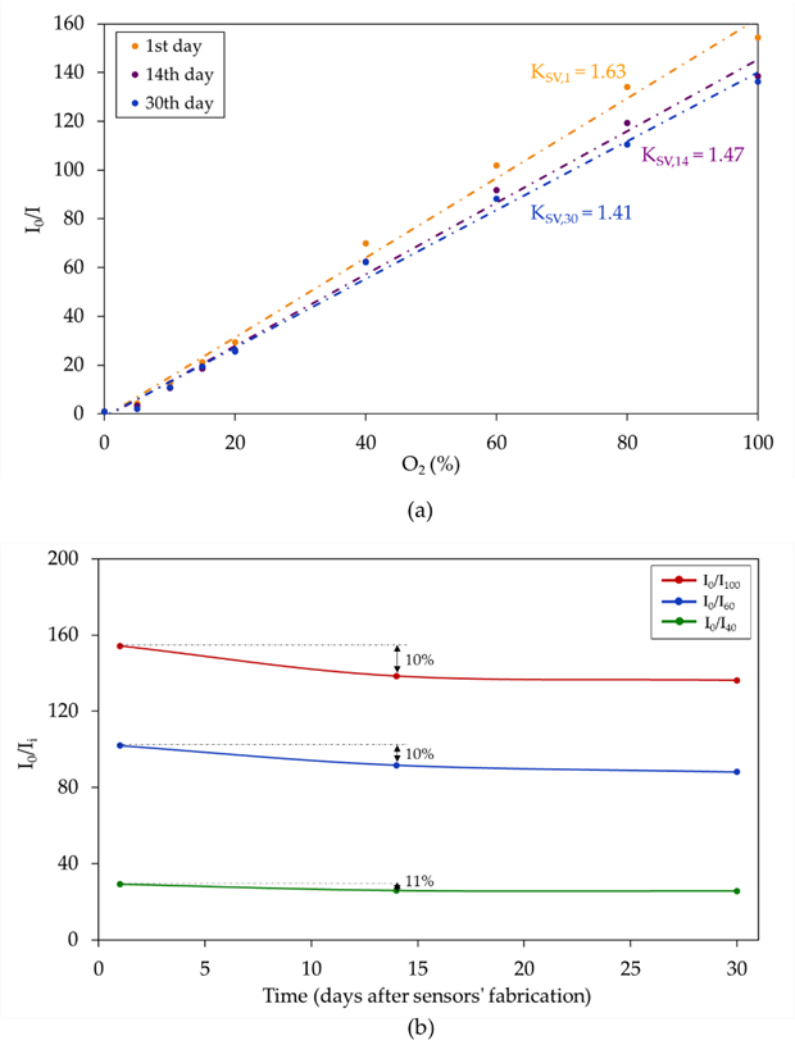

Figure 4.9. Evolution of the ratios I_0/I_{20}, I_0/I_{60} and I_0/I_{100} over a month. Decreases after two weeks are expressed in%.

4.3.4. Sensor optimization

As it its well known, the thickness of the PAH layers depends on the pH value of their solution [13]. Thus, the sensor [PAH/Pt_{SDS}]$_{10}$ was tried to be optimized by changing the original value of that parameter (pH 10) to 8 and 12: at pH 8, PAH is more ionized than at pH 10, yielding to thinner layers. Thus, the spacing distance between the luminescent films was expected to decrease and hence, due to a higher self-quenching, the sensitivity. When the pH value is fixed at 12, PAH is barely ionized, so the PAH layers are thicker. Therefore, this structure was supposed to be the thickest one, what could give rise to two opposite behaviors of the sensor: on one hand, as the luminescent films are more spaced from each other, the self-quenching decreases, resulting in an increase of the sensitivity. On the other hand, due to the thickness of the sensing film, the inner luminescent layers are not accessible to oxygen, so they are not quenched by its presence. This fact could also lead to a non-linear calibration curve. Three different sensors with the same structure, [PAH/Pt_{SDS}]$_{10}$, but distinct pH values of PAH (8, 10 and 12) were fabricated at the same time. Then, they were exposed to different oxygen concentrations and their calibration curves were obtained. They are summarized in Table 4.7 and displayed in Figure 4.11.

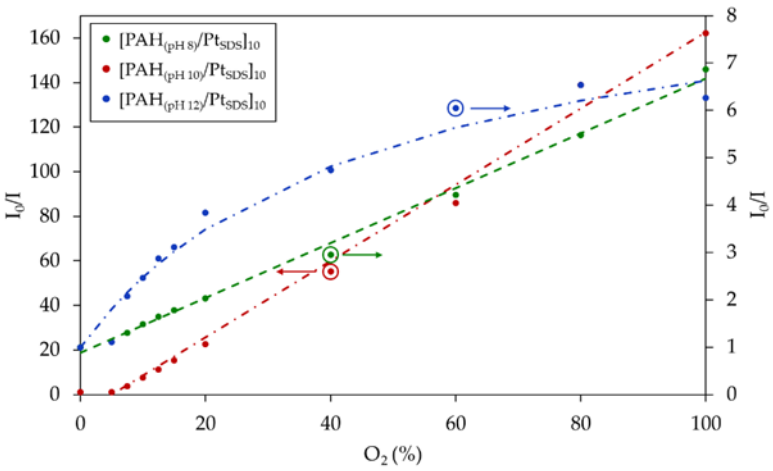

Figure 4.10. Calibration curves of the three sensors fabricated with the structure [PAH/Pt$_{SDS}$]$_{10}$ for different values of the PAH solution: pH 8 (green) pH 10 (red) and pH 12 (blue). The dots correspond to the measured data and the dashed lines to the mathematical models.

Analyzing the calibration curves of the three sensors, it can be seen that when using PAH at pH 8, although the sensitivity of the sensor decreased to 0.058 (almost 30 times), its behavior was still linear. The sensor fabricated with PAH at pH 12 did not behave in the same way: in addition to the decrease of the sensitivity, the calibration curve was not linear. According to the two-sites model proposed by Carraway et al. (eq. 3.3) [26], whereas the 89% of the Pt-TFPP particles were affected by the quenching constant K_{sv} = 0.2018, the 11% of them were barely quenched by oxygen (K_{sv} = 0.0001). Meanwhile, the sensor built up with PAH at pH 10 exhibited the same behavior as the analyzed in previous sections. This distinct behavior of the sensors caused by changes in the pH value of the PAH solutions could be explained by the dependence of the thickness of PAH layers on that parameter [13]: the higher is the pH value, the lower is its ionization degree. Thus, at pH 12 PAH was barely ionized, so the cationic layers were the thickest. This fact explained that at high oxygen concentrations, even at 100%, the luminescence peak was not totally quenched: due to the thickness of the structure [PAH (pH 12)/Pt$_{SDS}$]$_{10}$, the

inner layers of Pt-TFPP were not affected by oxygen and, in consequence, their luminescence was not quenched. In the case of employing PAH at pH 8, these cationic layers were the thinnest: despite the distribution of the Pt-TFPP inside the matrix was homogeneous, the spacing distance between the luminescent layers might not be enough to avoid the self-quenching, so the sensitivity of the sensor decreased.

Sensor	Stern-Volmer constants			
	f_1	k_1	f_2	k_2
$[PAH\ (pH\ 8)/Pt_{SDS}]_{10}$	1	0.058	0	-
$[PAH(pH\ 10)/Pt_{SDS}]_{10}$	1	1.71	0	-
$[PAH(pH\ 12)/Pt_{SDS}]_{10}$	0.89	0.2018	0.11	0.0001

Table 4.7. Quenching constants of the three sensors fabricated with the structure $[PAH/Pt_{SDS}]_{10}$ for different values of the PAH solution: pH 8, pH 10 and pH 12.

Furthermore, all the sensors built up under the same conditions (i.e., PAH at pH 10) exhibited similar calibration curves, what demonstrated the reproducibility of the fabrication procedure.

4.4. Conclusions

In this chapter, it has been analyzed how the different properties of the embedding matrices fabricated by means of the LbL technique affect the behavior of the oxygen sensors. In the three cases, the sensing indicator was the platinum metalloporphyrin Pt-TFPP, which was entrapped inside the anionic micelles of SDS. As cationic counterparts, three distinct polyelectrolytes were utilized: PDDA, PEI and PAH, giving rise to the sensing structures $[PDDA/Pt_{SDS}]_{10}$, $[PEI/Pt_{SDS}]_{10}$ and $[PAH/Pt_{SDS}]_{10}$. These coatings exhibited distinct morphological properties as well as different affinity for water: whereas $[PDDA/Pt_{SDS}]_{10}$ was the thinnest, the less rough and the most hydrophilic one, $[PAH/Pt_{SDS}]_{10}$ was the roughest and the thickest. However, the hydrophobicity of $[PDDA/Pt_{SDS}]_{10}$ was similar than that of $[PEI/Pt_{SDS}]_{10}$. After exposing the sensors to different oxygen concentrations, and comparing the obtained results with the properties of the coatings, it can be inferred that there is a correlation between the roughness of the sensing films and the sensitivity of the sensors: the rougher is the film, the more sensitive is the sensor. Besides, the thicker were the films, the more homogeneous was the luminophore distribution inside the entrapping matrix, so the more linear was the calibration curve. In addition, it seems that the spacing distance (the thickness of the layers) between the luminescent monolayers could affect the luminescence intensity, what implies a different sensitivity: the smaller is that distance, the closer are the luminescent films to each other and the higher is the self-quenching. This assumption opens the door to further research in which the effect of the spacing distance could be studied and optimized, this will be presented in the next chapter.

Apart from that, the aging process and the cross-sensitivity towards temperature and RH of the $[PAH/Pt_{SDS}]_{10}$ sensor (which exhibited the highest sensitivity), were tested. Related to the aging process, the sensitivity of the sensor decreased up to 10% for the first two weeks, and stabilized afterwards. Although this process can be mathematically modeled, some treatment could improve this behavior. In the case of the cross-sensitivity, the luminescent intensity decreased as temperature

increased, which is consistent with the behavior of the luminescent materials. However, it was barely affected by changes in the relative humidity, due to the hydrophobic nature of the PAH sensing coating.

Furthermore, the influence of the pH of the polyelectrolyte used in the LbL process was demonstrated: by tailoring the pH value of the PAH solutions, the thickness of these layers was also modified, changing not only the sensitivity of the sensors, but also the distribution of the luminophore inside the sensing matrix.

Finally, the similar sensitivities exhibited by the $[PAH/Pt_{SDS}]_{10}$ sensors fabricated in the same circumstances (pH 10) demonstrated the reproducibility of LbL technique for the fabrication of luminescence-based sensors.

Bibliography

1. DiMarco, G.; Lanza, M. Optical solid-state oxygen sensors using metalloporphyrin complexes immobilized in suitable polymeric matrices. *Sensors Actuators B Chem.* **2000**, *63*, 42–48, doi:10.1016/S0925-4005(00)00299-9.
2. Koren, K.; Hutter, L.; Enko, B.; Pein, A.; Borisov, S. M.; Klimant, I. Tuning the dynamic range and sensitivity of optical oxygen-sensors by employing differently substituted polystyrene-derivatives. *Sens. Actuators. B. Chem.* **2013**, *176*, 344–350, doi:10.1016/j.snb.2012.09.057.
3. Basu, B. J. Optical oxygen sensing based on luminescence quenching of platinum porphyrin dyes doped in ormosil coatings. *Sensors Actuators, B Chem.* **2007**, *123*, 568–577, doi:10.1016/j.snb.2006.09.062.
4. McDonagh, C.; Bowe, P.; Mongey, K.; MacCraith, B. . Characterisation of porosity and sensor response times of sol–gel-derived thin films for oxygen sensor applications. *J. Non. Cryst. Solids* **2002**, *306*, 138–148, doi:10.1016/S0022-3093(02)01154-7.
5. Chu, C.-S.; Lin, T.-H. Ratiometric optical sensor for dual sensing of temperature and oxygen. *Sensors Actuators B Chem.* **2015**, *210*, 302–309, doi:10.1016/j.snb.2014.12.133.
6. Chu, C.-S.; Sung, T.-W.; Lo, Y.-L. Enhanced optical oxygen sensing property based on Pt(II) complex and metal-coated silica nanoparticles embedded in sol–gel matrix. *Sensors Actuators B Chem.* **2013**, *185*, 287–292, doi:10.1016/j.snb.2013.05.011.
7. Mills, A.; Lepre, A. Controlling the Response Characteristics of Luminescent Porphyrin Plastic Film Sensors for Oxygen. *Anal. Chem.* **1997**, *69*, 4653–4659, doi:10.1021/ac970430g.
8. Hartmann, P.; Leiner, M. J. P.; Lippitsch, M. E. Luminescence quenching behavior of an oxygen sensor based on a Ru(II) complex dissolved in polystyrene. **1995**, *67*, 88–93.
9. Lvov, Y.; Möhwald, H. Protein architecture; interfacing molecular assemblies and immobilization biotechnology 2000.
10. Missner, A.; Kügler, P.; Antonenko, Y. N.; Pohl, P. Passive transport across bilayer lipid membranes: Overton continues to rule. *Proc. Natl. Acad. Sci. U. S. A.* **2008**, *105*, doi:10.1073/pnas.0809606106.
11. Zhang, W.; Hu, Y.; Ge, J.; Jiang, H.-L.; Yu, S.-H. A facile and general coating approach to moisture/water-resistant metal-organic frameworks with intact porosity. *J. Am. Chem. Soc.* **2014**, *136*, 16978–81, doi:10.1021/ja509960n.
12. Puklin, E.; Carlson, B.; Gouin, S.; Costin, C.; Green, E.; Ponomarev, S.; Tanji, H.; Gouterman, M. Ideality of pressure-sensitive paint. I. Platinum tetra(pentafluorophenyl)porphine in fluoroacrylic polymer. *J. Appl. Polym. Sci.* **2000**, *77*, doi:10.1002/1097-4628(20000923)77.
13. Choi, J.; Rubner, M. F. Influence of the degree of ionization on weak polyelectrolyte multilayer assembly. **2005**, *38*, 116–124, doi:10.1021/ma048596o.
14. Tonneau, D.; Clément, N.; Houel, A.; Bonnail, N.; Dallaporta, H.; Safarov, V. Chemical physics of thin film deposition processes for micro- and nano-technologies. *NATO ASI Ser.*

15. Guice, K. B.; Lvov, Y. M.; McShane, M. J. Nanoengineered microcapsules for the fluorescent sensing of oxygen 2nd Joint Conference of the IEEE Engineering in Medicine and Biology Society and the Biomedical Engineering Society. In *Annual International Conference of the IEEE Engineering in Medicine and Biology - Proceedings*; 2002; Vol. 2.
16. Wang, Y.; Wang, S.; Xiao, M.; Han, D.; Hickner, M. A.; Meng, Y. Layer-by-layer self-assembly of PDDA/PSS-SPFEK composite membrane with low vanadium permeability for vanadium redox flow battery. *RSC Adv.* **2013**, *3*, 15467–15474, doi:10.1039/c3ra41670d.
17. Wang, H.; Wang, Y.; Yan, H.; Zhang, J.; Thomas, R. K. Binding of sodium dodecyl sulfate with linear and branched polyethyleneimines in aqueous solution at different pH values. *Langmuir* **2006**, *22*, 1526–33, doi:10.1021/la051988j.
18. Zhang, X.; Taylor, D.; Thomas, R.; Penfold, J.; Tucker, I. Modifying the adsorption properties of anionic surfactants onto hydrophilic silica using the pH dependence of the polyelectrolytes PEI, ethoxylated PEI, and polyamines. *Langmuir* **2011**, *27*, 3569–77, doi:10.1021/la1046723.
19. Penfold, J.; Tucker, I.; Thomas, R. K.; Zhang, J. Adsorption of polyelectrolyte/surfactant mixtures at the air-solution interface: poly(ethyleneimine)/sodium dodecyl sulfate. *Langmuir* **2005**, *21*, 10061–73, doi:10.1021/la0505014.
20. Zhang, G.; Shitole, P. S.; Pujari, R. A.; Charnani, V. S.; McShane, M. J.; Robinson, C. J. Intrinsic optical signal imaging of a ratiometric fluorescence oxygen nanosensor. In *2005 3rd IEEE/EMBS Special Topic Conference on Microtechnology in Medicine and Biology*; 2005; Vol. 2005.
21. Guo, Y.; Geng, W.; Sun, J. Layer-by-layer deposition of polyelectrolyte-polyelectrolyte complexes for multilayer film fabrication. **2009**, *25*, 1004–1010, doi:10.1021/la803479a.
22. Shiratori, S. S.; Rubner, M. F. pH-dependent thickness behavior of sequentially adsorbed layers of weak polyelectrolytes. *Macromolecules* **2000**, *33*, 4213–4219, doi:10.1021/ma991645q.
23. Chu, C.-S.; Lo, Y.-L. Ratiometric fiber-optic oxygen sensors based on sol–gel matrix doped with metalloporphyrin and 7-amino-4-trifluoromethyl coumarin. *Sensors Actuators B Chem.* **2008**, *134*, 711–717, doi:10.1016/j.snb.2008.06.022.
24. Chu, C.-S.; Lin, T.-H. A new portable optical sensor for dual sensing of temperature and oxygen. *Sensors Actuators B Chem.* **2014**, *202*, 508–515, doi:10.1016/j.snb.2014.05.125.
25. McGaughey, O.; Ros-Lis, J. V.; Guckian, A.; McEvoy, A. K.; McDonagh, C.; MacCraith, B. D. Development of a fluorescence lifetime-based sol–gel humidity sensor. *Anal. Chim. Acta* **2006**, *570*, 15–20, doi:https://doi.org/10.1016/j.aca.2006.03.113.
26. Carraway, E. R.; Demas, J. N.; DeGraff, B. A.; Bacon, J. R. Photophysics and photochemistry of oxygen sensors based on luminescent transition-metal complexes. *Anal. Chem.* **1991**, *63*, 337–342.

Chapter 5

Enhancement of the sensitivity of luminescent oxygen sensors by tuning the distance between the luminophore layers

In this chapter, with the aim of optimizing the luminescence intensity by attenuating the self-quenching, different spacing distances have been introduced between the luminescent layers of oxygen sensors fabricated by the LbL technique. For the different polymeric matrices analyzed, tailoring those distances has permitted the modification and optimization of the sensitivity and the calibration curves of sensors.[1]

[1] This Chapter has been partially published in the paper entitled *Enhancement of luminescence-based optical fiber oxygen sensors by tuning the distance between fluorophore layers* in Sensors and Actuators: B.

5.1. Introduction

In the previous chapters, the Layer-by-Layer assembly of a water-insoluble porphyrin for oxygen sensing purposes was carried out by entrapping it into anionic micelles. Besides, by utilizing different cationic polyelectrolytes for fabricating the sensing films, the role of the entrapping matrices on the performance of the sensors was analyzed. It was found that the morphological properties of the sensing coatings determined the behavior of the oxygen sensors: the rougher the sensing coatings, the higher the sensitivity of the sensors.

Two phenomena that can affect negatively to the performance of luminescence-based sensors are the photobleaching and the self-quenching. The first one, which is a decrease of the emitted intensity as a consequence of the continuous exposure to the light source [1], has been widely studied [2] and can be mathematically modeled [3], as it has been done in chapters three and four. Besides, the platinum porphyrin utilized in this research, Pt-TFPP, it is known for its good photostability [4].

Regarding to the self-quenching, it consists of a decrease of the luminescence intensity due to the high concentration of indicator [5]. As it depends inversely on the distance between the luminophores [6], it can be tailored by varying the separation between the luminescent layers. When fabricating the sensors by means of the LbL technique, this process can be achieved by two different procedures. The first one consists of modifying the ionization degree of the polyelectrolytes layers that act as spacing layers between the luminescent ones: in the case of weak polycations, they are low ionized at high pH values, so the layers are thicker than at low pH values, when they are highly ionized and the functional groups repulse from each other. The second approach involves the introduction of layers of anionic polyelectrolytes between the cationic ones: the larger is the number of layers of polyelectrolytes, the higher is the spacing distance between the luminescent films. In the case of the $[PAH/Pt_{SDS}]_{10}$ sensors analyzed previously the one that utilized PAH at pH 10 exhibited higher sensitivity than those in which its pH value was fixed at 8 or 12. Additionally, PEI promotes a better adsorption of SDS at

pH 10 [7]. Thus, it was decided not to modify this parameter (pH of the solutions) and, consequently, the second method (the introduction of additional layers) was chosen for the current study.

5.2. Experimental considerations

5.2.1. Sensing material and entrapping matrices

With the aim of controlling the spatial order of the luminophore inside the sensing matrix, the LbL technique has been utilized for the fabrication of the oxygen sensors. As oxygen-sensitive material, the platinum porphyrin employed in the previous chapters, Pt-TFPP, has been used in this one. Owing to its water insolubility, it has been also entrapped into anionic micelles of SDS, which make possible its deposition by the LbL technique. As cationic counterparts, PDDA, PEI and PAH have been chosen due to the dissimilar properties of the sensing films to which they give rise [3], which were discussed in the previous chapter. Two different anionic polyelectrolytes were used for increasing the spacing distance between the luminescent layers: poly(styrenesulfonate) (PSS) and poly(acrylic acid) (PAA).

Besides, due to the shorter time needed for the polishing process, 1000 μm-core plastic optical fiber (POF) has been utilized instead of silica fiber.

5.3. Effect of increasing the spacing distance between the luminescent layers

5.3.1. Preliminary experiments: poly(styrene sulfonate) (PSS) as spacing material

As it was mentioned before, the LbL method permits to tailor the spacing distance between the luminescent films by modifying the deposition conditions of the polycations [8], or by introducing anionic polyelectrolytes between the cationic ones. Following this second approach, PSS layers were inserted between the cationic ones. The initial study was carried out by utilizing PAH as cationic counterpart (as it had exhibited the best results in the experiments of the previous chapters). The deposition conditions of PAH, Pt-TFPP and SDS were similar than in the previous experiments: 10 mM of PAH at pH 10 and 0.04 mg/ml of Pt-TFPP entrapped into micelles of 10 mM SDS. In the case of PSS, its concentration was of 10 mM, and, despite being a strong polyelectrolyte [9] which is totally ionized in the whole range of pH values [10], it was tested at different pH values: 2, 4.5 and 10 just to verify any possible influence in the fabrication of the coatings. The structures under study were the following ones:

- $[PAH/Pt_{SDS}]_{10}$
- $[PAH/PSS_{pH\ 2}/PAH/Pt_{SDS}]_{10}$
- $[PAH/PSS_{pH\ 4.5}/PAH/Pt_{SDS}]_{10}$
- $[PAH/PSS_{pH\ 10}/PAH/Pt_{SDS}]_{10}$

The first one corresponded to the sensor analyzed in the previous chapter, in which every sensitive layer was spaced from each other by a single PAH layer. In that sensor, the innermost luminescent film was also separated from the fiber core just by a PAH layer. In the three other cases, the layers containing Pt-TFPP were spaced from each other by three layers of polyelectrolytes: PAH/PSS/PAH. This same structure separated

the innermost Pt-TFPP film from the core of the fiber. In every case, the outermost layer contained the sensing material.

With the aim of obtaining a luminescent intensity as high as possible, a high-power LED centered at 400 nm was utilized. Therefore, it was necessary to use a High Pass Filter (HPF), whose cutoff wavelength was 600 nm, between the sensor and the spectrometer. When the optical fiber was illuminated at that wavelength, it emitted a fluorescence peak centered at 550 nm, which overlapped with the luminescence emitted by Pt-TFPP, as it can be observed in Figure 5.1. By using the above mentioned HPF, it was difficult to characterize mathematically the autofluorescence of the optical fiber since the cutoff wavelength of the filter is higher than the fluorescence peak wavelength of the optical fiber. In other words, the small contribution of the optical fiber fluorescence could not be subtracted from the luminescent peak emitted by the sensors. Thus, although the obtained calibration curves demonstrated which sensors exhibited higher sensitivities, they did not show their real values but slightly higher.

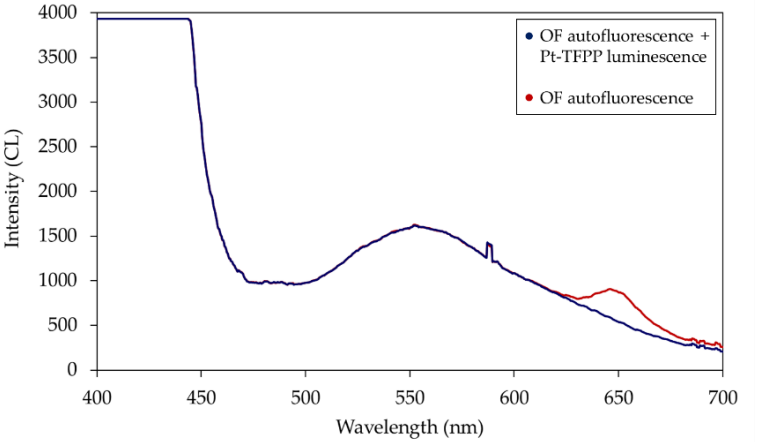

Figure 5.1. Autofluorescence emitted by the optical fiber (blue line) and luminescence intensity emitted by Pt-TFPP (red line) when they are illuminated at 400 nm. As it can be observed, both spectra are overlapped.

The obtained calibration curves demonstrated that when trying to increase the spacing distance between the luminescent films with PSS, the sensitivity of the sensors decreased, as shown in Figure 5.2. Furthermore, owing to the independency of the thickness of the PSS layer on the pH of the solution, the three sensors fabricated with this polyanion showed the same sensitivity. Their I_0/I_{100} ratios were 18.16, 21.14 and 21.8 for the different pH of PSS: 2, 4.5 and 10, respectively. Meanwhile, in the case of using the structure $[PAH/Pt_{SDS}]_{10}$, $I_0/I_{100} = 76.65$.

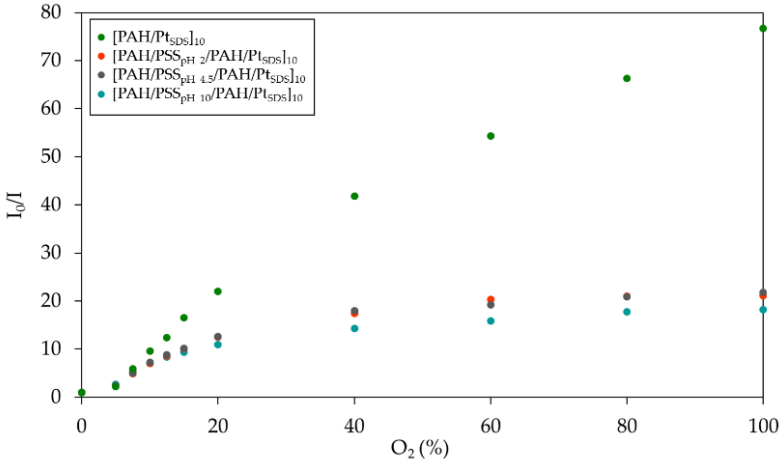

Figure 5.2. Calibration curves of $[PAH/Pt_{SDS}]_{10}$ and the different sensing structures utilizing PSS at different pH values.

The next attempt for increasing the sensitivity of the sensors was to change the architecture of the sensing structure, placing Pt-TFPP where PSS was, and viceversa. In that manner, the outermost layer of the sensor was made of PSS, and the first Pt-TFPP layer was spaced from the fiber core by a single PAH layer. Besides, a further modification was carried out on this structure: the two outermost layers of PAH and PSS were eliminated, so Pt-TFPP was present in the most external layer of the sensing film. The two new structures that were analyzed were the following ones:

- $[PAH/Pt_{SDS}/PAH/PSS]_{10}$
- $[PAH/Pt_{SDS}/PAH/PSS]_9$ + [PAH/ Pt_{SDS}]

As well as in the former study, $[PAH/Pt_{SDS}]_{10}$ was more sensitive to oxygen than the rest of the structures. Whereas the I_0/I_{100} ratio of $[PAH/Pt_{SDS}/PAH/PSS]_{10}$ was 13.67, when for the case of $[PAH/Pt_{SDS}/PAH/PSS]_9$ + [PAH/ Pt_{SDS}] it increased up to 28.22 because of the presence of Pt-TFPP in the outermost layer, which was the one that was in contact with the environment.

These results obtained when using PSS for increasing the spacing thickness between luminescent films could be explained by the ones achieved by Elzbieciak et al. [11]: when depositing by Layer-by-Layer an odd number of layers of a weak polycation at high pH (low ionization degree) and a strong polyanion the resulting films exhibited a low roughness, which is directly correlated with the porosity and the permeability of the coating.

5.3.2. Poly(acrylic acid) (PAA) as spacing material

Due to the unsatisfactory results obtained by utilizing PSS for increasing the spacing distance between the luminescent layers, it was substituted by PAA: it is an anionic and weak polyelectrolyte, so its surface charge density can be tailored by modifying the pH of the solution. At low pH values it is barely ionized, giving rise to thick layers. Thus, this parameter was fixed at 4.5, and the concentration utilized was 10 mM.

Initially, the following structures were compared:

- $[PAH/Pt_{SDS}]_5$
- $[PAH/Pt_{SDS}/PAH/PAA]_4$ + $[PAH/Pt_{SDS}]$

The choice of this second structure was made in agreement with the following criteria:

- In both schemes, a single layer of PAH separated the first layer of Pt-TFPP from the fiber core.
- The outermost layer (that which is in contact with the environment) was made of Pt-TFPP.
- Both structures contained the same number of sensitive films.

Furthermore, it can be observed that the number of luminescent films was reduced from 10 to 5. This decision was taken because the main objective of this research was not to optimize the structure of ten layers, but to investigate, for a given number of luminescent films, the effect of increasing the spacing thickness between them. In order to obtain reasonable fabrication times, five luminescent layers were considered appropriate. Apart from that, the original optical set-up (without the HPF) was used again in order to obtain accurate calibration curves.

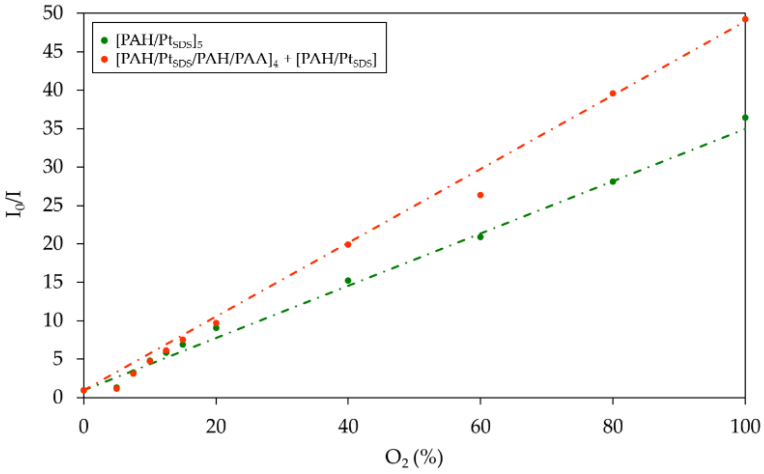

Figure 5.3. Calibration curves of $[PAH/Pt_{SDS}]_5$ and $[PAH/Pt_{SDS}/PAH/PAA]_4$ + $[PAH/Pt_{SDS}]$. The increase of the spacing distance between the luminescent layers gave rise to the increase of the sensitivity of the sensor.

Both sensors were exposed to different oxygen concentrations between 0% and 100%, and the obtained calibration curves are plotted in Figure 5.3: as it can be observed, when a layer of PAA was introduced between those of PAH, the sensitivity of the sensor increased. Furthermore, the calibration curve was linear, what meant that the distribution of the luminophore inside the sensing matrix was homogeneous.

5.3.3. Sensors construction process

Based on the previous results, it was decided to continue within this line of research for the polyelectrolytes PDDA and PEI as well. In addition, more complex spacing structures were also analyzed, which are explained below:

- Structure A: $[P(+)/Pt_{SDS}]_5$
- Structure B: $[P(+)/Pt_{SDS}/P(+)/PAA]_4 + [P(+)/Pt_{SDS}]$
- Structure C: $[P(+)/Pt_{SDS}/(P(+)/PAA)_2]_4 + [P(+)/Pt_{SDS}]$
- Structure D: $[P(+)/Pt_{SDS}/(P(+)/PAA)_3]_4 + [P(+)/Pt_{SDS}]$

where P(+) represents the corresponding polycation (PDDA, PEI or PAH). In this manner, the luminescent films (Pt_{SDS}) were spaced by different number of polyelectrolyte layers: one (Structure A), three (Structure B), five (Structure C) or seven (Structure D). A schematic representation of each sensing structure is plotted in Figure 5.4.

These sensing structures were deposited by the LbL technique onto the tip of 1000 μm-core plastic optical fiber (POF), which was activated by the process described by Bulmuş et al. [12]: it was first immersed in NaOH 10% (w/v), followed by another immersion in EtOH 50% (v/v), in both cases for 10 min. After that, the hydroxyl groups were generated by introducing the fiber for 20 min in a 10^{-3} mg/ml PVA solution. The fiber was washed for 1 min in ultrapure water after each step.

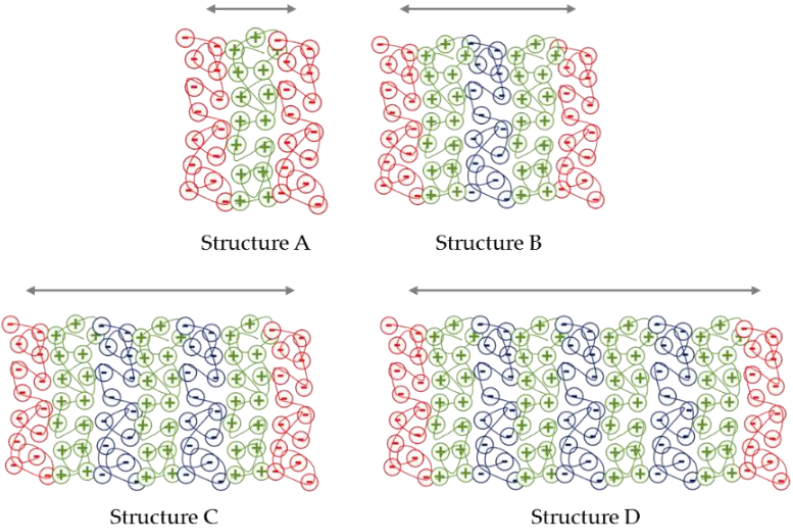

Figure 5.4. Scheme of the different thicknesses of spacing (in terms of number of layers) between the luminescent ones. Luminescent layers are red colored, polycationic ones (PDDA, PEI or PAH) are green colored, and the blue colored ones correspond to PAA.

For the fabrication of the simplest structure, $[P(+)/Pt_{SDS}]_5$, the fiber was alternatively immersed in the cationic and the anionic polyelectrolytes. In the cases of the more complex structures, different routines were followed:

- First, the fiber was immersed in the cationic solution, and then in the sensing one. Subsequently, it was alternatively immersed for N times (N = 1, 2, 3) in the polycationic and the PAA solutions, depending on the number of spacing layers. This process was repeated four times.

- Finally, the fiber was immersed in the polycationic and in the Pt-TFPP solution.

In this manner, all the sensing structures were made of five sensing layers. Furthermore, in every structure, the outermost layer consisted of

Pt-TFPP, the innermost luminescent film was spaced from the fiber core by a single cationic layer and all the sensitive films were spaced from each other by the same number of polyelectrolyte layers.

For the proper preservation of the sensors, they were stored in the absence of light at room conditions.

5.3.4. Comparison of the simplest sensing structures

The three sensors in which the luminescent films were spaced from each other by a single cationic layer were the first to be characterized. Thus, they were exposed to oxygen concentrations from 0% to 100%. The calibration curves were obtained by calculating the ratio between the relative intensity in the absence of O_2 (I_0) and the relative intensity for every oxygen concentration (I). The Stern-Volmer plots of every sensor are shown in Figure 5.5, and their mathematical models are summarized in Table 5.1.

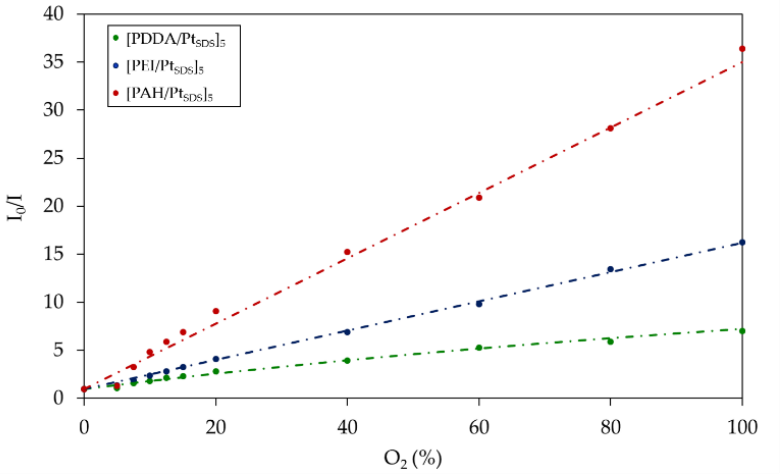

Figure 5.5. Calibration curves of the basic sensing structures: [PDDA/Pt$_{SDS}$]$_5$, [PEI/Pt$_{SDS}$]$_5$, and [PAH/Pt$_{SDS}$]$_5$.

Comparing the I_0/I_{100} ratios, the sensor made of PAH was the most sensitive (I_0/I_{100} = 35), whereas that built up with PDDA presented the lowest sensitivity (I_0/I_{100} = 5) and the one fabricated with PEI exhibited an intermediate behaviour (I_0/I_{100} = 16.2).

Sensor	Stern-Volmer equations
$[PDDA/Pt_{SDS}]_5$	$\frac{I_0}{I} = \left(\frac{0.957}{1 + 0.0898 \cdot [O_2]} + \frac{0.043}{1 + 0.0001 \cdot [O_2]}\right)^{-1}$
$[PEI/Pt_{SDS}]_5$	$\frac{I_0}{I} = \left(\frac{0.9939}{1 + 0.1526 \cdot [O_2]} + \frac{0.0061}{1 + 0.085 \cdot [O_2]}\right)^{-1}$
$[PAH/Pt_{SDS}]_5$	$\frac{I_0}{I} = 1 + 0.34 \cdot [O_2]$

Table 5.1. Calibration curves of the three sensors under study.

Besides, when paying attention to their mathematical models, the only one which was linear was that made of PAH, what meant that the luminophore distribution into the sensing matrix was homogeneous (f_2 = 0) [13]. In the other sensors, the luminescent particles were distributed in two different populations: in the case of PEI, the 99.39% of Pt-TFPP was affected by a quenching constant $K_{SV,1}$ = 0.1526, whereas the 0.61% was barely quenched by oxygen ($K_{SV,2}$ = 0.085). Attending to the calibration curve of PDDA, the 95.7% of the luminophore was quenched by oxygen and a non-negligible fraction of the population (4.3%) was not affected by its presence ($K_{SV,2}$ = 0.0001).

Related to the kinetics of the sensors, their response and recovery times were obtained by exposing them to cyclical variation of the oxygen concentration between 0% and 100%. The obtained results are shown in Table 5.2. The sensor made of PAH was the fastest (2.71 seconds) and that made of PDDA the slowest (5.76 seconds). In all the cases, the response times were shorter than the recovery ones, a typical behaviour of this kind of sensors. The baseline (intensity at 0% of oxygen) was recovered in all the cases.

Sensor	Response time (s)	Recovery time (s)
$[PDDA/Pt_{SDS}]_5$	5.76	12.87
$[PEI/Pt_{SDS}]_5$	3.37	9.91
$[PAH/Pt_{SDS}]_5$	2.71	14.95

Table 5.2. Response and recovery times of the three basic sensing structures.

This dissimilar behavior of the three sensors can be explained by the different morphological properties of the coatings [3], as it was explained in chapter 4: the rougher is the coating, the more sensitive and the faster is the sensor. In order to verify this assumption, these structures were deposited onto glass slides, and their roughness and thickness were measured by an AFM. The obtained results, which in fact are in agreement with the previous explanation, are presented in Table 5.3: in the case of the thinnest and less rough structure (the one that employed PDDA as polycationic counterpart) it exhibited the lowest sensitivity and the highest response time. Besides, the luminophore distribution into the polymeric matrix was also the most heterogeneous. Oppositely, PAH gave rise the thickest and the roughest structure, and the corresponding sensor was the most sensitive and the fastest. In addition, the luminophore was homogeneously distributed inside the matrix. As in all the cases explained up to now, the sensor built up with PEI showed an intermediate behavior, as well as intermediate morphological properties. The luminophore distribution inside the matrix was not homogeneous, but the amount of population that was hardly quenched by oxygen was smaller than in the case of PDDA (less than 1%).

Structure	Thickness (nm)	Roughness (nm)
$[PDDA/Pt_{SDS}]_5$	9.52	5.92
$[PEI/Pt_{SDS}]_5$	20.95	9.6
$[PAH/Pt_{SDS}]_5$	44	20.93

Table 5.3. Morphological properties of the basic sensing structures.

5.3.5. Effect of increasing the spacing distance between the luminescent layers for each cationic polyelectrolyte

The short distance between the luminophores is the cause of the self-quenching [14]. Monolayers of PDDA and PEI are thinner (1 nm [15] and 2 nm [16], respectively) than those of PAH (5 nm at pH 9 [17]). Thus, the spacing distance between luminescent layers is smaller in $[PDDA/Pt_{SDS}]_5$ and $[PEI/Pt_{SDS}]_5$ than in $[PAH/Pt_{SDS}]_5$, so they are supposed to be more affected by the self-quenching. Therefore, when increasing the number of layers spacing the luminescent ones, the increase of the sensitivity is expected to be higher in those sensors than in $[PAH/Pt_{SDS}]_5$. To carry out this analysis, the above explained Structures A, B, C and D were studied.

The first case under study was that when PDDA was the cationic polyelectrolyte. For that polycation, when the luminophore layers were spaced by a single layer of this polycation the sensor exhibited the lowest sensitivity: I_0/I_{100} = 7. When increasing the spacing distance by introducing a monolayer of PAA between the layers of PDDA, the I_0/I_{100} ratio increased up to 9.8. The maximum of the sensitivity was achieved when five layers of polyelectrolytes, i.e. $[(PDDA/PAA)_2/PDDA]$, separated the luminescent layers from each other, being the I_0/I_{100} ratio 16.2, threefold higher than that of the basic structure, $[PDDA/Pt_{SDS}]_5$. In the case of the greatest spacing distance, i.e. $[(PDDA/PAA)_3/PDDA]$, the sensitivity of the sensor decreased up to 14. The corresponding

calibration curves of these sensors are plotted in Figure 5.6: as it can be observed, as the spacing thickness between the luminescent layers increased, also did the sensitivity of the sensors until the optimal spacing distance was reached. Furthermore, once this optimal distance was exceeded, although the sensitivity decreased, the sensitivity was still higher than that of $[PDDA/Pt_{SDS}]_5$.

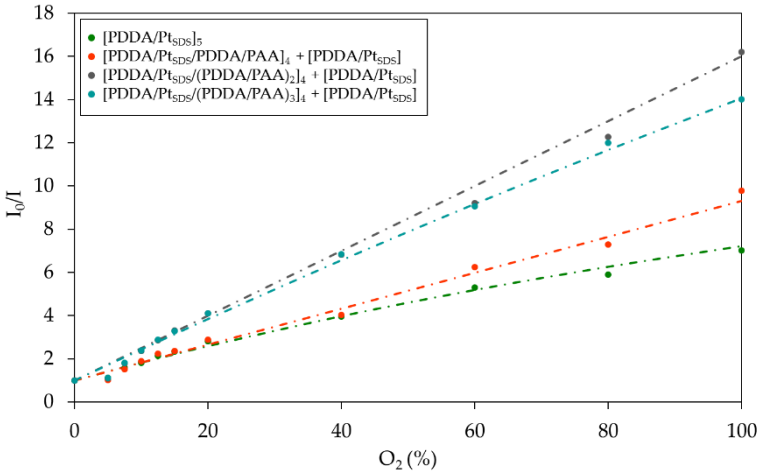

Figure 5.6. Calibration curves of the sensors fabricated employing PDDA as cationic polyelectrolyte.

The mathematical models of the calibration curves are summarized in Table 5.4.

Sensor	Stern-Volmer equations
$[PDDA/Pt_{SDS}]_5$	$\frac{I_0}{I} = \left(\frac{0.957}{1 + 0.0898 \cdot [O_2]} + \frac{0.043}{1 + 0.0001 \cdot [O_2]}\right)^{-1}$
$[PDDA/Pt_{SDS}/PDDA/PAA]_4$ + $[PDDA/Pt_{SDS}]$	$\frac{I_0}{I} = 1 + 0.0083 \cdot [O_2]$
$[PDDA/Pt_{SDS}/(PDDA/PAA)_2]_4$ + $[PDDA/Pt_{SDS}]$	$\frac{I_0}{I} = 1 + 0.15 \cdot [O_2]$
$[PDDA/Pt_{SDS}/(PDDA/PAA)_3]_4$ + $[PDDA/Pt_{SDS}]$	$\frac{I_0}{I} = \left(\frac{0.992}{1 + 0.147 \cdot [O_2]} + \frac{0.008}{1 + 0.0002 \cdot [O_2]}\right)^{-1}$

Table 5.4. Mathematical models of the sensors fabricated employing PDDA as cationic polyelectrolyte.

In the case of $[PDDA/Pt_{SDS}]_5$ the luminophore was distributed in two different environments with different quenching constants (the 95.7% of the population was affected by $K_{SV,1}$ = 0.0898 and the 4.3% of the total was barely quenched by oxygen ($K_{SV,2}$ = 0.0001). In consequence, as it can be observed in Figure 5.7(a), the luminescent peak was not completely quenched at 100% of oxygen, what meant that the luminophore distribution was heterogeneous [18]. By increasing the spacing distance, the luminophore population was distributed more homogeneously. For the spacing structure [PDDA/PAA/PDDA] the whole population was equally affected by oxygen (K_{SV} = 0.0083). A similar distribution of the luminophore was observed when the luminescent layers were spaced from each other by the structure $[(PDDA/PAA)_2/PDDA]$, when the sensor exhibited the highest sensitivity, being the quenching constant K_{SV} = 0.15. Besides, in both cases the intensity of the luminescent peak is close to 0 for completely oxygenated atmospheres (Figures 5.7(b) and (c)). Finally, for a greater spacing distance, the luminescent intensity was not completely quenched at 100% oxygen concentration (Figure 5.7(d)). Inside that sensing structure, the luminophore distribution was not totally homogeneous: whereas the quenching constant of the 99.2% of the population was $K_{SV,1}$ = 0.147, the 0.8% of the luminescent particles was hardly quenched by oxygen, $K_{SV,2}$ = 0.0002.

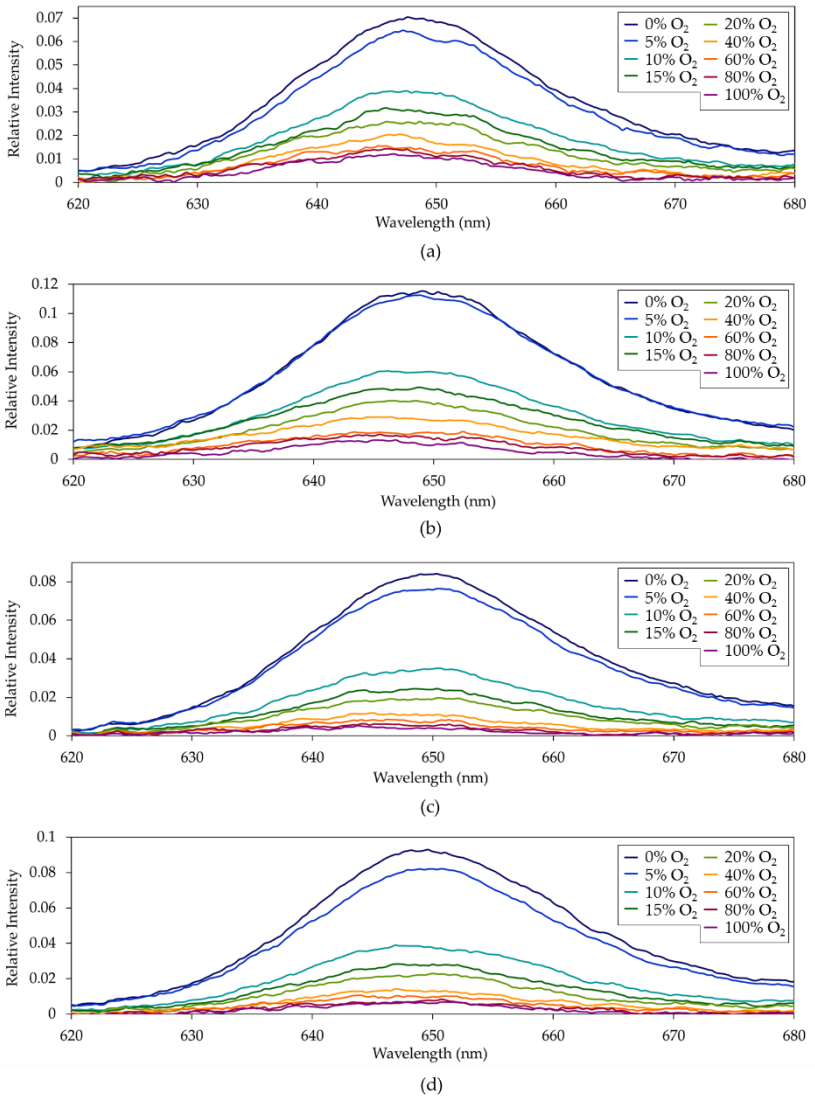

Figure 5.7. Relative intensity of the luminescent peak of the sensors made with PDDA at different oxygen concentrations. Each figure corresponds to a different number of spacing layers (N = 1 (A), N = 2 (B), N = 3 (C), N = 4 (D)) between the luminescent ones.

When employing PEI as the polycation, the highest sensitivity was achieved for the sensing structure [PEI/Pt_{SDS}/(PEI/PAA)$_2$]$_4$ + [PEI/Pt_{SDS}], in which the luminescent films were spaced from each other by five layers or polyelectrolytes. Its I_0/I_{100} ratio was 24.6, 1.52 times higher than the obtained with the simplest structure, [PEI/Pt_{SDS}]$_5$, whose I_0/I_{100} ratio was 16.2. Their calibration curves, as well as the ones corresponding to the rest of the sensors fabricated utilizing PEI as the cationic polyelectrolyte are displayed in Figure 5.8.

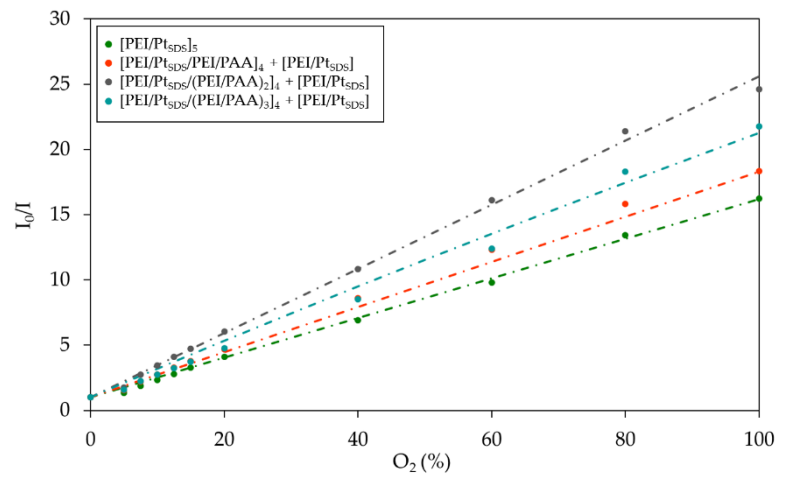

Figure 5.8. Calibration curves of the sensors fabricated employing PEI as cationic polyelectrolyte.

Besides, their mathematical models are summarized in Tables 5.5: the sensitivity and linearity of the sensors increased as the separation between the luminescent films did, until reaching the optimal. The relative luminescent intensities of the sensors for different oxygen concentrations are plotted in Figure 5.9: in all the cases, the relative luminescent intensities at 100% oxygen were close to 0, even for the sensors [PEI/Pt_{SDS}]$_5$ and [PEI/Pt_{SDS}/(PEI/PAA)$_3$]$_4$ + [PEI/Pt_{SDS}], in which the fraction of the hardly quenched luminophores was almost negligible (f_2 = 0.61% and 0.5%, respectively).

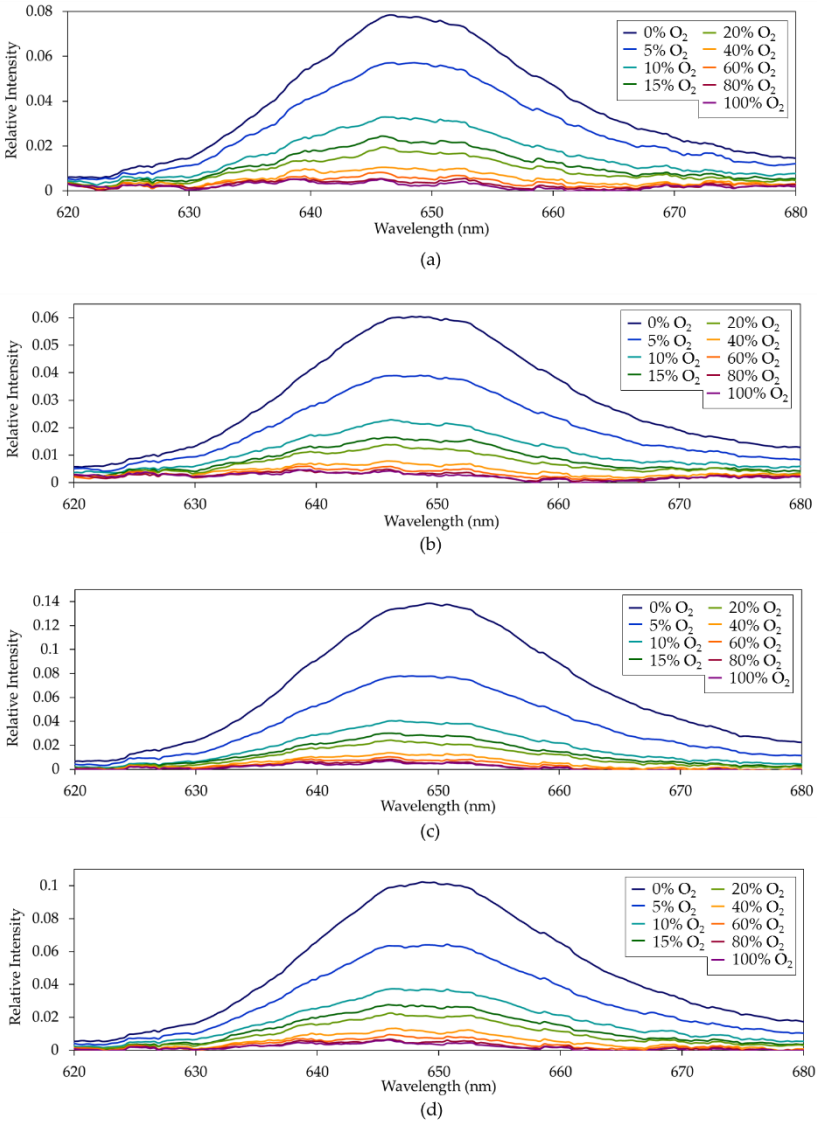

Figure 5.9. Relative intensity of the luminescent peak of the sensors made with PEI at different oxygen concentrations. Each figure corresponds to a different number of spacing layers (N = 1 (A), N = 2 (B), N = 3 (C), N = 4 (D)) between the luminescent ones.

Sensor	Stern-Volmer equations
$[PEI/Pt_{SDS}]_5$	$\frac{I_0}{I} = \left(\frac{0.9939}{1 + 0.1526 \cdot [O_2]} + \frac{0.0061}{1 + 0.085 \cdot [O_2]}\right)^{-1}$
$[PEI/Pt_{SDS}/PEI/PAA]_4$ + $[PEI/Pt_{SDS}]$	$\frac{I_0}{I} = 1 + 0.1737 \cdot [O_2]$
$[PEI/Pt_{SDS}/(PEI/PAA)_2]_4$ + $[PEI/Pt_{SDS}]$	$\frac{I_0}{I} = 1 + 0.246 \cdot [O_2]$
$[PEI/Pt_{SDS}/(PEI/PAA)_3]_4$ + $[PEI/Pt_{SDS}]$	$\frac{I_0}{I} = \left(\frac{0.995}{1 + 0.222 \cdot [O_2]} + \frac{0.005}{1 + 0.002 \cdot [O_2]}\right)^{-1}$

Table 5.5. Mathematical models of the sensors fabricated employing PEI as cationic polyelectrolyte.

The third polyelectrolyte utilized as cationic counterpart was PAH. As it was mentioned before, PAH is the cationic polyelectrolyte which forms thicker coatings. Therefore, it is expected that a lower number of layers is necessary to obtain the optimum spacing. In fact, the structure $[PAH/Pt_{SDS}/PAH/PAA]_4$ + $[PAH/Pt_{SDS}]$ exhibited the highest sensitivity, with an I_0/I_{100} ratio equal to 49.3, which was 1.35 times higher than that of the simplest structure, $[PAH/Pt_{SDS}]_5$. When the number of spacing layers was increased, both, the linearity and the sensitivity of the sensors decreased (see Figure 5.10): in the case of $[PAH/Pt_{SDS}/(PAH/PAA)_2]_4$ + $[PAH/Pt_{SDS}]$, I_0/I_{100} = 17.2 and for $[PAH/Pt_{SDS}/(PAH/PAA)_3]4$ + $[PAH/Pt_{SDS}]$, I_0/I_{100} = 9.6. The decrease of the linearity of the calibration curves as the number of spacing layers increased demonstrated the more heterogeneous distribution of the luminophore inside the sensing coatings [18], as it can be inferred from the quenching constants of the sensors and their mathematical models, which are presented in Tables 5.6. This fact can be also observed in the relative intensities of the luminescent peak of each sensor, shown in Figure 5.11(a)-(d). For instance, the luminescent intensity of the $[PAH/Pt_{SDS}/(PAH/PAA)_2]_4$ + $[PAH/Pt_{SDS}]$ sensor was not completely quenched for 100% oxygen: in that structure, whereas the 97.45% of the luminophore was affected by oxygen with a quenching constant $K_{SV,1}$ = 0.2516, the 2.55% of the population was almost unquenched ($K_{SV,2}$ = 0.0023). In the case of the

[PAH/Pt$_{SDS}$/(PAH/PAA)$_3$]$_4$ + [PAH/Pt$_{SDS}$] sensor, the luminescent peak in an oxygen-saturated atmosphere was clearly observable, what happened because the 28.19% of the population of Pt-TFPP was barely accessible for oxygen ($K_{SV,2}$ = 0.023).

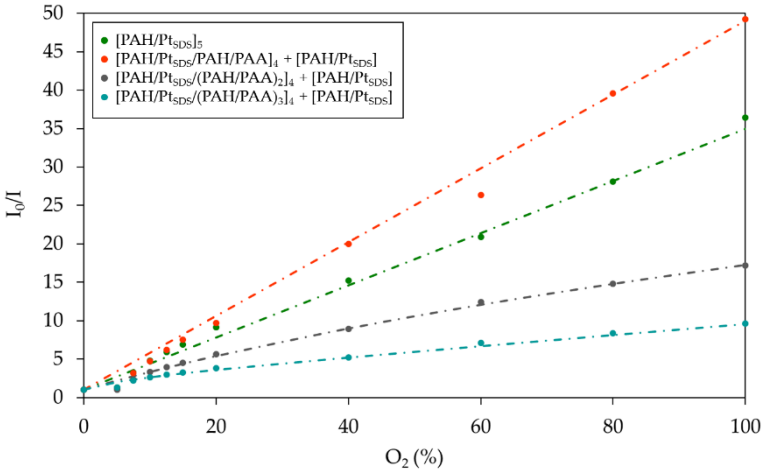

Figure 5.10. Calibration curves of the sensors fabricated employing PAH as cationic polyelectrolyte.

Sensor	Stern-Volmer equations
[PAH/Pt$_{SDS}$]$_5$	$\frac{I_0}{I} = 1 + 0.34 \cdot [O_2]$
[PAH/Pt$_{SDS}$/PAH/PAA]$_4$ + [PAH/Pt$_{SDS}$]	$\frac{I_0}{I} = 1 + 0.48 \cdot [O_2]$
[PAH/Pt$_{SDS}$/(PAH/PAA)$_2$]$_4$ + [PAH/Pt$_{SDS}$]	$\frac{I_0}{I} = \left(\frac{0.9745}{1 + 0.2516 \cdot [O_2]} + \frac{0.0255}{1 + 0.0023 \cdot [O_2]}\right)^{-1}$
[PAH/Pt$_{SDS}$/(PAH/PAA)$_3$]$_4$ + [PAH/Pt$_{SDS}$]	$\frac{I_0}{I} = \left(\frac{0.7182}{1 + 0.37 \cdot [O_2]} + \frac{0.2819}{1 + 0.023 \cdot [O_2]}\right)^{-1}$

Table 5.6. Mathematical models of the sensors fabricated employing PAH as cationic polyelectrolyte.

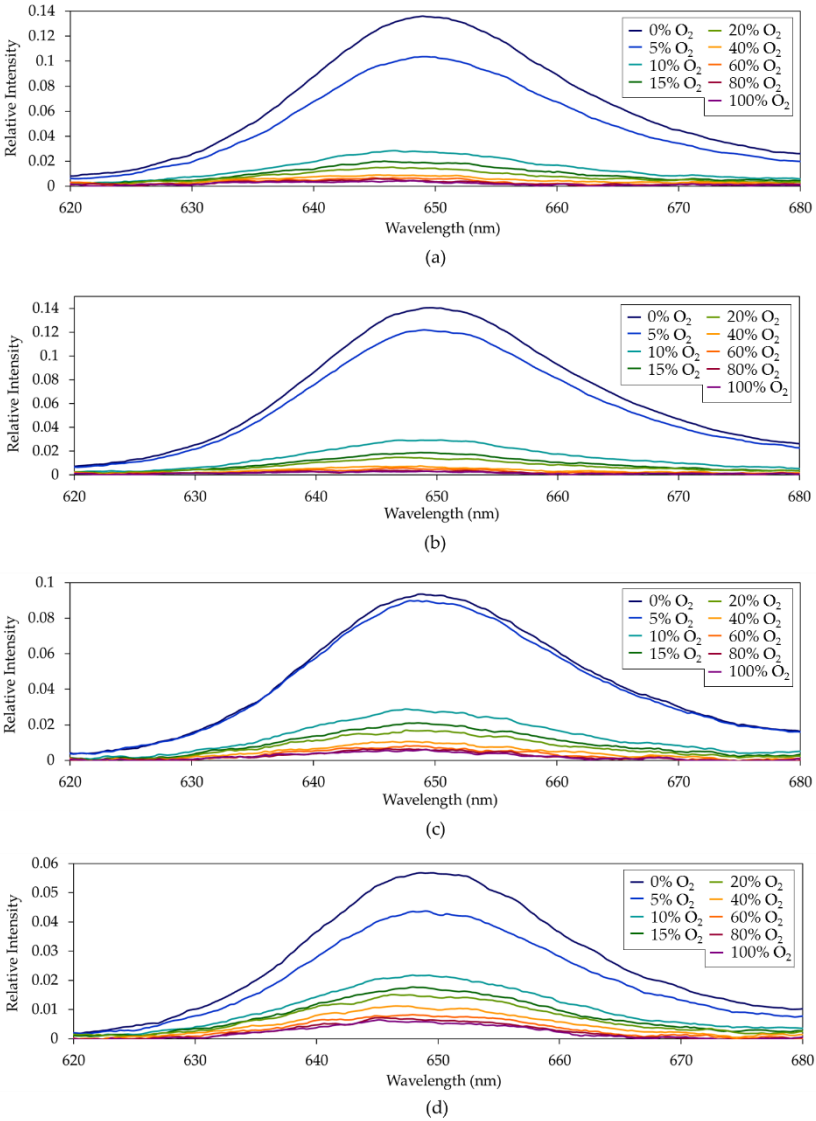

Figure 5.11. Relative intensity of the luminescent peak of the sensors made with PAH at different oxygen concentrations. Each figure corresponds to a different number of spacing layers (N = 1 (A), N = 2 (B), N = 3 (C), N = 4 (D)) between the luminescent ones.

Analyzing these results, it was observed that the sensing structures that were thicker than the optimal ones exhibited less linear calibration curves. According to the mathematical models proposed by Demas et al. [18], it can be considered that the luminophore was heterogeneously distributed into the sensing matrix (see Tables 5.4-5.9). This distribution of the sensing material affected the sensitivity of these structures: the luminophore of the innermost layers was less accessible to oxygen than that of the outermost ones. In consequence, even in completely oxygen saturated atmospheres, not all the population was quenched, what meant that the I_{100} value was not negligible. Therefore, the I_0/I_{100} ratio decreased and, hence, the sensitivity also decreased.

For each cationic polyelectrolyte, the kinetics of the four sensing structures were analyzed. To that end, each sensor was exposed to cyclical variations of the oxygen concentration from 0% to 100%. The calculated response and recovery times are shown in Tables 5.7 (PDDA), 5.8 (PEI) and 5.9 (PAH). For every case, the response times were shorter than the recovery ones, and they increased as the thickness of the sensing structures did.

Sensor	Response time (s)	Recovery time (s)
$[PDDA/Pt_{SDS}]_5$	5.76	12.87
$[PDDA/Pt_{SDS}/PDDA/PAA]_4$ + $[PDDA/Pt_{SDS}]$	5.24	13.24
$[PDDA/Pt_{SDS}/(PDDA/PAA)_2]_4$ + $[PDDA/Pt_{SDS}]$	5.74	11.91
$[PDDA/Pt_{SDS}/(PDDA/PAA)_3]_4$ + $[PDDA/Pt_{SDS}]$	9.47	12.21

Table 5.7. Response and recovery times of the sensors made with PDDA as polycation.

Sensor	Response time (s)	Recovery time (s)
$[PEI/Pt_{SDS}]_5$	3.37	9.91
$[PEI/Pt_{SDS}/PEI/PAA]_4$ + $[PDDA/Pt_{SDS}]$	3.79	12.99
$[PEI/Pt_{SDS}/(PEI/PAA)_2]_4$ + $[PEI/Pt_{SDS}]$	5.15	11.35
$[PEI/Pt_{SDS}/(PEI/PAA)_3]_4$ + $[PEI/Pt_{SDS}]$	4.65	9.32

Table 5.8. Response and recovery times of the sensors made with PEI as polycation.

Sensor	Response time (s)	Recovery time (s)
$[PAH/Pt_{SDS}]_5$	2.71	14.95
$[PAH/Pt_{SDS}/PAH/PAA]_4$ + $[PAH/Pt_{SDS}]$	5	13.95
$[PAH/Pt_{SDS}/(PAH/PAA)_2]_4$ + $[PAH/Pt_{SDS}]$	6.78	16.15
$[PAH/Pt_{SDS}/(PAH/PAA)_3]_4$ + $[PAH/Pt_{SDS}]$	12.16	24.75

Table 5.9. Response and recovery times of the sensors made with PAH as polycation.

5.3.5.1. Comparison between the optimal sensing structures for each cationic polyelectrolyte

The morphological properties of the optimal sensors for each cationic polyelectrolyte were analyzed with an AFM. The measure values of the roughness and thickness of the structures are shown in Table 5.10: in every case, the values were higher than those of the simplest structures, $[P(+)/Pt_{SDS}]_5$, which have been previously displayed in Table 5.3.

Structure	Roughness (nm)	Thickness (nm)
$[PDDA/Pt_{SDS}/(PDDA/PAA)_2]_4$ + $[PDDA/Pt_{SDS}]$	13.18	37.59
$[PEI/Pt_{SDS}/(PEI/PAA)_2]_4$ + $[PEI/Pt_{SDS}]$	19.45	61.8
$[PAH/Pt_{SDS}/PAH/PAA]_4$ + $[PAH/Pt_{SDS}]$	45.57	146.84

Table 5.10. Morphological features of the optimal sensing structures for each cationic polyelectrolyte.

First, it can be observed that the sensor that exhibited the highest sensitivity, $[PAH/Pt_{SDS}/PAH/PAA]_4 + [PAH/Pt_{SDS}]$, is the one that showed the highest values for the roughness and the thickness. Oppositely, the least sensitive sensor, which used PDDA as cationic polyelectrolyte, exhibited the lowest values for the roughness and the thickness [3].

Besides, when comparing the enhancement of the sensitivity between the optimal structure and the basic one for each polycation (measured as the ratio of the I_0/I_{100} ratios of the optimal and simplest structure), the one that corresponded to PDDA was the highest. In particular, the I_0/I_{100} ratio of $[PDDA/Pt_{SDS}/(PDDA/PAA)_2]_4 + [PDDA/Pt_{SDS}]$ was 2.3 times higher than that of $[PDDA/Pt_{SDS}]_5$. Meanwhile, for the optimal number of spacing layers for the other cationic polyelectrolytes, PEI and PAH, the enhancements of the sensitivity were 1.5 and 1.35, respectively.

According to this data, due to the low thickness of the monolayers of PDDA, the [PAH/Pt_{SDS}]$_5$ sensor was the most affected by self-quenching. By increasing the spacing distance between the luminescent layers, this effect was attenuated. Furthermore, the increases of that spacing distance also led to a more homogeneous distribution of the luminophore inside the sensing matrix, what led to more linear calibration curves.

Comparing their kinetics, the three sensors exhibited similar response (between 5 and 6 seconds) and recovery times (between 11 and 14 seconds). Furthermore, all the sensors recovered the baseline (normalized intensity in the absence of oxygen) after oxygen concentration variation from 0% to 100%, as it can be observed in Figure 5. 12, as well as in the detailed images of the response times and recovery times that are depicted in Figure 5.13:

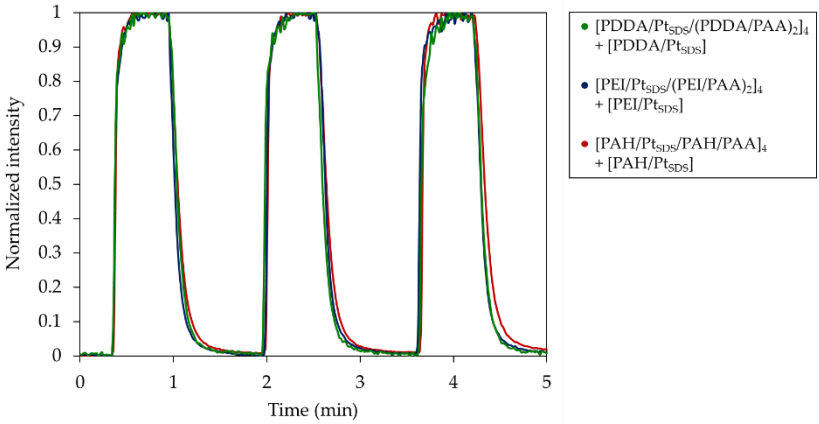

Figure 5.12. Response and recovery times of the optimal sensing structures for each cationic polyelectrolyte: PDDA, PEI and PAH.

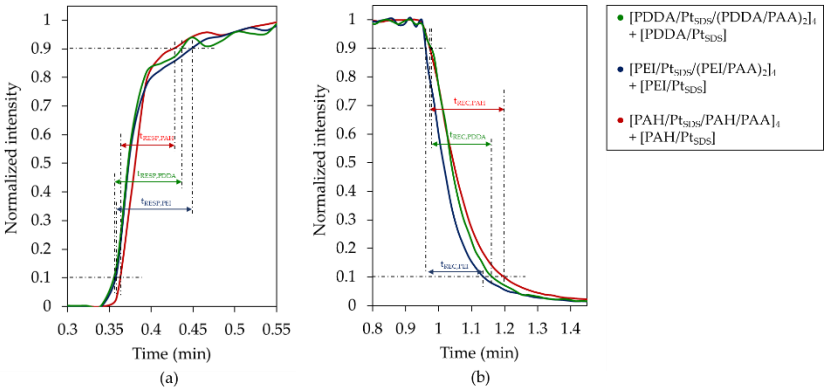

Figure 5.13. (a) Response and (b) recovery times of the optimal sensing structures for each cationic polyelectrolyte: PDDA, PEI and PAH.

5.4. Conclusions

In this chapter, the effect of increasing the spacing distance between the luminophore layers has been studied for three different sensing structures, which were fabricated by means of the LbL technique, but with different cationic polyelectrolytes: PDDA, PEI and PAH. First, it was checked that the optimal number of spacing layers depended on the thickness of the monolayers of PDDA, PEI and PAH: the thinner these monolayers were, the higher was the number of the spacing layers needed. The thickness of these monolayers was not enough to attenuate the self-quenching, which was more noticeable for the sensors fabricated with PDDA than for those made up with PEI or PAH. In consequence, the enhancement of the sensitivity that was obtained by increasing the spacing distance between the luminescent films was higher for the case of utilizing PDDA than when using PEI or PAH. Besides, tailoring the separation between the luminophore layers not only permitted to increase the sensitivity of the sensors, but also to tune the distribution of the luminescent material inside the sensing matrix. Finally, and in agreement with the results obtained in the previous chapter, the highest sensitivity was reached by the sensor which exhibited the highest roughness. In light of these results, the LbL has been demonstrated as a powerful technique for fabricating luminescence-based sensors, in which not only the self-quenching can be attenuated, but the sensitivity and the linearity of the calibration curves (i.e., the distribution of the luminophore inside the matrix) can also be optimized.

Bibliography

1. Patterson, G. H.; Piston, D. W. Photobleaching in Two-Photon Excitation Microscopy. *Biophysical Journal* **2000**, *78*, 2159–2162, doi:10.1016/S0006-3495(00)76762-2.
2. Ling, L.; Jiang, Y.; Wang, C.; Fang, X.; Wan, L.; He, Z.; Bai, C.; Chen, D. Delaying photobleaching and recovering luminescence of a DNA molecular light switch in DNA analysis. *Analytical Biochemistry* **2004**, *329*, doi:10.1016/j.ab.2004.02.046.
3. de Acha, N.; Elosúa, C.; Martínez, D.; Hernáez, M.; Matías, I. R.; Arregui, F. J. Comparative study of polymeric matrices embedding oxygen-sensitive fluorophores by means of Layer-by-Layer nanosassembly. *Sensors and Actuators, B: Chemical* **2017**, *239*, doi:10.1016/j.snb.2016.08.077.
4. Lee, S. K.; Okura, I. Photostable Optical Oxygen Sensing Material: Platinum Tetrakis(pentafluorophenyl)porphyrin Immobilized in Polystyrene. **1997**, *34*, 185–188.
5. Hamann, S.; Kiilgaard, J. F.; Litman, T.; Alvarez-Leefmans, F. J.; Winther, B. R.; Zeuthen, T. Measurement of Cell Volume Changes by Fluorescence Self-Quenching. In; 2002; Vol. 12, pp. 139–145.
6. Lakowicz, J. R. *Principles of Fluorescence Spectroscopy*; Lakowicz, J. R., Ed.; Springer US: Boston, MA, 2006; ISBN 978-0-387-31278-1.
7. Penfold, J.; Tucker, I.; Thomas, R. K.; Zhang, J. Adsorption of polyelectrolyte/surfactant mixtures at the air-solution interface: poly(ethyleneimine)/sodium dodecyl sulfate. *Langmuir : the ACS journal of surfaces and colloids* **2005**, *21*, 10061–73, doi:10.1021/la0505014.
8. Choi, J.; Rubner, M. F. Influence of the degree of ionization on weak polyelectrolyte multilayer assembly. *Macromolecules* **2005**, *38*, 116–124, doi:10.1021/ma048596o.
9. Balastre, M.; Persello, J.; Foissy, A.; Argillier, J.-F. Binding and Ion-Exchange Analysis in the Process of Adsorption of Anionic Polyelectrolytes on Barium Sulfate. *Journal of Colloid and Interface Science* **1999**, *219*, 155–162, doi:https://doi.org/10.1006/jcis.1999.6469.
10. Dejeu, J.; Buisson, L.; Guth, M. C.; Roidor, C.; Membrey, F.; Charraut, D.; Foissy, A. Early steps of the film growth mechanism in self-assembled multilayers of PAH and PSS on silica. Polymer uptake, charge balance and AFM analysis. *Colloids and Surfaces A: Physicochemical and Engineering Aspects* **2006**, *288*, 26–35, doi:10.1016/j.colsurfa.2006.03.050.
11. Elzbieciak, M.; Zapotoczny, S.; Nowak, P.; Krastev, R.; Nowakowska, M.; Warszyński, P. Influence of pH on the structure of multilayer films composed of strong and weak polyelectrolytes. *Langmuir* **2009**, *25*, 3255–3259, doi:10.1021/la803988k.
12. Bulmuş, V.; Ayhan, H.; Pişkin, E. Modified PMMA monosize microbeads for glucose oxidase immobilization. *Chemical Engineering Journal* **1997**, *65*, 71–76, doi:10.1016/S1385-8947(96)03156-7.
13. Carraway, E. R.; Demas, J. N.; DeGraff, B. A. Luminescence quenching mechanism for microheterogeneous systems. *Analytical Chemistry* **1991**, *63*.

14. Ogawa, M.; Kosaka, N.; Choyke, P. L.; Kobayashi, H. H-type dimer formation of fluorophores: A mechanism for activatable, in vivo optical molecular imaging. **2009**, *4*, 535–546, doi:10.1021/cb900089j.
15. Lvov, Y.; Möhwald, H. Protein architecture; interfacing molecular assemblies and immobilization biotechnology 2000.
16. Zhang, X.; Taylor, D.; Thomas, R.; Penfold, J.; Tucker, I. Modifying the adsorption properties of anionic surfactants onto hydrophilic silica using the pH dependence of the polyelectrolytes PEI, ethoxylated PEI, and polyamines. *Langmuir : the ACS journal of surfaces and colloids* **2011**, *27*, 3569–77, doi:10.1021/la1046723.
17. Shiratori, S. S.; Rubner, M. F. pH-dependent thickness behavior of sequentially adsorbed layers of weak polyelectrolytes. *Macromolecules* **2000**, *33*, 4213–4219, doi:10.1021/ma991645q.
18. Carraway, E. R.; Demas, J. N.; DeGraff, B. A.; Bacon, J. R. Photophysics and photochemistry of oxygen sensors based on luminescent transition-metal complexes. *Analytical Chemistry* **1991**, *63*, 337–342.

Chapter 6

Conclusions

After the analysis of the state of the art of optical sensors fabricated by LbL that utilize luminescence quenching as the detection mechanism, it was observed that there was a lack of gaseous oxygen sensors that combined both techniques, luminescence quenching and LbL. Furthermore, rigorously speaking, the cases reported in the literature did not employ the LbL technique to deposit the sensitive indicator: in those cases, the embedding matrix is indeed built by means of LbL and then the final matrix was immersed only once in a solution just to adsorb the indicator. Therefore, it has been considered of great interest a detailed research about luminescence-based oxygen sensors, in which the sensitive indicator could be entrapped in a controlled way inside polymeric matrices by LbL.

Owing to its interesting chemical and optical features, the platinum metalloporphyrin Pt-TFPP was chosen as the appropriate oxygen indicator under study. Its main drawback for being deposited by means of the LbL approach was its water-insolubility: as the LbL is a wet technique, it requires all the materials to be dissolved in water solutions.

Thus, Chapter 3 is focused on overcoming this challenge, which was achieved thanks to the utilization of anionic micelles of SDS for entrapping Pt-TFPP. These micelles attenuated the aggregation and further precipitation of this sensing material. This fact, together with the use of PAH as the cationic counterpart, permitted the deposition of Pt-TFPP by LbL for the first time, as it was demonstrated by the EDX analysis and by the absorbance spectrum of the as-coated glass slides, as well. The sensor fabricated by depositing the structure $[PAH/Pt_{SDS}]_{10}$ on the tip of a 400 μm-core fiber was capable to distinguish oxygen concentrations from 0% to 100% and it also exhibited a repetitive behavior towards dynamic variations of the oxygen concentration. Once the LbL assembly of one the best known oxygen indicators (despite its water-insolubility) was achieved for the first time in this chapter, since LbL permits to fine-tune the properties of nanostructured films, it was considered of great interest to analyze how different polymeric matrices influence the performance of luminescent sensors.

In Chapter 4, previously to the analysis of the influence of the embedding matrices on the performance of the sensors, the diameters of the fiber cores (the one of the bifurcated fiber and that of the fiber onto which the sensor was built) were optimized. This fact permitted a better coupling of light, which implied an increase of the captured intensity of light and a decrease of the background noise, with the subsequent increment of the signal to noise ratio. Employing this optical set-up, the following study was carried out: three different cationic polyelectrolytes, PDDA, PEI and PAH, were utilized to fabricate the oxygen sensors. The hydrophilicity or hydrophobicity and the morphological properties (roughness and thickness) of the obtained nanostructures, $[PDDA/Pt_{SDS}]_{10}$, $[PEI/Pt_{SDS}]_{10}$ and $[PAH/Pt_{SDS}]_{10}$, as well as their sensitivities and kinetics towards oxygen variations were studied. The analysis of the features of the nanostructures demonstrated $[PDDA/Pt_{SDS}]_{10}$ as the thinnest, the less rough and the most hydrophilic one. $[PAH/Pt_{SDS}]_{10}$ exhibited opposite properties: it was the thickest, the roughest and the most hydrophilic one. Meanwhile, $[PEI/Pt_{SDS}]_{10}$ had intermediate properties: in terms of morphology, although it was thicker and rougher than $[PDDA/Pt_{SDS}]_{10}$, the values of these parameters were

closer to those of this structure than to those of $[PAH/Pt_{SDS}]_{10}$. In the case of its hydrophobicity, the contact angle of $[PEI/Pt_{SDS}]_{10}$ was similar to that of $[PAH/Pt_{SDS}]_{10}$. Additionally, the exposure of the three sensors towards different oxygen concentrations from 0% to 100% revealed that the $[PDDA/Pt_{SDS}]_{10}$ structure was the less sensitive one. Meanwhile, $[PAH/Pt_{SDS}]_{10}$ exhibited the highest sensitivity and $[PEI/Pt_{SDS}]_{10}$ showed an intermediate one. Regarding to the kinetics, $[PDDA/Pt_{SDS}]_{10}$ had the longest response and recovery times, whereas $[PAH/Pt_{SDS}]_{10}$ was the fastest sensor. From that analysis, it was found that, on one side, there was a correlation between the morphology and the sensitivity of these sensors: the rougher the film, the higher its sensitivity. Additionally, a thicker coating gave rise to a more homogeneous distribution of the indicator, as it was demonstrated by the calibration curves and the analysis of the Stern-Volmer constants. The enhancement of sensitivity is attributed in part to the thickness of the cationic layers: the thicker they were, the higher was the spacing distance between the luminescent films and, thus, the lower was the self-quenching. However, this hypothesis was not demonstrated in this chapter. On the other side, the roughness of the coatings, what implies a higher porosity, it seems to play a more important role on the kinetics of the sensors than their morphologies: the $[PAH/Pt_{SDS}]_{10}$ sensor (the roughest coating) exhibited the fastest kinetics, and the $[PDDA/Pt_{SDS}]_{10}$ sensor (the lest rough coating), the slowest ones.

Additionally, as the $[PAH/Pt_{SDS}]_{10}$ sensor exhibited the highest sensitivity and the fastest kinetics, it was tried to be optimized by tailoring the pH of the PAH solutions. This analysis highlighted the critical role that that parameter plays in the fabrication of nanostructures by LbL and demonstrated again the dependency of the performance of luminescent sensors on the embedding matrix.

The previously exposed theory about the relationship between the spacing distance between the luminescent layers and the self-quenching suffered by the sensors was analyzed in Chapter 5: in that section, for each employed polycation (PDDA, PEI and PAH), different spacing thicknesses were introduced between the luminescent layers with the aim of avoiding the self-quenching: as that spacing distance increased, also

did the sensitivities of the sensors until the optimal separation was reached. Furthermore, the optimal sensing structure obtained for each polycation exhibited a linear calibration curve, what implied a homogeneous distribution of the indicator inside the polymeric matrix. Additionally, the values of the Stern-Volmer constants suggest that higher spacing distances than the optimal ones gave rise to heterogeneous distributions of the indicator inside the matrices, what would explain the decrease of the sensitivities of the sensors. These results demonstrated the LbL as a powerful approach to fine-tune the distribution of the indicator inside the matrix and, in consequence, the sensitivity of luminescence based sensors.

Just to conclude, the deposition by LbL of a water-insoluble porphyrin has opened the door for the fabrication of sensing devices that require the utilization of other water-insoluble indicators. As it has been demonstrated, the LbL technique offers the possibility to use different polymeric matrices and to tailor their deposition parameters, giving rise to the manufacture of optimized luminescence-based sensors.

Appendix I

Luminescent and colorimetric optical fiber sensor based on a Pt_2Pb cluster for the detection of volatile organic compounds

This section is devoted to the development of a volatile organic compounds (VOCs) sensor based on an organometallic Pt_2Pb cluster, which shows a luminescent emission and absorbance spectra that vary in presence of certain VOCs. This sensing material was entrapped into a polymeric matrix and deposited onto an optical fiber by dip-coating. When it was illuminated with a LED at 380nm, it showed a luminescent peak at 580 nm which was quenched and shifted towards lower wavelengths in the presence of acetone. In the case of the absorbance spectrum, a color change from orange to green was observable when it was exposed to acetone and methanol vapors.[1]

[1] This work was carried out with the major support from Prof. M. Teresa Moreno García, Prof. Jesús Berenguer and Prof. Elena Lalinde from the University of La Rioja, who synthesized and provided the sensing material employed in this study.

I.1. Introduction

This thesis is focused on the development and study of luminescence-based sensors for oxygen monitoring fabricated by means of the LbL technique. However, there are other chemicals, such as Volatile Organic Compounds (VOCs), whose detection is of high interest due to its wide range of applications: air and water-quality [1][2][3] or growth processes of plants monitoring [4], public safety [5] or early diagnosis of human diseases [6][7], among others. Therefore, in this section, the experiments carried out to develop luminescence- and colorimetry-based sensors for VOCs detection are explained. Besides, in order to study new polymeric matrices as well as a new deposition method, all of them were fabricated by using the dip-coating technique.

Among the existing optical techniques for VOCs identification, colorimetry [8][9] and luminescence [10] are the widely employed. Magnesium and Zinc porphyrins [11][12], and solvatochromic dyes such as Reichardt's dye [13] or Nile Red [14] have been widely utilized as sensing materials. These chemical dyes are usually embedded into polymeric [15][16] or sol-gel [17] matrices and changes in their optical properties due to the interaction with vapors are monitored.

In this work, the optical fiber technology and some of the above mentioned optical techniques have been combined for the fabrication of a VOC sensor. The sensing material is a novel organometallic Pt_2Pb cluster, whose formula is $[\{Pt(C_6F_5)(bzq)\}_2Pb(SpyCF_3\text{-}5)_2]$ (bzq = benzoquinolinyl, Spy = 2-pyridinethiolate). Its main advantage is that it can be characterized by two different techniques: colorimetry and luminescence [18].

I.2. Experimental considerations

I.2.1. Sensing material

The sensing material chosen for this investigation exhibits both, vapochromic and vapoluminescent behavior, [18]. It is an organometallic Pt_2Pb cluster, $[\{Pt(C_6F_5)(bzq)\}_2Pb(SpyCF_3\text{-}5)_2]$ (bzq = benzoquinolinyl, Spy = 2-pyridinethiolate), which was synthesized according to [18]. Its molecular structure is shown in Figure I.1. In presence of certain solvents both, its absorbance spectrum and its luminescent peak, centered at 580 nm, exhibit a blue shift, which can be attributed to changes in the environment of the Pb^{II} ion due to Pb-solvent bindings.

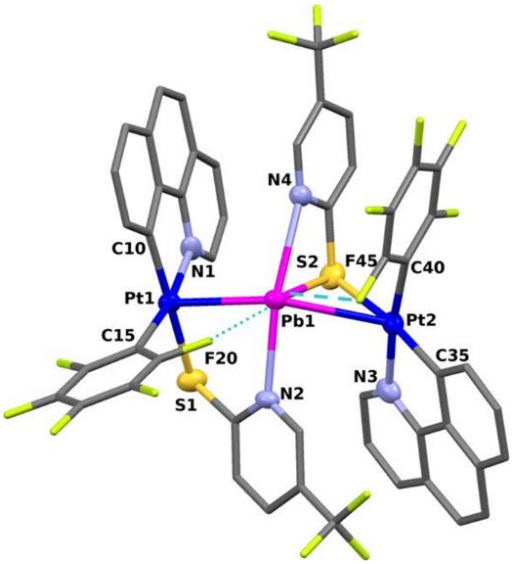

Figure I.1 Chemical structure of the Pt_2Pb cluster employed for the detection of VOCs.

I.2.2. Sensor construction process

For fabricating the sensor, this compound was entrapped into a polymeric matrix of poly(methyl methacrylate) (PMMA, Mw ~ 550000 g·mol-1) dissolved in acetone. PMMA was chosen because it had been widely employed for the fabrication of polymer-based sensors [19][20][21].

The sensing material concentration into the solution was 1 mM, and the ratio between it and PMMA was 1:9 (w/w). Firstly, the sensing compound was dissolved to 1 mL of acetone and, while stirring, PMMA was added progressively.

For its deposition, the dip-coating technique was utilized: the optical fiber was immersed at a constant speed of 20 mm/min into the sensing solution. Thereafter, the sensor was kept for 12 hours in the absence of light at room temperature in order to get the solvent evaporated. This construction process is shown in Figure I.2.

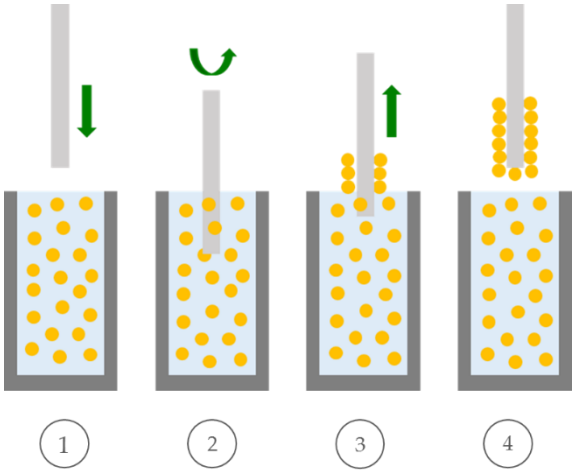

Figure I.2 Schematic illustration of the steps of the dip-coating technique: the optical fiber is immersed (1) in and extracted ((2) and (3)) from the sensing solution at a constant speed, and a uniform coating is deposited on its surface (4).

I.2.3. Experimental set-up

The reflection architecture was used to characterize the sensor. The experimental set-up is shown in Figure I.3: a halogen light source (DH-2000) and a LED centered at 380 nm were connected to each one of the independent branches of a 600-µm core bifurcated fiber. The common branch of that fiber was connected to the independent branch on another bifurcated fiber. In the common branch of that fiber was connected the sensor, and in the other independent one, it was connected a Maya LSL spectrometer from Ocean Optics Inc. Finally, the sensor was placed into a dark and hermetic chamber where the solvent to be detected were evaporated. In this manner, any external contamination from gases or light was avoided.

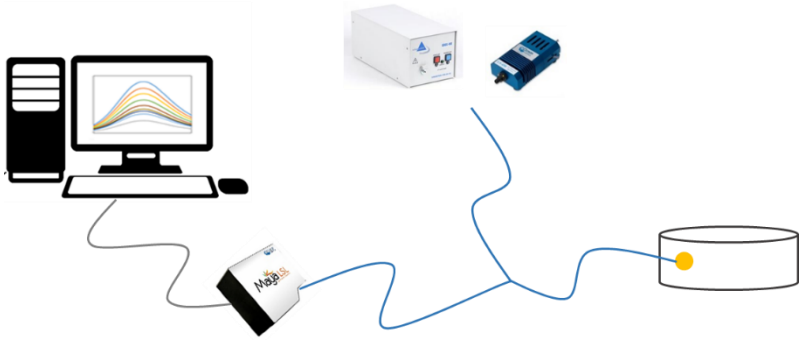

Figure I.3. Experimental set-up used for the characterization of the sensor.

I.3. Response towards methanol and acetone

I.3.1. Luminescent response

When illuminating the sensor at 380 nm, a luminescent emission was observed at 570 nm (Figure I.4): when the sensor was exposed to methanol no appreciable variation was registered. On the contrary, when exposed to acetone the luminescent emission was reversibly quenched, as it can be observed in Figure I.5. However, the sensor was not able to detect acetone concentration in the range of ppm. This behavior was likely to happen as a consequence of the crystallization of the Pt_2Pb compound inside the polymeric embedding matrix. This crystallized from did not allow the compound to interact with the VOCs present in the atmosphere.

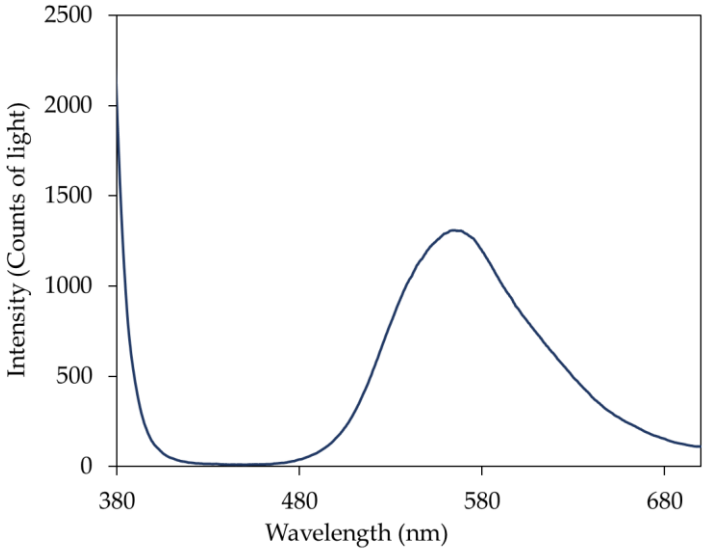

Figure I.4. Luminescent emission of the sensor fabricated with the Pt_2Pb cluster when illuminated at 380 nm.

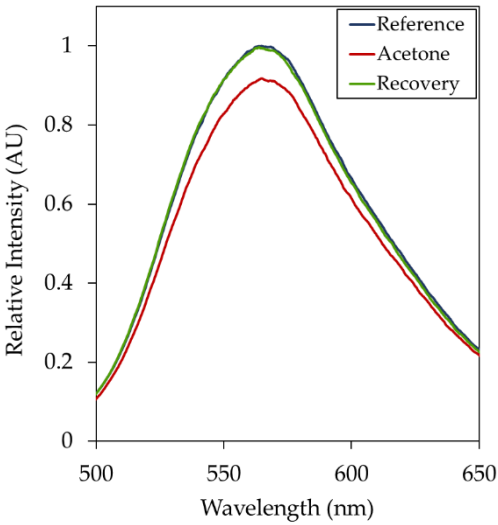

Figure I.5. Variation of the luminescent emission of the sensor when exposed to an acetone-saturated atmosphere.

I.3.2. Colorimetric response

In the case of colorimetry analysis, the sensor was illuminated with an halogen lamp and its absorbance spectra when exposed to VOCs were recorded. The spectrum of the sensing film deposited onto the optical fiber core in absence of VOCs, which is shown in Figure I.6 was taken as reference spectrum. Once the sensor was exposed to acetone, absorbance spectrum (Figure I.7) showed a minimum at 625 nm (orange) and maximums at 475 nm (blue) and 800 nm (red), which indicated a color change from orange towards green. When exposing the sensor to methanol, its absorbance spectrum showed a minimum at 615 nm (orange) and maxima at 440 nm (blue) and 780 nm (red), indicating a color change from orange towards green. In both cases, once the VOCs were removed, absorbance spectra shapes were similar to the original, what meant that the color change was reversible. However, the sensor was not able to detect lower acetone or methanol concentrations.

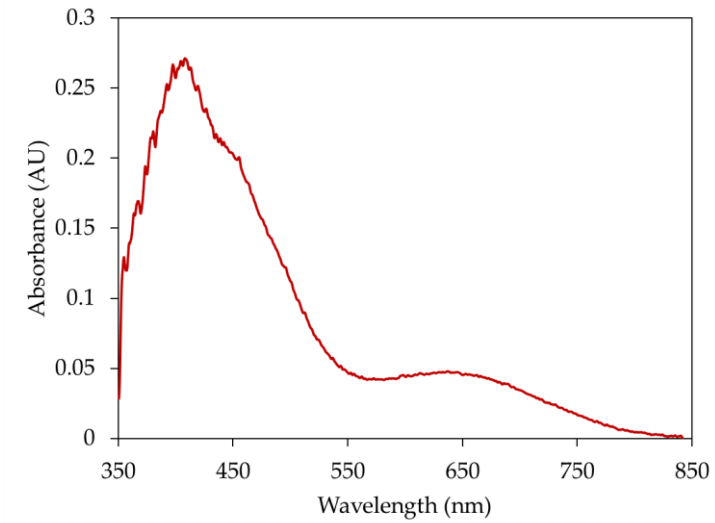

Figure I.6. Variation of the luminescent emission of the sensor when exposed to an acetone-saturated atmosphere.

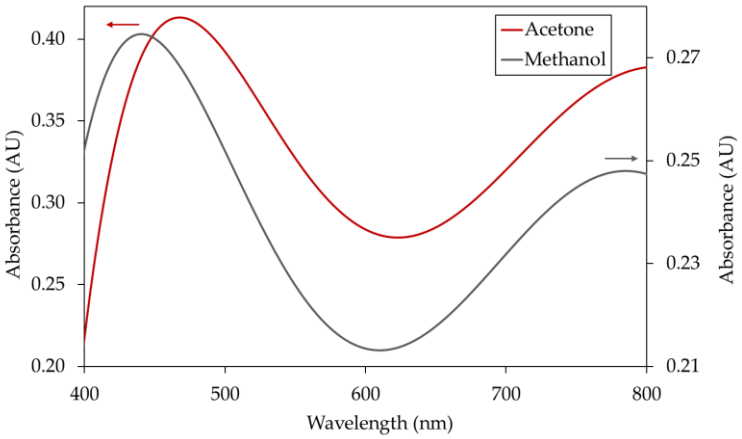

Figure I.7. Variation of the luminescent emission of the sensor when exposed to an acetone-saturated atmosphere.

I.4. Study of different embedding matrices

As the embedding matrices plays a key role in the response of this kind of sensors, different polymers and solvents were analysed in order to achieve a sensor capable to detect low concentrations of both VOCs. Although this goal was not reached because of the inability of the crystallized form of the compound to interact with the VOCs, it has been considered of interest to summarize in Table I.1 all the combinations of polymers and solvents that were studied, as well as the different analyzed ratios Pt_2Pb:polymer (w/w) .

Polymer	Solvent	Pt_2Pb:polymer (w/w)
PMMA	Acetone	1:99, 10:90, 25:75, 40:60
PMMA	Dichloromethane	1:99, 10:90, 25:75, 40:60
PVC	THF	10:90, 25:75
PS	THF	1:99, 10:90
PBA	THF	1:99, 10:90

Table I.1. Different combinations of polymers and solvents that were employed for fabricating the embedding matrix. The Pt2Pb:polymer (w/w) ratios that were studied are also shown.

Moreover, a SEM image of one of the coatings was taken, which is shown in Figure I.8: it corresponds to the matrix made of PolymBlend A (PBA) (acquired from NanoMyp Inc.) dissolved in THF. As it can be observed, the matrix exhibited a good porosity, a key requirement for VOCs sensing purposes. Thus, the lack of sensitivity of this sensor is not attributable to the properties of the embedding matrix, but to the sensing compound.

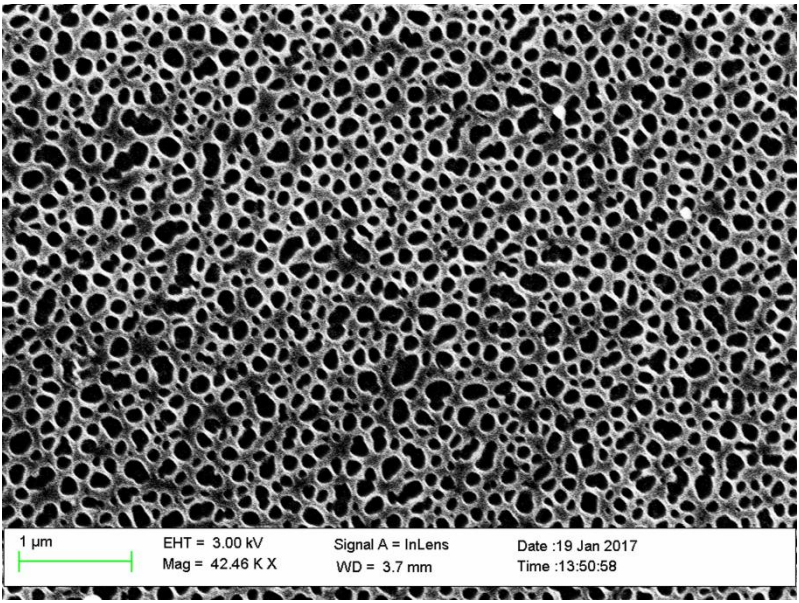

Figure I.8. Variation of the luminescent emission of the sensor when exposed to an acetone-saturated atmosphere.

I.5. Conclusions

The sensor built in this work was capable to detect saturated atmospheres of acetone and methanol. Whereas in the case of colorimetric analysis both compounds were detectable, when employing luminesce, only acetone was identified. Although several embedding matrices were tested, the crystallized form of the sensing compound inside them did not allow its interaction with VOCs and, thus, it was not possible to detect low concentrations. Furthermore, the analysis of different embedding matrices, as well as the SEM image of one of them, revealed that this sensing compound was not the appropriate one for the detection of VOCs with optical fiber sensors.

In any case, the high porosity exhibited by the matrix made of PBA makes it suitable for gas sensing purposes. Thus, it should be taken into account for the further development of this kind of sensors.

Bibliography

1. Peng, I. H.; Chu, Y. Y.; Kong, C. Y.; Su, Y. S. Implementation of indoor VOC air pollution monitoring system with sensor network. In; 2013; pp. 639–643.
2. Partridge, M.; Wong, R.; James, S. W.; Davis, F.; Higson, S. P. J.; Tatam, R. P. Long period grating based toluene sensor for use with water contamination. 2014, 203, 621–625, doi:10.1016/j.snb.2014.06.121.
3. Rowe, B. L.; Toccalino, P. L.; Moran, M. J.; Zogorski, J. S.; Price, C. V. Occurrence and potential human-health relevance of volatile organic compounds in drinking water from domestic wells in the United States. 2007, 115, 1539–1546, doi:10.1289/ehp.10253.
4. Aalto, J.; Kolari, P.; Hari, P.; Kerminen, V. M.; Schiestl-Aalto, P.; Aaltonen, H.; Levula, J.; Siivola, E.; Kulmala, M.; Bäck, J. New foliage growth is a significant, unaccounted source for volatiles in boreal evergreen forests. 2014, 11, 1331–1344, doi:10.5194/bg-11-1331-2014.
5. Castañeda, L.; Gonzalez-Alatriste, M.; Avendaño-Alejo, M. Thin solid films semiconducting metal oxide gas sensors: A brief review 2016, 14, 331–345.
6. Saalberg, Y.; Wolff, M. VOC breath biomarkers in lung cancer 2016, 459, 5–9.
7. Miekisch, W.; Schubert, J. K.; Noeldge-Schomburg, G. F. E. Diagnostic potential of breath analysis--focus on volatile organic compounds. Clinica chimica acta; international journal of clinical chemistry 2004, 347, 25–39, doi:10.1016/j.cccn.2004.04.023.
8. Yuan, H.; Yeom, S. H.; Lim, J. W.; Kang, S. W. Side-polished optical fiber odor sensor for VOC detection based on solvatochromism. In; 2011; Vol. 9, pp. 87–91.
9. Hoang, A. T.; Cho, Y. B.; Park, J.-S.; Yang, Y.; Kim, Y. S. Sensitive naked-eye detection of gaseous ammonia based on dye-impregnated nanoporous polyacrylonitrile mats. Sensors and Actuators B: Chemical 2016, 230, 250–259, doi:10.1016/j.snb.2016.02.058.
10. Strianese, M.; Pellecchia, C. Metal complexes as fluorescent probes for sensing biologically relevant gas molecules 2016, 318, 16–28.
11. Gutiérrez, A. F.; Brittle, S.; Richardson, T. H.; Dunbar, A. A proto-type sensor for volatile organic compounds based on magnesium porphyrin molecular films. 2014, 202, 854–860, doi:10.1016/j.snb.2014.05.082.
12. Kladsomboon, S.; Puntheeranurak, T.; Pratontep, S.; Kerdcharoen, T. An artificial nose based on M-porphyrin (M = Mg, Zn) thin film and optical spectroscopy. In; 2010; pp. 968–969.
13. Krech, J. H.; Rose-Pehrsson, S. L. Detection of volatile organic compounds in the vapor phase using solvatochromic dye-doped polymers. 1997, 341, 53–62, doi:10.1016/S0003-2670(96)00495-3.
14. Lee, J.-S.; Yoon, N.-R.; Kang, B.-H.; Lee, S.-W.; Gopalan, S.-A.; Jeong, H.-M.; Lee, S.-H.; Kwon, D.-H.; Kang, S.-W. Response characterization of a fiber optic sensor array with dye-coated planar waveguide for detection of volatile organic compounds. Sensors (Basel, Switzerland) 2014, 14, 11659–71, doi:10.3390/s140711659.
15. Hanisch, C.; Ni, N.; Kulkarni, A.; Zaporojtchenko, V.; Strunskus, T.; Faupel, F. Fast electrical response to volatile organic compounds of 2D Au nanoparticle layers embedded into polymers. Journal of Materials Science 2011.

16. Quercia, L.; Loffredo, F.; Alfano, B.; La Ferrara, V.; Di Francia, G. Fabrication and characterization of carbon nanoparticles for polymer based vapor sensors. Sensors and Actuators B: Chemical 2004, 100, 22–28, doi:10.1016/j.snb.2003.12.015.
17. Aguirre, S. M.; Hipatl, C. M.; Mixcóatl, J. C.; Pérez, G. B.; Merino, R. P.; Wetter, N. U.; Frejlich, J. Gas Sensor Using a Rhodamine-6 G Doped TiO[sub 2] Film Deposited on an Optical Fiber to Detect Volatile Organic Compounds. In AIP Conference Proceedings; AIP, 2008; Vol. 992, pp. 969–974.
18. Berenguer, J. R.; Lalinde, E.; Martín, A.; Moreno, M. T.; Ruiz, S.; Sánchez, S.; Shahsavari, H. R. Photophysical responses in Pt2Pb clusters driven by solvent interactions and structural changes in the Pb(II) environment. Inorganic chemistry 2014, 53, 8770–85, doi:10.1021/ic501458q.
19. Shiraishi, N.; Kimura, M.; Ando, Y. Development of PMMA-based gas sensor and its evaluation using a VOC dilution flow system. 2014, 119, 115–121, doi:10.1016/j.mee.2014.03.021.
20. Shiraishi, N.; Ikehara, T.; Dao, D. V.; Sugiyama, S.; Ando, Y. Fabrication and testing of polymer cantilevers for VOC sensors. 2013, 202, 233–239, doi:10.1016/j.sna.2013.01.011.
21. Chatterjee, S.; Castro, M.; Feller, J. F. An e-nose made of carbon nanotube based quantum resistive sensors for the detection of eighteen polar/nonpolar VOC biomarkers of lung cancer. 2013, 1, 4563–4575, doi:10.1039/c3tb20819b.

Appendix II

Detection of ethanol in human breath using optical fiber long period grating coated with metal-organic frameworks

In this section, an optical fiber sensor for ethanol detection in exhaled breath is described. The sensor was fabricated by functionalizing a Long Period Grating (LPG) with a metal-organic framework, ZIF-8. Although the sensor exhibited a high cross-sensitivity towards temperature and relative humidity, its response towards ethanol was repetitive: it was exposed to the exhaled breath of a person before and after the ingestion of alcoholic drinks, showing a higher wavelength difference between the resonance bands in the second case. Furthermore, despite the suitability of ZIF-8 for gas storage, typical CO_2 concentrations in human breath did not affect the sensor's response.[1]

[1] This work was carried out during a research stay in the Optics and Photonics Research Group from the University of Nottingham, under the supervision of Prof. Sergiy Korposh.

II.1. Introduction

As mentioned in Appendix I, the main goal of this thesis was to develop luminescence-based sensors. They were mainly devoted to oxygen monitoring, but VOCs measurements were also tried. In the last years, there has been an increasing interest in monitoring Volatile Organic Compounds (VOCs) in exhaled breath [1], since they can be used as indicators of different illnesses [2][3]; one of the most studied applications is ethanol detection in human breath, as it is of high interest in traffic safety [4].

Although a wide variety of electronic sensors, most of them based on semiconductor technology, is under development for VOCs detection [5], no device based on optical fiber has been developed for this purpose so far. With that aim, instead of luminescence, optical resonances induced by Long Period Gratings (LPGs) were investigated for ethanol measurements in human breath. Moreover, the sensors were fabricated by means of the in-situ crystallization technique, which had not been used in the rest of this thesis.

LPGs are devices based on periodic modifications of the refractive index of the fiber core that induce the coupling of the core mode to the co-propagating cladding ones [6]. This coupling is observable in the transmission spectrum as a series of attenuation bands, whose central wavelength also depends on external parameters, such as temperature, strain, bending or refractive index. When developing a sensor based on LPG, this structure must be functionalized with a coating that is sensitive to the target parameter [7]. In this particular case of ethanol monitoring, the sensing material used to coat the LPG is ZIF-8, a metal-organic framework that exhibits cavities for gas storage [8].

II.2. Theoretical considerations

A LPG is a periodic modification of the refractive index of the fiber core that gives rise to the coupling of the core mode to the co-propagating cladding modes [6]. Thus, different resonance bands can be observed in the transmission spectrum. The central wavelength of the resonance bands can be calculated according to equation:

$$\lambda_X = (n_{core} - n_{clad(X)})\Delta \qquad \text{(eq II.1)}$$

where λ_X is the wavelength at which light is coupled to the mode LP0X, n_{core} is the effective refractive index of the core mode, $n_{clad(X)}$ is the effective refractive index of the LP0X cladding mode and Δ is the period of the LPG. The central wavelength of the coupled modes also depends on external parameters, such as temperature [9], strain [10], bend radius [11] or the refractive index of the surrounding media [12]. This fact permits to use the LPGs as sensors of those variables. Furthermore, the particular feature of the sensitivity of a LPG to variations of the external refractive index opens the door to a wide variety of sensors based on this structure. For instance, by functionalizing it with a nanocoating whose properties change in the presence of a certain analyte, as it is the case of the metal-organic framework employed in this work.

In addition, the sensitivity of every cladding mode of a LPG is maximized when its phase matching turning point (PMTP) is reached [6]: at that point, the resonance band (centered at a single wavelength) is divided in two attenuation bands, each one centered at a different wavelength. Thus, the range of wavelengths that correspond to the PMTP of an LPG is the most attractive one for sensing purposes.

II.3. Experimental considerations

II.3.1. Fabrication of the Long Period Gratings

Using a custom-made amplitude mask, two different LPGs of grating periods of 109 and 109.5 μm and length of 30 mm were fabricated onto boron–germanium co-doped optical fiber (Fibercore PS750) with a cut-off wavelength 670 nm. The optical fibers were side-illuminated by the output from a frequency-quadrupled Nd:YAG laser operating at 266 nm [13].

II.3.2. Sensing material

Zeolitic Imidazolate Framework (ZIF-8) is a metal-organic framework made by zinc ions coordinated by four imidazolate rings. Thanks to its large cavities, gas molecules storage is allowed [8]. Besides, it is also well-known due to its chemical robustness and its thermal stability [14] and it has been used as sensitive material towards organic vapors [15]. Its chemical structure is shown in Figure II.1.

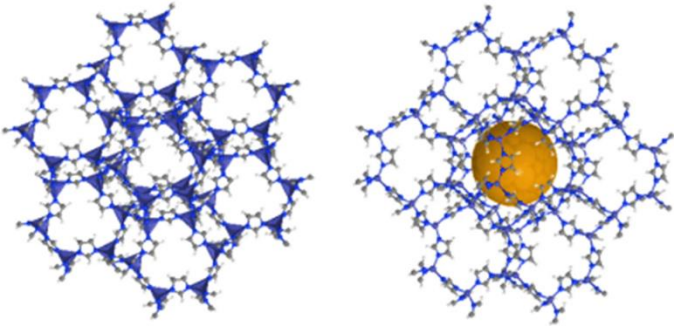

Figure II.1. Chemical structure of ZIF-8. The inner ball represents the cavity where the gas molecules are stored.

II.3.3. Experimental set-up

A transmission architecture was used to characterize the deposition of ZIF-8 onto the LPGs as well as the performance of both devices towards ethanol. Therefore, the LPG was illuminated by the halogen lamp HL2000 and the transmission spectra were recorded by the spectrometer USB4000. Besides, for the analysis of the behavior of the sensors towards ethanol, they were fixed inside a hermetic box with the aim of avoiding any gas leakage. This experimental set-up is shown in Figure II.2.

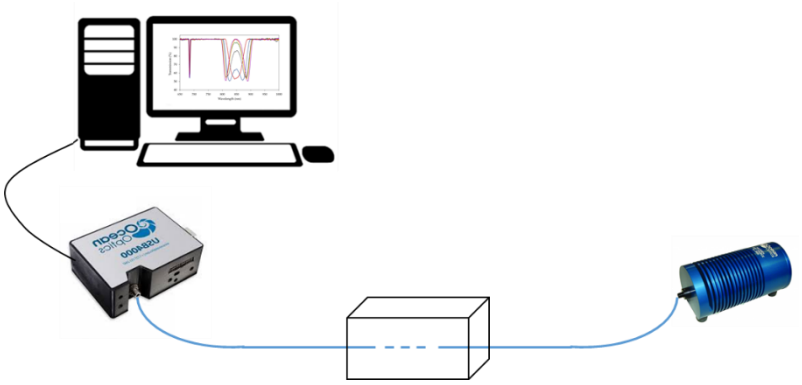

Figure II.2. Experimental set-up employed for characterizing the performance of the sensors towards ethanol.

II.4. Sensor construction process

The in-situ crystallization technique was employed to deposit ZIF-8 onto the LPGs: they were immersed for 30 minutes in a mixture of 15 ml of 2.5 mM zinc nitrate hexahydrate and 15 ml of 25 mM 2-metyl-imidazole. Afterwards, they were washed with methanol and exposed to a nitrogen flow in order to be dried [16]. These steps were repeated five times.

The above explained fabrication process was monitored for each LPG and the recorded transmission spectra at each immersion step (when the LPGs were still immersed in the solution) are displayed in Figure II.3 and Figure II.4. In the first case (Δ = 109.5 μm), when the LPG was uncoated, no resonance band was observed, and as the ZIF-8 film grew onto the grating, the transmitted light at 850 nm decreased, indicating the growth of the sensing film.

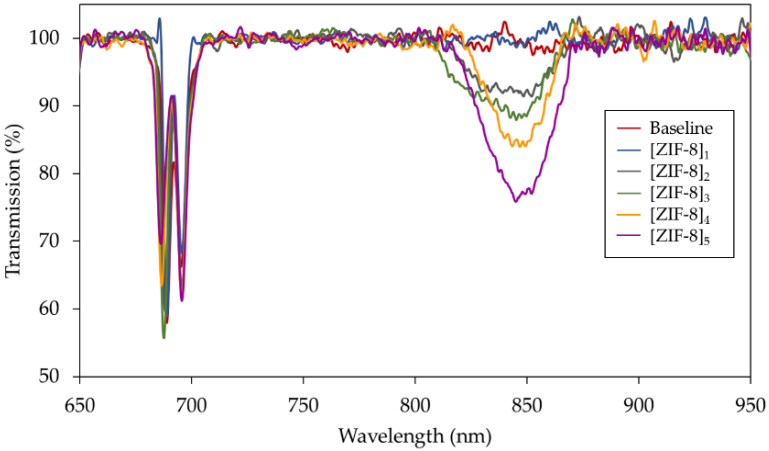

Figure II.3. Transmission spectra after the deposition of each growth cycle of ZIF-8 on a LPG of grating period of 109.5 μm.

In the case of the LPG corresponding to the grating period Δ = 109 μm, an attenuation band centered at 850 nm was observed when the grating was still uncoated. Once it was covered by a growth cycle of ZIF-8, two resonance bands were observed and, as the number of growth cycles of ZIF-8 increased, also did the separation between them.

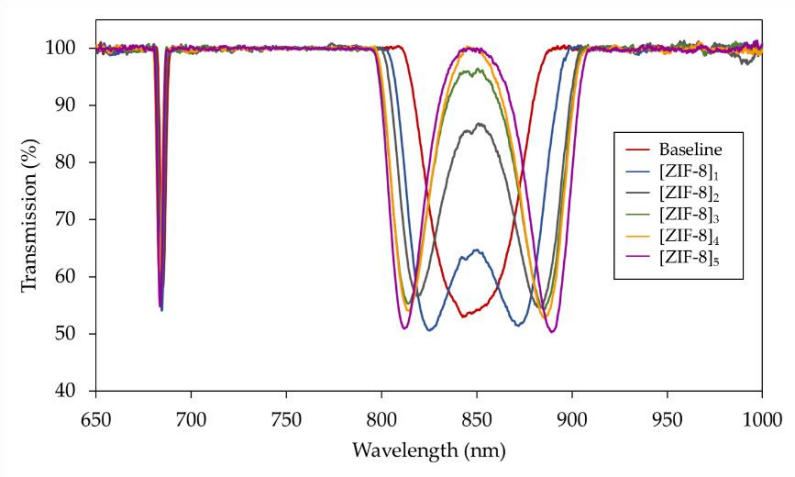

Figure II.4. Transmission spectra after the deposition of each growth cycle of ZIF-8 on a LPG of grating period of 109 μm.

II.5. Response towards low concentrations of ethanol

The performance of both sensors towards low concentrations of ethanol was analyzed using the experimental set-up shown in Figure II.2. Thus, different concentrations of ethanol, in the range from 0 to 1000 ppm, were injected inside the hermetic box.

As in the case of the sensor fabricated with the LPG of grating period 109.5 μm, only a single attenuation band centered at 850 nm was observed, the sensitivity of the sensor was calculated as the variation of the transmitted intensity (in %) divided by the ethanol concentration (measured in ppm). This value was -0.0025 %/nm, since the transmitted intensity decreased as the ethanol concentration increased, which can be observed in Figure II.5.

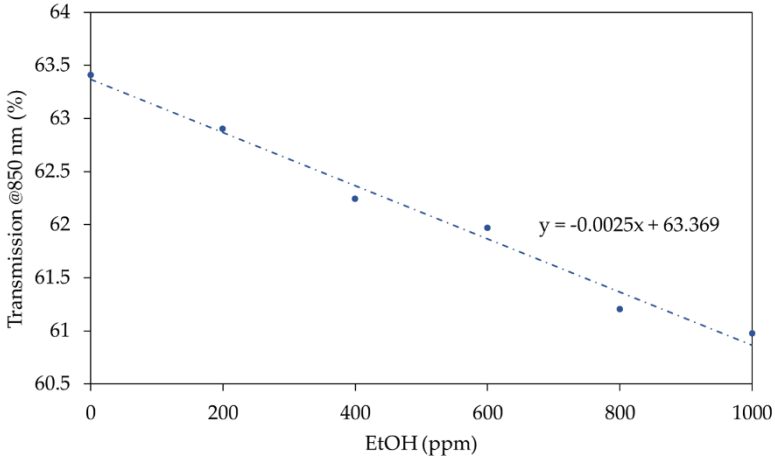

Figure II.5. Transmitted intensity (%) at 850 nm for ethanol concentrations between 0 and 1000 ppm.

The sensor corresponding to the grating period of 109 μm exhibited two resonance bands when it was coated with 5 growth cycles of ZIF-8. Thus, its sensitivity was obtained by dividing the wavelength difference between both of them (measured in nm) by the ethanol concentration

(ppm). Figure II.6 shows how the separation between both bands increased as the ethanol concentration did. The sensitivity of this sensor was 0.0009nm/ppm.

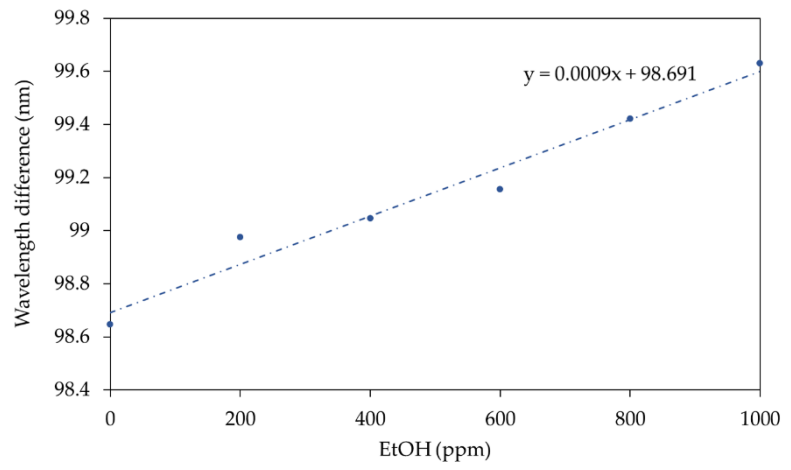

Figure II.6. Wavelength difference between the resonance bands for ethanol concentrations in the range from 0 to 1000 ppm.

When characterizing optical fiber sensors, wavelength measurements provide higher robustness than intensity ones. Thus, and also taking into account the higher sensitivity of the 109 μm-period LPG, this sensor was chosen for detecting ethanol in exhaled breath.

II.6. Cross-sensitivity and detection of ethanol in exhaled breath

II.6.1. Cross-sensitivity towards CO_2

A wide variety of VOCs and gaseous species are exhaled during breathing, whose presence can interfere in ethanol measurements. Thus, low cross-sensitivity to these parameters is required to this kind of sensors. As the chemical structure of ZIF-8 is appropriate for the detection of gas molecules and carbon dioxide (CO_2) concentration in human breath is particularly high, in the range from 40000 to 50000 ppm, so the analysis of the influence of this specie on the sensors performance is of particular interest. Therefore, the sensor was exposed to changes in the CO_2 concentration from 0 to 50000 ppm, and the increase of the wavelength separation between the attenuation bands was monitored. The obtained results are displayed in Figure II.7: as it can be observed, the changes in the CO_2 concentration did not influence the wavelength separation of the attenuation peaks, showing that the cross-sensitivity of the sensor towards CO_2 was negligible.

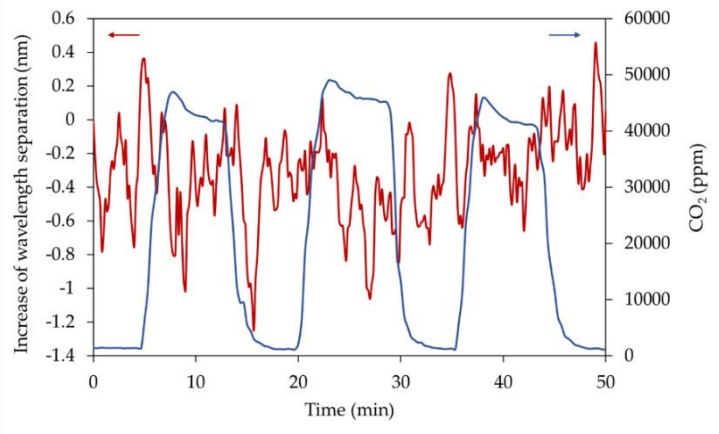

Figure II.7. Wavelength difference between the resonance bands for ethanol concentrations in the range from 0 to 1000 ppm.

II.6.2. Cross-sensitivity towards relative humidity

Another parameter of special interest when analyzing human breath is relative humidity, whose value is 100%. In such conditions, exhaled breath condensates, and the water droplets formed can be stored in the ZIF-8 cavities, influencing the response of the sensor. To study the effect of this parameter, it was varied from 35% to 90%, and it was found that the cross-sensitivity of the sensor to this variable was 0.45nm/%RH, as can be observed in Figure II.8. However, it took the sensor two minutes to response to these changes, while the exhalation process for alcoholic tests is shorter.

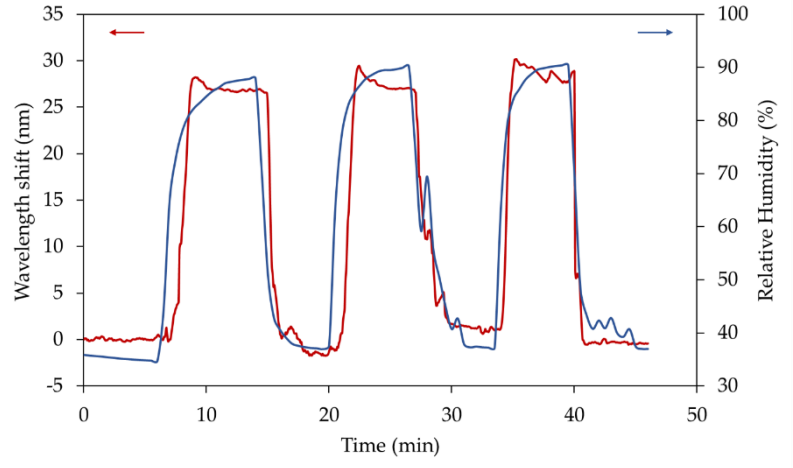

Figure II.8. Wavelength difference between the resonance bands for ethanol concentrations in the range from 0 to 1000 ppm.

II.6.3. Cross-sensitivity towards temperature

Apart from CO_2 concentration and relative humidity, temperature of exhaled breath is a parameter that can also affect the response of the sensor. Thus, it was exposed to five cycles of human breath before the ingestion of alcoholic drinks, whose temperature was monitored. As it is shown in Figure II.9, exhaled breath induced an increase of the separation between the resonance bands, which showed high dependency on temperature (4 nm per Celsius degree). Although relative humidity also affected the response of the sensor (Figure II.8), it was not monitored in this case.

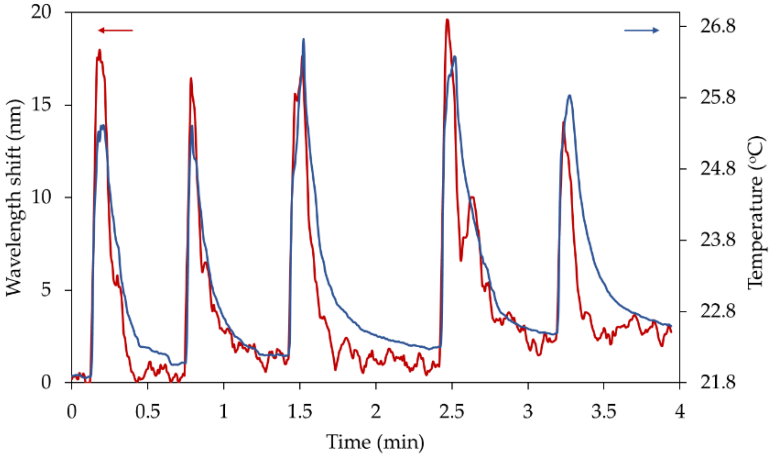

Figure II.9. Wavelength difference between the resonance bands for ethanol concentrations in the range from 0 to 1000 ppm.

II.6.4. Detection of ethanol in exhaled breath

Finally, the sensor was exposed to the exhaled breath of a person after the intake of alcoholic drinks. Its response is plotted in Figure II.10, and as it can be observed, the increase of the wavelength separation was repetitive (23 nm) for every breathing cycle, independently on the temperature of the exhaled breath. This fact demonstrated the capability of the sensor to detect ethanol in exhaled breath.

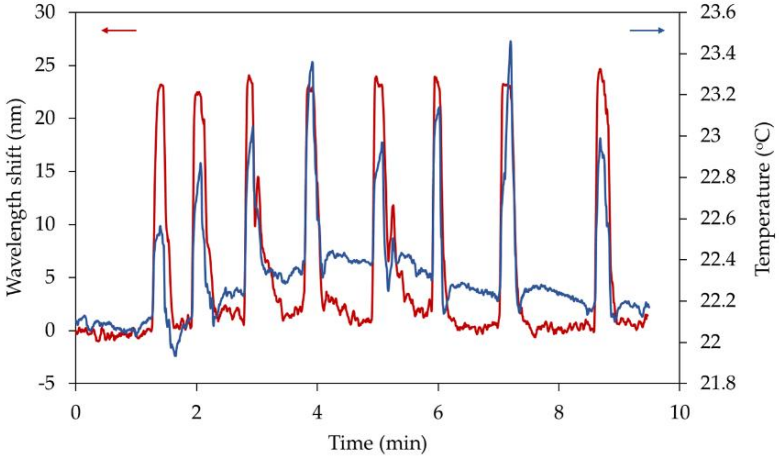

Figure II.10. Wavelength difference between the resonance bands for ethanol concentrations in the range from 0 to 1000 ppm.

II.7. Conclusions

A sensor fabricated by depositing five growth cycles of metal-organic framework ZIF-8 onto a LPG with grating period of 109 μm and length of 30 mm has been demonstrated to detect ethanol in exhaled breath. The sensor exhibited high cross-sensitivity towards relative humidity and temperature, while the influence of carbon dioxide was negligible. The wavelength separation between the resonance bands is not only higher but also repetitive when ethanol is present in exhaled breath than in its absence, independently on temperature. Further work should, on one side, quantify the exact concentration of ethanol in human breath, and, on the other side, analyze the cross-sensitivity towards other breath biomarkers (acetone, ammonia, …) and attenuate the effect of relative humidity.

The results obtained in this work open an interesting research line for the utilization of optical fiber sensors based on LPGs in real applications: by coating these gratings with the appropriate sensing materials, a wide variety of gaseous species can be monitored, for instance, in indoor environments. Another challenging application could the detection of biomarkers in exhaled breath condensate.

Bibliography

1. Wang, C.; Sahay, P. Breath analysis using laser spectroscopic techniques: Breath biomarkers, spectral fingerprints, and detection limits. *Sensors* **2009**, *9*, 8230–8262, doi:10.3390/s91008230.
2. Ashutosh, K. Nitric oxide and asthma: A review. *Current Opinion in Pulmonary Medicine* 2000, *6*, 21–25.
3. Paredi, P.; Shah, P. L.; Montuschi, P.; Sullivan, P.; Hodson, M. E.; Kharitonov, S. A.; Barnes, P. J. Increased carbon monoxide in exhaled air of patients with cystic fibrosis. *Thorax* **1999**, *54*, 917–920.
4. Domènech-Gil, G.; Samà, J.; Pellegrino, P.; Barth, S.; Gràcia, I.; Cané, C.; Romano-Rodriguez, A. Gas nanosensors based on individual indium oxide nanostructures. In *Procedia Engineering*; 2015; Vol. 120, pp. 795–798.
5. Elmi, I.; Zampolli, S.; Cozzani, E.; Mancarella, F.; Cardinali, G. C. Development of ultra-low-power consumption MOX sensors with ppb-level VOC detection capabilities for emerging applications. *Sensors and Actuators, B: Chemical* **2008**, *135*, 342–351, doi:10.1016/j.snb.2008.09.002.
6. James, S. W.; Tatam, R. P. Optical fibre long-period grating sensors: Characteristics and application. *Measurement Science and Technology* **2003**, *14*, r49–r61, doi:10.1088/0957-0233/14/5/201.
7. Elosua, C.; Matias, I. R.; Bariain, C.; Arregui, F. J. Volatile organic compound optical fiber sensors: A review. *Sensors* **2006**, *6*, 1440–1465.
8. Xu, X.; Wang, H.; Liu, J.; Yan, H. The applications of zeolitic imidazolate framework-8 in electrical energy storage devices: a review. *Journal of Materials Science: Materials in Electronics* **2017**, *28*, 7532–7543, doi:10.1007/s10854-017-6485-6.
9. Pulido-Navarro, M. G.; Escamilla-Ambrosio, P. J.; Marrujo-García, S.; Álvarez-Chávez, J. A.; Martínez-Piñón, F. Temperature sensing through long period fiber gratings mechanically induced on tapered optical fibers. *Applied Optics* **2017**, *56*, 5526–5531, doi:10.1364/AO.56.005526.
10. Ascorbe, J.; Coelho, L.; Santos, J. L.; Frazao, O.; Corres, J. M. Temperature Compensated Strain Sensor Based on Long Period Gratings and Microspheres. *IEEE Photonics Technology Letters* 2017.
11. Glavind, L.; Gao, S.; Cook, K.; Canning, J.; Skipper, B. F.; Luo, Y.; Peng, G.; Kristensen, M. Enhanced resolution of long-period grating bend sensor. In *Proceedings of SPIE - The International Society for Optical Engineering*; 2013; Vol. 8924.
12. Tsuda, H.; Urabe, K. Characterization of long-period grating refractive index sensors and their applications. *Sensors (Switzerland)* **2009**, *9*, 4559–4571, doi:10.3390/s90604559.
13. Hromadka, J.; Correia, R.; Korposh, S. Fabrication of fiber optic long period gratings operating at the phase matching turning point using an amplitude mask. In *Proceedings of SPIE - The International Society for Optical Engineering*; 2016; Vol. 9916.
14. Lu, G.; Hupp, J. T. Metal-organic frameworks as sensors: A ZIF-8 based fabry-pérot device as a selective sensor for chemical vapors and gases. *Journal of the American Chemical Society* **2010**, *132*, 7832–7833, doi:10.1021/ja101415b.

15. Hromadka, J.; Tokay, B.; James, S.; Tatam, R. P.; Korposh, S. Optical fibre long period grating gas sensor modified with metal organic framework thin films. *Sensors and Actuators, B: Chemical* **2015**, *221*, 891–899, doi:10.1016/j.snb.2015.07.027.
16. Hromadka, J.; Tokay, B.; Korposh, S.; James, S.; Tatam, R. P. Detection of volatile organic compounds using optical fibre long period grating modified with metal organic framework thin films. In *Proceedings of SPIE - The International Society for Optical Engineering*; 2015; Vol. 9634.

Appendix III

Scientific contributions

III.1. Research papers published in scientific journals that are directly related to the main topic of this thesis

[1] *Layer-by-Layer Assembly of Water-insoluble Platinum Complex for Optical Fiber Oxygen Sensors*, C. Elosúa, N. de Acha, M. Hernáez, I. R. Matías, F. J. Arregui, Sensors and Actuators B: Chemical. 207 (2015) 683–689. http://dx.doi.org/10.1016/j.snb.2014.10.042

[2] *Comparative study of polymeric matrices embedding oxygen-sensitive fluorophores by means of Layer-by-Layer nanosassembly*, N. de Acha, C. Elosúa, D. Martínez, M. Hernáez, I.R. Matías, F.J. Arregui, Sensors and Actuators B: Chemical. 239 (2017) 1124–1133. doi:10.1016/j.snb.2016.08.077

[3] *An Optimized Method Based on Digitalized Lissajous Curve to Determine Lifetime of Luminescent Materials on Optical Fiber Sensors*, A. Ridruejo, N. De Acha, C. Elosúa, I. R. Matías, F. J. Arregui, Journal of Sensors. http://dx.doi.org/10.1155/2016/6019439

[4] *Enhancement of luminescence-based optical fiber oxygen sensors by tuning the distance between fluorophore layers*, N. de Acha, C. Elosúa, I.R. Matías, F.J. Arregui, Sensors and Actuators, B: Chemical. 248 (2017) 836–847. doi:10.1016/j.snb.2016.12.081

[5] *Luminescence-based optical sensors fabricated by means of the layer-by-layer nano-assembly technique*, N. De Acha, C. Elosua, I. R. Matias, F. J. Arregui. Sensors (Switzerland), 17 (2017), doi:10.3390/s17122826

III.2. Other research papers published in scientific journals related to this thesis

[6] *Optical sensors based on lossy-mode resonances*, Ignacio Del Villar, Francisco J. Arregui, Carlos R. Zamarreño, Jesus M. Corres, Candido Bariain, Javier Goicoechea, Cesar Elosua, Miguel Hernaez, Pedro J. Rivero, Abian B. Socorro, Aitor Urrutia, Pedro Sanchez, Pablo Zubiate, Diego Lopez, Nerea De Acha, Joaquin Ascorbe, Ignacio R. Matias, Sensors and Actuators B: Chemical, 240 (2017) 174–185. doi:10.1016/j.snb.2016.08.126

[7] *Micro and nanostructured materials for the development of optical fibre sensors*, C. Elosua, F.J. Arregui, I. Del Villar, C. Ruiz-Zamarreño, J.M. Corres, C. Bariain, J. Goicoechea, M. Hernaez, P.J. Rivero, A.B. Socorro, A. Urrutia, P. Sanchez, P. Zubiate, D. Lopez-Torres, N. De Acha, J. Ascorbe, A. Ozcariz, I.R. Matias, Sensors (Switzerland), 17 (2017). doi:10.3390/s17102312

III.3. Oral contributions to international conferences that are directly related to the main topic of this thesis

[1] *Optimization of Optical Fiber Oxygen Sensors based on Metalloporphyrins following Layer-by-Layer method*, C. Elosua, N. de Acha, I.R. Matias, F.J. Arregui, Trends in Nanotechnology, 2014, Barcelona, Spain

[2] *Enhancement of an oxygen luminescent sensor by tuning the distance between fluorophore layers at the nanometer scale*, N. de Acha, C. Elosúa, I. R. Matías, F.J. Arregui, The 16th International Meeting on Chemical Sensors, 2016, Jeju Island, South Korea

III.4. Other oral contributions to international conferences related to this thesis

[3] *Fiber-Optic Lossy Mode Resonance Sensors*, Francisco J. Arregui, Ignacio Del Villar, Jesus M. Corres, Javier Goicoechea, Carlos R. Zamarreño, Cesar Elosua, Miguel Hernaez, Pedro J. Rivero, Abian B. Socorro, Aitor Urrutia, Pedro Sanchez, Pablo Zubiate, Diego Lopez, Nerea De Acha, Ignacio R. Matias, XXVIII Eurosensors, 2014, Brescia, Italy doi:10.1016/j.proeng.2014.11.253

[4] *Fiber optic sensors based on lossy mode resonances*, Matias I. R., Arregui, F. J., Del Villar I., Corres J. M. Goicoechea J., Zamarreño Z. R., Elosúa C., Hernáez M., Rivero P. J., Socorro A. B. , Urrutia A., Sanchez P., Zubiate P., Lopez D., De Acha N., Latin America Optics and Photonics Conference, LAOP, 2014, Cancun, Mexico

[5] *Nanocoated Optical Fiber for Lossy Mode Resonance (LMR) Sensors and Filters*, Ignacio Del Villar, Francisco J. Arregui, Jesus M. Corres, Candido Bariain, Javier Goicoechea, Carlos R. Zamarreño, Cesar Elosua, Miguel Hernaez, Pedro J. Rivero, Abian B. Socorro, Aitor Urrutia, Pedro Sanchez, Pablo Zubiate, Diego Lopez, Nerea De Acha, Joaquin Ascorbe, and Ignacio R. Matias, 17th International Conference on Transparent Optical Networks, ICTON, 2015, Budapest, Hungary http://dx.doi.org/10.1109/ICTON.2015.7193695

[6] *Functionalization of rough nanofilms deposited onto optical fiber to implement gas and vapors sensors*, C. Elosúa, D. López-Torres, N. de Acha, I. R. Matías, F.J. Arregui, The 16th International Meeting on Chemical Sensors, 2016, Jeju Island, South Korea

[7] *Micro and Nano structured Coatings for the Development of Optical Fibre Sensors*, C. Elosua, F. J. Arregui, I. Del Villar, C. R. Zamarreño, J. M. Corres, C. Bariain, J. Goicoechea, M. Hernaez, P. J. Rivero, A. B. Socorro, A. Urrutia, P. Sanchez, P. Zubiate, D. Lopez, N. De Acha, J. Ascorbe, A. Ozcariz, I. R. Matias, 6th International Conference on Materials and Applications for Sensors and Transducers, September 27-30, 2016, Athens, Greece

[8] *Detection of Ethanol in Human Breath Using Optical Fiber Long Period Grating Coated with Metal-Organic Frameworks*, Nerea De Acha, Jiri Hromadka, Begum Tokay, Ricardo Correia, Cesar Elosua, Ignacio R. Matías, Francisco J. Arregui, Stephen P. Morgan, Sergiy Korposh, XXXI Eurosensors, 2017, Paris, France doi:10.3390/proceedings1040474

III.5. Poster contributions to international conferences that are directly related to the main topic of this thesis

[9] *Luminescent Optical Fiber Oxygen Sensor following Layer-by-Layer metho*d, C. Elosua, N. de Acha, D. Lopez-Torres, I.R. Matias, F. J. Arregui, XXVIII Eurosensors, 2014, Brescia, Italy doi:10.1016/j.proeng.2014.11.324

III.6. Other poster contributions to international conferences related to this thesis

[10] *Sensors based on D-shaped single mode optical fiber for an array to identify volatile compounds,* C. Elosúa, N. de Acha, D. López-Torres, I. R. Matías, F.J. Arregui, The 16th International Meeting on Chemical Sensors, 2016, Jeju Island, South Korea

[11] *Development of luminescent and colorimetric optical fiber sensor based on Pt_2Pb clusters to detect volatile organic vapors,* N. de Acha, C. Elosúa, S. Ruiz, M. T. Moreno, E. Lalinde, I. R. Matías, F.J. Arregui, The 16th International Meeting on Chemical Sensors, 2016, Jeju Island, South Korea

III.7. Oral contributions to national conferences

[12] *Adaptive Lissajous method for fluorescence phase measurement system*, A. Ridruejo, N. De Acha, C. Elosúa, I. R. Matías, F. J. Arregui, XXX Simposium Nacional de la Unión Científica Internacional de Radio, 2015, Pamplona, España

[13] *Desarrollo de un sensor de fibra óptica luminiscente y colorimétrico basado en un cluster de Pt2Pb para la detección de VOCs,* Nerea de Acha, César Elosúa, Santiago Ruiz, María Teresa Moreno, Elena Lalinde, Ignacio R. Matías, Francisco J. Arregui, XIII Simposio de Investigadores Jóvenes de la RSEQ, 8-11 Noviembre 2016, Logroño, España

[14] *Optical fibre sensors for environmental and bio medical applications*, C. Elosua, F. J. Arregui, I. Del Villar, C. R. Zamarreño, J. M. Corres, C. Bariain, P. J. Rivero, A. B. Socorro, P. Sanchez, P. Zubiate, D. Lopez, N. De Acha, J. Ascorbe, A. Ozcariz, I. R. Matias. Metals and Water 2017, II International Conference on Water Soluble Metal Complexes, June 13-15, 2017, Jaca (Spain)

III.8. Poster contributions to national conferences

[15] *SnO_2 humidity interferometric sensor based on Photonic Crystal optical fiber and Fast Fourier Transform*, D. López-Torres, N. De Acha, C. Elosúa, F. J. Arregui, NanoSpain Conference, 2016, Logroño, Spain